Data Characteristics and Preliminary Results from the Atacama B-Mode Search (ABS)

Katerina Visnjic

A Dissertation
Presented to the Faculty
of Princeton University
in Candidacy for the Degree
of Doctor of Philosophy

Recommended for Acceptance
by the Department of
Physics
Adviser: Lyman A. Page

September 2013

Abstract

The Atacama B-Mode Search (ABS) is a 145 GHz polarimeter located at a high altitude site on Cerro Toco, in the Andes of northern Chile. Having deployed in early 2012, it is currently in its second year of operation, observing the polarization of the Cosmic Microwave Background (CMB). It seeks to probe the as yet undetected odd-parity B-modes of the polarization, which would have been created by the primordial gravitational wave background (GWB) predicted by theories of inflation. The magnitude of the B-mode signal is characterized by the tensor-to-scalar ratio, r. ABS features 60 cm cryogenic reflectors in the crossed-Dragone configuration, and a warm, continuously rotating sapphire half-wave plate to modulate the polarization of incoming radiation. The focal plane consists of 480 antenna-coupled transition edge sensor bolometers, arranged in orthogonal pairs for polarization sensitivity, and coupled to feedhorns in a hexagonal array.

In this thesis we describe the ABS instrument in the state in which it is now operating, outline the first season of observations, and characterize the data obtained. Focusing on observations of the primary CMB field during a one month reference period, we detail the algorithms currently used to select the data suitable for making maps. This is the first pass at data cuts and provides a conservative estimate for the sensitivity of ABS to the polarization modes in the sky. We project that with one year total observation time of the primary CMB field, ABS should be able to detect the B-mode signal at roughly the level of $r = 0.03$.

Acknowledgements

Working on the Atacama B-mode Search these past five years, and seeing it grow from mere design to actual telescope, has been an exciting and fruitful adventure that I have shared with a wonderful group of people. First off I would like to thank my adviser, Lyman Page. His insatiable curiosity and his enthusiasm are contagious and inspiring. He has exceeded his reputation as a great teacher and adviser and has become more of a mentor to me, and a friend.

I would also like to thank Suzanne Staggs, who has been like a second, unofficial adviser to me. I have learned a great deal from her thorough approach and incredible attention to detail, always sprinkled with good humor. I have also benefitted from working with Norm Jarosik, with Joe Fowler before he moved to Colorado, and with Tobias Marriage before he moved to Johns Hopkins.

Work on ABS involved many late nights in the lab and long days on the mountain in Chile, and sharing those experiences with Lucas Parker, John Appel and Thomas Essinger-Hileman for five years has turned great lab mates into great friends. It was a pleasure to be joined by more great team mates along the way: Akito Kusaka, Jon Sievers, Sara Simon, and Srinivasan Raghunathan. I have also enjoyed interacting with the scientists at ACTpol, and previously ACT, with whom we share the site: Jeff Klein, Mark Devlin, Emily Grace, Laura Newburgh, Christine Pappas, Rolando Dunner, Adam Hincks, Michael Niemack, Yue Zhao, Mike Nolta, and Matthew Hasselfield. Thank you to Xin Xin Du, Alex Dahlen, Richard Saldanha, Arijeet Pal, Tiberiu Tesileanu, Silviu Pufu, Pablo Mosteiro, Mikhail Tokhonov and Theodor Brasoveanu, for making Jadwin cozy.

I am also grateful to the people who work behind the scenes in Jadwin to make everything run smoothly. To the A-Level team: Claude Champagne, Barbara Grunwerg and Lauren Callahan in Purchasing; Darryl Johnson in Shipping, Ted Lewis in the Stock Room, Steve Lowe in the student shop, and Mike Peloso for teaching me

how to machine; Bill Dix and Glenn Atkinson in the Machine Shop - your ingenuity in machining the most intricate pieces never ceases to amaze me. A walk through A-Level always cheers me up. To the second floor team: Angela Qualls, Geoff Gettelfinger, Regina Savage, Jessica Heslin, Julianne Jones, Karen Kelly, and previously Laurel Lerner. Thank you for making even the most tricky problems and difficulties magically disappear.

Outside of my work family, I have been surrounded by great friends, both within and outside of Princeton. In particular I would like to thank Maria Martynovsky, Mark Ioffe, Gopal Sarma, Srdjan Krstic, Ketra Kanodia, Chris Laumann, Aakash Pushp, and Charles Mathey.

And finally, a special thanks to my family: to Vanya Visnjic, my brother, my intellectual sparring mate, my former actual sparring mate, and my always best friend. And to my first and favorite teachers, my parents Vladimir Visnjic and Georgia Triantafillou. This thesis is dedicated to them.

Contents

List of Tables

List of Figures

Chapter 1

Introduction

Questions about the origins of the Universe have fascinated and puzzled humanity for millennia. The various cosmogonic theories proposed over the years can be found in mythology, philosophy, and religion, and only in the last few decades has technology progressed enough to allow us to acquire data and put the various models to the test. The discovery of the Cosmic Microwave Background (CMB) [30] almost 50 years ago arguably marks the birth of cosmology as a science. The existence of an isotropic black body background was predicted over a decade earlier[2], as a consequence of the idea that the Universe is expanding, this being the radiation emitted when the Universe used to be denser and hotter. Although the connection between the first measurement at 3 GHz indicating a $\sim$ 3 K thermal source, and the relic radiation was produced almost immediately [13], its black body nature was not fully verified until 1990 [26, 20], when the Far-InfraRed Absolute Spectrophotometer (FIRAS) on the Cosmic Background Explorer (COBE) satellite measured the CMB in the Wien regime, above 150 GHz. The temperature of this black body is now known to be 2.72548 ± 0.00057 K[17]. Additionally, the Differential Microwave Radiometers (DMR), also aboard COBE, gave the first accurate measurement of the anisotropies

at the 7° scale, 16 ± 4 μK, revealing that the Universe is isotropic to one part in $\sim 100,000$[41].

1.1 The Standard Model of Cosmology

In the past decade, increasingly precise measurements of the CMB temperature anisotropies [7, 10, 32] have culminated in a well-established standard model of cosmology, called the ΛCDM model. It assumes a homogeneous and isotropic Universe with adiabatic, Gaussian fluctuations. It is the simplest model which is in agreement with all the observations to date, including zero spatial curvature, the large scale structure formation observations, and the accelerated expansion rate determined from supernovae observations. Here, Λ represents the cosmological constant, one form of dark energy, while CDM stands for cold dark matter, which is non-relativistic, dissipationless and collisionless, interacting with other particles only through the weak force and gravity, and possibly through other interactions no stronger than the weak force.

The cosmological constant was first introduced by Einstein in his equations of General Relativity in his quest to construct a static Universe. It permeates all of space uniformly and acts as a negative pressure, expanding spacetime and counteracting the attractive force of gravity. It was discarded in 1927 when the Universe was discovered to be expanding, until the rate of expansion was observed to be increasing, and a uniform repulsive force was required to explain this counter-intuitive phenomenon[43]. Unlike dark energy, dark matter is not uniformly distributed, having undergone gravitational collapse much the same way as ordinary matter. The presence of unaccounted for mass in the centers of spiral galaxies was detected from their rotation curves, which were seen to level off instead of decrease. We now know that over 80% of the matter in our Universe is dark: according to the ΛCDM model,

ordinary matter makes up roughly 5% of the current energy density of our Universe. Dark matter comprises 23% and the rest, by far the most at 72%, is dark energy. Given its six parameters (Tab. 1.1), the ΛCDM model successfully describes the evolution of the Universe starting from 10^{-10} s after the Big Bang, when the energy was 7 TeV, until today. [1]

Parameter	Description	Best-fit Value
$\Omega_b h^2$	Baryon density	0.02264 ± 0.00050
$\Omega_c h^2$	Cold dark matter density	0.1138 ± 0.00045
Ω_Λ	Dark energy density	0.721 ± 0.025
$10^9 \Delta^2_{\mathcal{R}}$	Amplitude of curvature perturbations	2.41 ± 0.10
n_s	Spectral index of density perturbations	0.972 ± 0.013
τ	Reionization optical depth	0.089 ± 0.014

Table 1.1: Best-fit ΛCDM parameters for a flat Universe from WMAP 9-year data[21]. Here, $\Omega_{b,c,\Lambda}$ denote the fractional density of baryonic matter, cold dark matter, and dark energy, and the hubble parameter $h = 0.700 \pm 0.022$, explained in more detail in Section 1.1.2, relates the fractional density to the physical density.

1.1.1 The Oldest Light In The Universe

As the Universe expanded, its temperature and density decreased. Thus the evolution of the early Universe, up until 0.1 eV, can be separated into periods characterized by what reactions were allowed to occur (Tab. 1.2). Each period begins when the temperature drops enough to allow the bound state of a particle which in turn allows a particular reaction to happen. It ends with a freeze-out, when the reaction rate drops below the expansion rate. For unstable particles there is an additional time element, the half-life of the particle.

Before the first second had passed, nucleons and neutrinos had already frozen-out. At 3 minutes, in a process called Big Bang nucleosynthesis, protons and neutrons fused to form deuterium and tritium, which in turn fused to form helium-4. By the

[1] 7 TeV is the maximum energy that terrestrial accelerators have been able to probe, and marks the current limit of our knowledge.

time the energy fell below the point where fusion could occur, at 20 minutes, there was about three times more hydrogen than helium-4 by mass, and trace amounts of heavier nuclei. The photons were still strongly interacting via Compton scattering with the charged matter particles, and the counteracting forces due to gravity and photon pressure created baryon acoustic oscillations (BAO), or sound waves, in the plasma, of part in 10^5[41].

Event	Time	Energy	Redshift
Inflation?	$\geq 10^{-34}$s	$\leq 10^{15}$ GeV	
Electroweak unification	10^{-10}s	1 TeV	
Quark-hadron transition	10^{-4} s	10^2 MeV	
Nucleon freeze-out	0.01 s	10 MeV	
Neutrino freeze-out	1 s	1 MeV	
Big bang nucleosynthesis	3 min	0.1 MeV	
Matter-radiation equality	10^4 yrs	1 eV	3,200
Recombination	10^5 yrs	0.1 eV	1,100
Reionization	10^8 yrs		$25 - 6$
Large scale structure formation	$\sim 6 \times 10^8$ yrs		~ 10
Now	14×10^9 yrs	1 meV	0

Table 1.2: Timeline of the Universe.

The Universe continued as an oscillating plasma of nuclei and electrons for $\sim 380,000$ years until the energy dropped enough for neutral hydrogen to form, a process called Recombination. Over a relatively short period of time, all the electrons combined with protons[2], allowing the 3000 K black body spectrum of photons to decouple from matter and start free streaming. This decoupling marked the transition of the Universe from opaque to transparent. Since light travels at a finite speed, an observer is only able to see as far as his past light cone until decoupling. This looks like a transparent bubble centered at the observer and bounded by the "surface of last scattering" which is receding at roughly the speed of light[3]. The expansion of the Universe until the present time redshifted the photons to their current tempera-

[2]The much smaller fraction of heavier atoms were already bound.

[3]Not accounting for the expansion of Universe.

ture of 2.7 K. The photons reaching us from the surface of last scattering have been traveling freely for the past 13.8 billion years, presenting us with a "baby picture" of the Universe.

1.1.2 Temperature anisotropies

The most general metric describing a homogeneous and isotropic space varying in time is known as the Friedmann-Robertson-Walker (FRW) metric:

$$ds^2 = dt^2 - a(t)\left(\frac{r^2 dr}{1 - Kr^2} + d\Omega^2\right), \tag{1.1}$$

where $K = 0$, 1, -1 for a flat, positive and negative spatial geometry, respectively, r and Ω are spherical coordinates for 3-space, and $a(t)$ is the "scale factor" giving the physical size of the Universe as a function of time. The convention is to take $a_0 \equiv 1$, where the subscript 0 henceforth denotes the value today. We define the redshift $z \equiv 1/a - 1$ and the expansion rate $H \equiv \dot{a}/a$ whose current value is known as the Hubble constant, $H_0 \equiv 100h$ km/s/Mpc $= 67.3 \pm 1.2$ km/s/Mpc[33].

Since the scale factor is the only quantity varying with time, studying the dynamics of an FRW Universe is reduced to studying the evolution of $a(t)$. Applying Einstein's field equations to the FRW metric yields two differential equations:

$$H^2 + \frac{K}{a^2} = \frac{8\pi G\rho}{3}, \tag{1.2}$$

$$\dot{\rho} = -3H(\rho + p). \tag{1.3}$$

Equation (1.2) is the Friedmann equation governing the expansion of the Universe and (1.3) is the energy conservation law as explained below. The first equation gives the relationship between the energy density ρ and the spatial curvature K. For a flat

Universe, $\rho = \rho_c \equiv 3H^2/8\pi G$. For greater or smaller values of ρ it would be positively or negatively curved, respectively.

The conservation law relates H to the equation of state, $w \equiv p/\rho$. For relativistic matter, non-relativistic matter and dark energy, $w_{R,M,\Lambda} = 1/3,\ 0,\ -1$, respectively. Although at any given time all three forms of energy are present, it is revealing to consider the extreme cases which yield: $\rho_R \propto a^{-4}$, $\rho_M \propto a^{-3}$, and $\rho_\Lambda \propto 1$. As Figure 1.1 illustrates, this implies that although we are now in a dark energy dominated Universe, there was a period when it was matter dominated, and before that it was radiation dominated. In terms of the fractional densities $\Omega_* \equiv \rho_*/\rho_c$ the Friedmann equation (1.3) can be simply written as

$$1 = \Omega_R + \Omega_M + \Omega_\Lambda + \Omega_K, \tag{1.4}$$

where $\Omega_K \equiv -K/a^2H^2$ is called the curvature density. Observations have shown that the curvature of our Universe is consistent with zero to within 0.5%, so from now on we will take K=0.

Just as the high level of isotropy of the Universe is revealing, the one part in 10^5 anisotropies mentioned above are rich with information about the early Universe. To study the anisotropies it is convenient to decompose the temperature on the surface of last scattering into real spherical harmonics $Y_{\ell m}(\hat{n})$:

$$\Delta T(\hat{n}) = T(\hat{n}) - T_{mean} = \sum_{\ell m} a_{\ell m} Y_{\ell m}(\hat{n}). \tag{1.5}$$

Since the mean temperature is already subtracted, the lowest non-zero term is the dipole term $\ell = 1$, which is dominated by the Doppler effect due to Earth's motion relative to the CMB. In other words the CMB defines a rest frame for the Universe and the Earth's velocity in it. The coefficients $a_{\ell m}$ depend on the choice of coordinate frame, so to get a frame-independent characterization of the CMB we define the

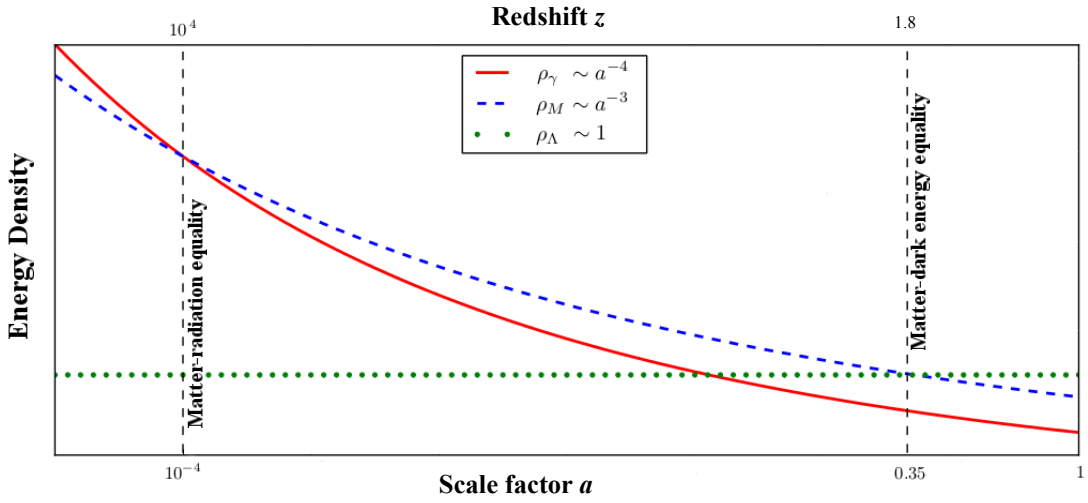

Figure 1.1: Evolution of the energy densities as a function of the scale factor for a radiation dominated (red solid curve), matter dominated (blue dashed curve) and dark energy dominated (green dotted curve) Universe. Figure not drawn to scale.

multipole coefficients as the average over all ms for a given ℓ:

$$C_\ell \equiv \frac{1}{2\ell+1}\sum_m |a_{\ell m}|^2.$$

Figure 1.2 shows the power spectrum of the CMB as measured by several modern experiments. The oscillations in the spectrum represent the state of the baryon acoustic oscillations at the time of decoupling. A mode starts to oscillate when its wavelength is twice the size of the horizon, defined as the boundary between causally connected and not connected regions of spacetime. In other words, it is the size of a light cone originating at the big bang in the standard model. Smaller angular scales represent modes that entered the horizon earlier and have been oscillating longer. The first peak at $\ell \sim 100$ represents the last mode to have entered the horizon and reached maximal compression due to gravitational collapse before decoupling, and thus gives the size of the horizon at decoupling. The second peak represents the mode that has undergone one half oscillation, at which point the previously under-

dense regions achieve maximal compression and vice-versa. The third peak represents the mode which has undergone a full oscillation, and the over-dense regions coincide with their initial position. Dark matter, which does not feel the photon pressure, does not oscillate; rather its distribution in the sky remains fixed, and it only undergoes gravitational collapse. This effect can be seen in the relative amplitudes of the first few peaks: after half of an acoustic oscillation, the ordinary matter distribution, which initially coincides with the dark matter, becomes anti-aligned, and after a full oscillation it coincides again. Thus the even numbered peaks are suppressed and the odd numbered peaks are amplified.

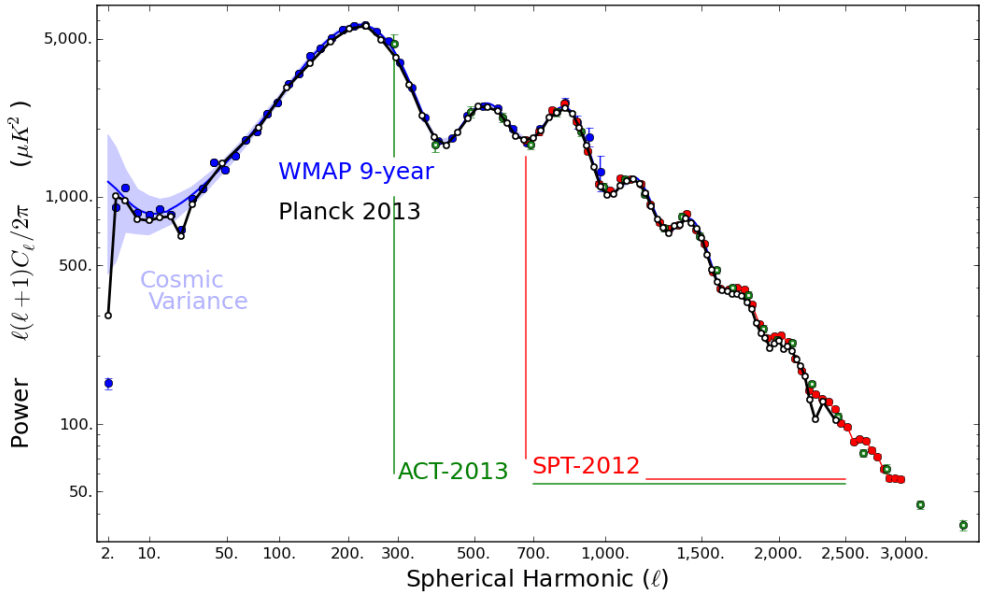

Figure 1.2: Measurements of the CMB power spectrum. Shown are the spectra from the 9-year WMAP data [7] at large angular scales, $\ell < 1000$, in blue and from the Atacama Cosmology Telescope (ACT) [10] and the South Pole Telescope (SPT) [42] at smaller angular scales in green and red, respectively. The recent Planck measurements [31] are shown in white go up to $\ell <\sim 2,500$. Figure courtesy of Mark Halpern.

1.2 Inflation

1.2.1 Motivation

The ΛCDM model is consistent will all current data, but does not explain how the Universe arrived at its initial state of isotropy and flatness with a nearly scale invariant spectrum of minute anisotropies. In a radiation or matter dominated Universe, such a state is in unstable equilibrium, which is problematic from a philosophical standpoint. Inflation was postulated to address this extreme fine-tuning of the initial conditions.

Horizon problem At the time of decoupling, the horizon of an observer was much smaller than it is today; its angular diameter in our sky is $\sim 1.6^\circ$. In a matter and radiation dominated Universe, any inhomogeneities on scales larger than a few degrees would not have been smoothed over, in direct contradiction with the observed degree of isotropy over the entire sky. The fact that the CMB is so uniform on nominally causally disconnected scales suggests that our entire visible Universe was at one time causally connected and in thermal equilibrium. That is, the horizon started out at least as big as it is now, *shrank*, and then started expanding in the "normal" way. This counter-intuitive effect of a shrinking horizon occurs during exponential expansion.

Figure 1.3 illustrates the horizon problem with a spacetime diagram, with coordinate time t, which is the time as measured by a clock in a comoving reference frame, rather than the usual conformal time $\tau \equiv \int \mathrm{d}t/a(t)$. On the $x-$axis is the usual comoving space coordinate x. In this diagram the trajectories of the photons are no longer straight lines; over time the scale factor, and thus the physical distance between two coordinates, increases, and it takes light longer in coordinate time to travel from one point to the other, distorting the traditional light cone into a trumpet shape. The shape of the light's trajectory $t(x)$ can be found by doing the coordinate transformation $\tau \to t$ of the conformal light cone $\tau(x) = x$. In the case of matter dominated

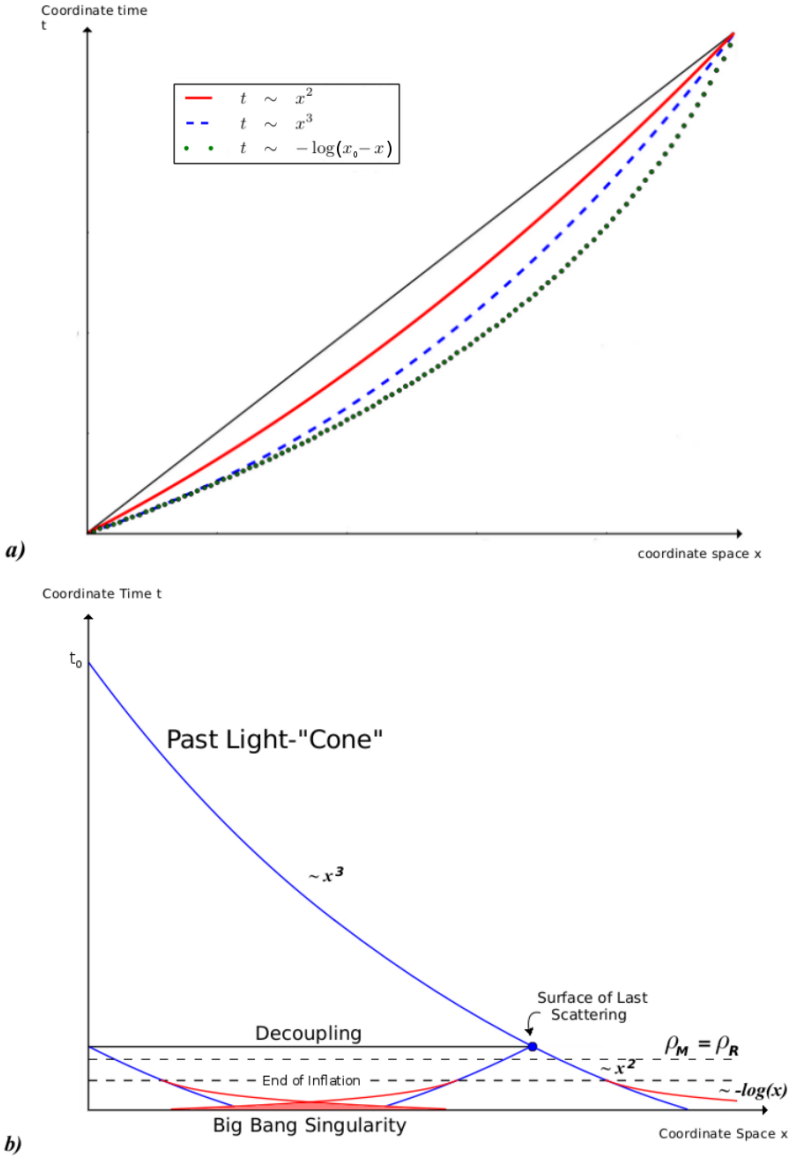

Figure 1.3: "Non-conformal" space-time diagrams, with coordinate time rather than conformal time on the y-axis. a) The trajectories of a photon between two given coordinate points in a radiation (red, thick solid line) and matter (blue, dashed) dominated Universe and during exponential expansion (green, dots). The trajectory in conformal time is shown for comparison (black, thin solid line). b) The 'horizon problem' illustrated. In a matter- and radiation-dominated Universe the past light cones of two points on the surface of last scatter do not overlap (blue trajectories). Exponential expansion during inflation has the effect of stretching out the tails of the cones, bringing the two points into causal contact (red trajectories).

expansion,

$$\begin{aligned} a &\sim t^{2/3}, \text{ so} \\ \tau &\sim \int t^{-2/3} \mathrm{d}t \sim t^{1/3}, \\ x &\sim \tau \sim t^{1/3}, \text{ and} \\ t &\sim x^3. \end{aligned}$$

Following a similar procedure for the other two types of expansion yields

$$\begin{aligned} &\text{radiation domination} \quad a(t) \sim t^{1/2} \quad \Rightarrow \quad t \sim x^2 \\ &\text{exponential expansion} \quad a(t) \sim e^t \quad \Rightarrow \quad t \sim -\log(x_0 - x), \end{aligned}$$

where x_0 is the coordinate which the light ray asymptotically approaches as the Universe expands exponentially. The effect that inflation has on the light cone is to stretch out the tails, expanding our past horizon exponentially in time.

Flatness problem Rewriting the Friedmann equation as $\dot{a}^2 = \frac{8}{3}\pi G a^2 \rho - K$, we see that for a matter and radiation dominated Universe, where $a^2 \rho_{M,R} \sim a^{-1}$, a^{-2}, respectively, the first term dominates over the curvature parameter $K = \pm 1$ as $a \to 0$ at early times, and the density approaches the critical density. In other words, zero curvature is an unstable equilibrium point, and a slight curvature at early times would grow. The fact that we are within 0.5% of the critical density now requires that at matter-radiation equality the Universe was within 0.0005% of the critical density, and even closer before that. Now that we have recently entered the dark energy epoch and $a^2 \rho_\Lambda \sim a^2$, over time our Universe will tend to get more flat. The exponential expansion during inflation would have had a similar effect as the exponential expansion due to dark energy, wiping out any initial curvature and bringing the Universe to the flatness required for the ΛCDM initial conditions.

1.2.2 Polarization

How does one test a theory about the first 10^{-34} seconds when the oldest light in the Universe was emitted almost half a million years later? Inflation posits that the exponential expansion would have stretched quantum fluctuations into macroscopic perturbations in the spacetime metric. These metric perturbations can be decomposed into scalar, vector and tensor modes. The vector modes represent peculiar velocities and vortices, which would have decayed with the expansion of the Universe and so would not have a measurable power spectrum. The scalar and tensor modes on the other hand would have maintained their amplitude, and on re-entering the horizon would have started to propagate as sound and gravitational waves respectively.

The prediction of a nearly scale-invariant spectrum of scalar perturbations is in line with the observations of the temperature anisotropies of the CMB, however there is no evidence as of yet for the existence of tensor modes. Gravitational waves propagating through the Universe would have left their signature on the CMB both as temperature anisotropies, in particular at low ℓ, and as a polarization tensor field. The strength of the tensor field is quantified by the tensor-to-scalar ratio, r, defined as the ratio between the amplitudes of the tensor and scalar fluctuations at the quadrupole, at $\ell = 2$. The value of r depends only on the characteristic energy scale at which inflation occurred, and in the most straightforward single-field inflationary models that energy scale goes as $r^{1/4}(2 \times 10^{16}$ GeV)[25]. The current upper bound on r is based on the temperature anisotropies. Improving this limit requires a direct measurement of the polarization.

The CMB tensor field can be decomposed into two fields invariant under rotation, one curl-free and one divergence-less, termed E and B respectively[4] [40]. Examples of pure E- and B-modes can be seen in Figure 1.4 on the left. E is invariant under parity transformations whereas B changes sign, making it a pseudoscalar field. Temperature

[4]In analogy with the curl-free electric and divergence-less magnetic fields.

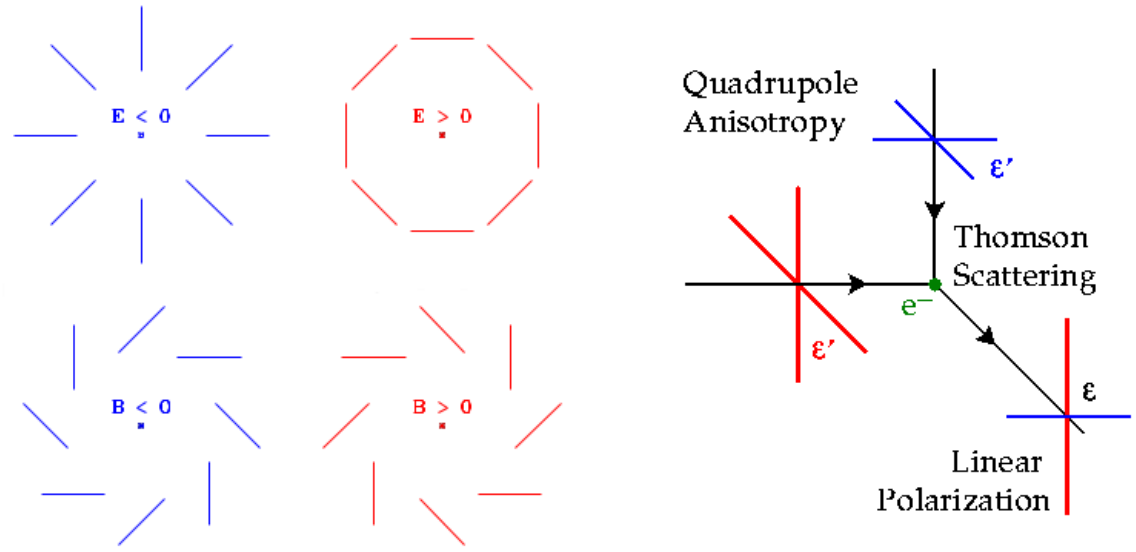

Figure 1.4: Left, pure scalar curl-free E-modes and pseudoscalar divergence-less B-modes. The E- and B-modes are not measured locally; they are Fourier modes and for pure decomposition require the tensor field to be measured over the entire sky. Finite sky coverage and pixelization introduce some ambiguity in the decomposition [8]. Right, illustration of how a temperature quadrupole anisotropy can produce a net linear polarization. Figure from [46].

quadrupole anisotropies can also produce a net polarization due to the anisotropic Thomson scattering from the hot and cold regions (Fig. 1.4 right). However scalar perturbations can only source the scalar E-modes making B-modes the purest probe of the primordial gravitational wave background.

The upper bound on r based on measurements of the CMB polarization alone is currently at 0.12 [33]. Improving this limit by approximately an order of magnitude would allow us to probe energies below the grand unification energy of 10^{16} GeV. A measurement of B-modes at this level would not only be compelling evidence for inflation, it would also be the first detection, direct or indirect, of primordial gravitational waves, confirming their existence. Furthermore, it would give insight into fundamental physics at energy scales which are 10^{13} times greater than we have been able to probe with the most powerful particle accelerators on Earth. If the B-

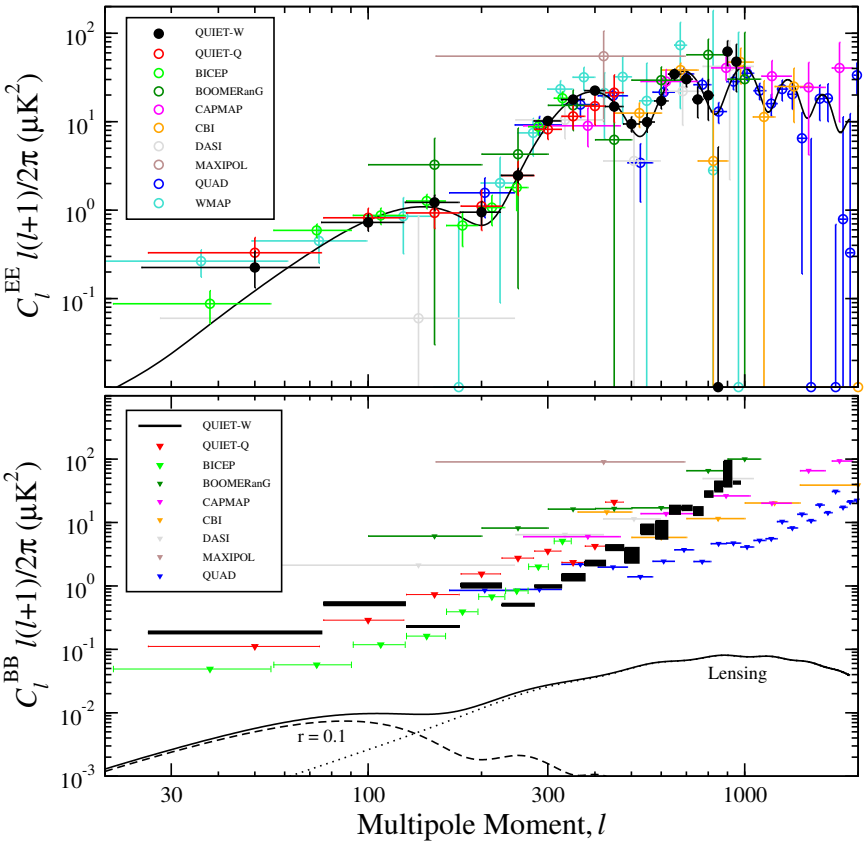

Figure 1.5: Measurements as of 2012 of the EE power spectrum, and upper limits for the BB power spectrum. The predicted BB spectrum for $r = 0.1$ is shown for reference. It is dominated by the inflationary component at large scales, and by gravitational lensing of E-modes at small scales. For $r <\sim 0.01$ the inflationary component would be too small to be distinguishable from the gravitational lensing component even at its peak at $\ell \sim 100$, without statistical analysis and foreground removal. Figure from [35].

modes remain elusive, an upper bound on r at this level would significantly constrain the many models of the birth of the Universe[5].

1.3 The Atacama B-mode Search (ABS) Experiment

Given the insight on cosmology and particle physics that a detection of the primordial gravitational wave background would result in, there are a number of experiments

targeting the B-modes, such as Planck [31], SPIDER [19], POLARBeaR [34] and its planned expansion to the Simons Array, CLASS [15], EBEX [38], ACTpol [27], SPTpol [4], QUBIC [22], PIPER, and BICEP/BICEP II/Keck [45, 36]. This dissertation will focus on the Atacama B-mode Search (ABS) experiment, a 145 GHz polarimeter optimized for degree angular scales. The telescope was designed and built mainly at Princeton University, with collaborators at Johns Hopkins University and the National Institute of Standards and Technology (NIST). Since its deployment in early 2012 ABS has been taking data in the Atacama Desert of Chile, at an altitude of 17,000 ft (5,200 m). With an array sensitivity of 35 $\mu K\sqrt{s}$, after a full year of observation time, ABS is expected to probe r down to ~ 0.03 (Fig. 1.6).

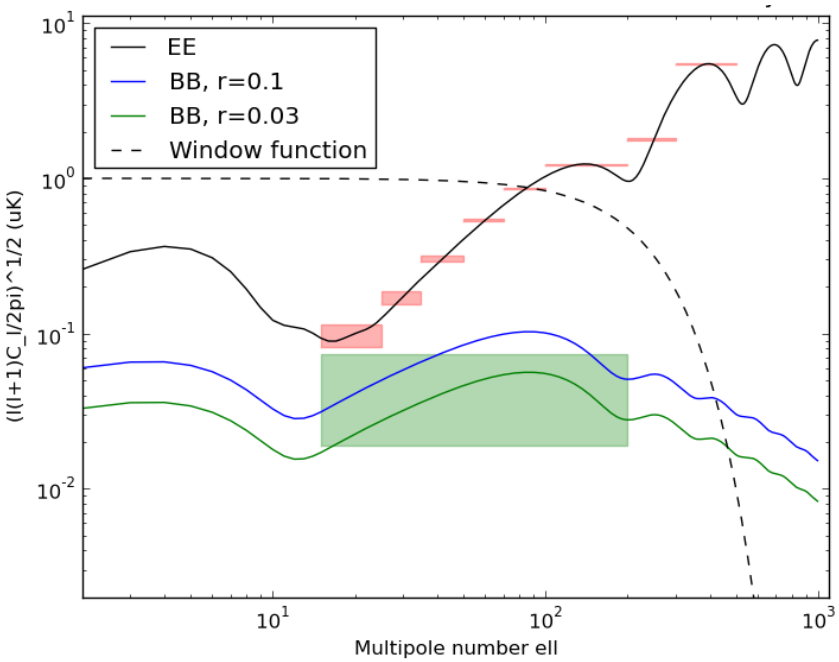

Figure 1.6: Projected sensitivity of ABS to the EE and BB power spectra after a full year of observation of the primary CMB patch. The window function assumes a Gaussian beam of full width at half maximum of 0.58°. Esimated binned errors for the EE spectrum and the BB spectrum with r= 0.03 are shown as red and green boxes.

Acquiring such high sensitivity relies on several factors, the most important of which are listed here. First, the location of the observation site was chosen for its

high altitude and low humidity, reducing the in-band loading from the water in the atmosphere. Second, a half-wave plate spinning continuously at ~ 2.5 Hz modulates the polarization signal at ~ 10 Hz, shifting it away from the $1/f$ noise of the atmosphere. Third, a series of IR-blockers and low pass filters are inserted at the three temperature stages of 300 K, 50 K and 4 K, blocking out most of the out of band radiation before it reaches the fiducial volume of the telescope. Fourth, the mirrors are in the beam path after the optical filters, and are cooled to 4 K reducing the thermal loading onto the focal plane.[5] Finally, the focal plane, cooled to 300 mK, is comprised of 240 pairs of state-of-the-art, feedhorn-coupled, transition-edge-sensor (TES) polarimeters developed by the Quantum Sensors Group at NIST, which were extensively tested and characterized in a field-able instrument for the first time by ABS.

The following chapters describe the design, construction and deployment of ABS, as well as the data obtained in the first few months of observations and the methods and techniques used to reduce these data for the production of the first CMB polarization maps. Chapter 2 describes the ABS instrument with a focus on the feed horns and the optical filters mentioned above. Chapter 3 presents a characterization of the raw data acquired from the observations. Chapter 4 describes the data selection criteria and presents preliminary maps.

[5]The continually spinning room-temperature half-wave plate element as the first optical element and the 4 K reflectors are unique to ABS.

Chapter 2

The ABS Instrument

2.1 Overview

The design of the ABS cryostat was built on the requirement that the focal plane be at 300 mK and the reflectors at 4 K. The cryostat, as shown in Figure 2.1, is a 1.02 m diameter by 1.04 m tall aluminum cylinder (40" by 41"), consisting of two lids and, for easier access to the interior, two stacked cylindrical walls.[1] It has four vacuum seals in all, including that for the window. It consists of four shells in three cryogenic stages, the vacuum shell and μ-metal magnetic shield at 300 K, an aluminum shell at 40 K and a cryoperm shell at 4 K which also serves as magnetic shielding. They are thermally isolated from each other by two G-10 stages. For additional radiation shielding between the stages, each shell is wrapped with $\sim$ 30 layers of aluminized mylar. The 58.5 cm parabolic primary and 57.1 cm hyperbolic secondary reflectors, arranged in the compact cross-Dragone design, are housed within the 4 K fiducial volume and mounted to the 4 K baseplate. The focal plane, described in more detail below, is mounted next to the primary, at a 12° angle from vertical relative to the plane of the primary.

[1] It was designed by Lucas Parker and was built by Precision Cryogenic Systems, Inc

The temperatures of the shells are maintained using two Pulse Tube Cryorefrigerators from Cryomech, one PT407 and one PT410, each of which has nominal 4 K and 40 K stages. They are mounted on the side of the cryostat at 45° so that they are vertical and operating most efficiently when the telescope is tilted to 45° elevation. In the field the stages operate at 3.6 K and 42 K, at which temperatures the two pulse tubes together provide 1.0 W and 41 W of cooling power, respectively. In addition to cooling the 4 K components of the cryostat, the pulse tubes back the helium adsorption refrigerator system, which is used to achieve the target focal plane temperature of 300 mK.

2.1.1 Half-Wave Plate

The first thing an electromagnetic wave sees coming from the sky is the ABS continuously rotating 33 cm half-wave plate made of single crystal, A-cut sapphire. Sapphire is a birefringent material; namely its index of refraction along one axis, called the extraordinary axis, is less than that along the other two "ordinary" axes. The ABS disk is cut perpendicular to an ordinary axis, so that the extraordinary and the other ordinary axis are in the plane of the disk. Linearly polarized light entering a waveplate can be decomposed into two waves, each of whose electric field is aligned with one of these axes. In the plate, the wavelengths of these two components are different. A half-wave plate (HWP) for a particular frequency is the proper thickness so that at the far side of the plate, the component aligned with the ordinary or 'slow' axis is delayed by exactly half a wavelength compared to the other 'fast' component (Fig. 2.2). The polarization of the outgoing wave is thus reflected through the fast axis, and further, if the HWP spins with frequency f, constant incoming polarization is modulated at $4f$.

The optimal HWP thickness for the ABS band of $127-163$ GHz is 3.15 mm, since the indices of refraction of the ordinary and extraordinary axes at central frequency 145 GHz are 3.40 and 3.07, respectively. With sapphire having such a high average

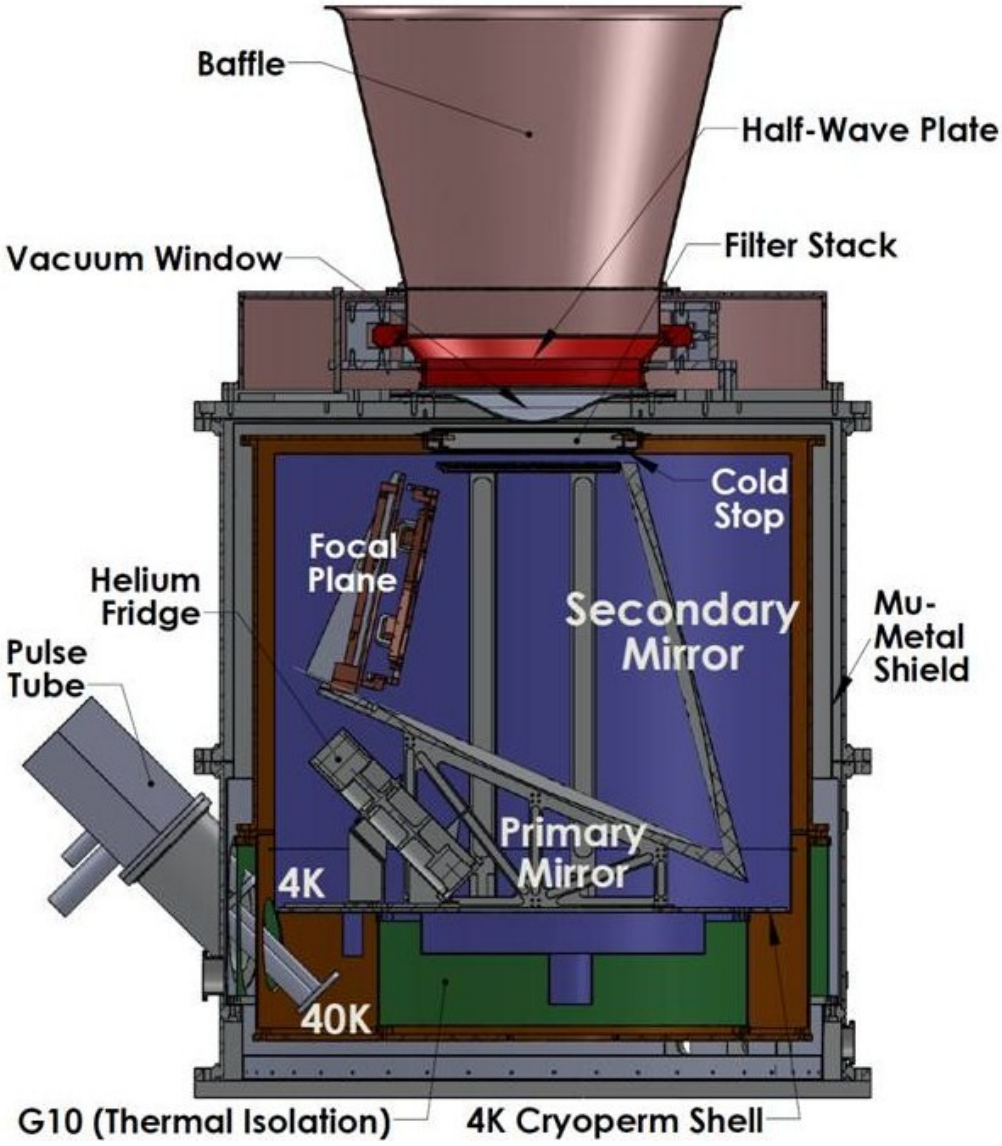

Figure 2.1: The ABS receiver, highlighting the most important features. The 300 K volume is shown in silver, the 40 K volume in brown, and the 4 K fiducial volume in purple. G-10 cylinders are used to thermally isolate the stages and the two stages are shown in green. The focal plane, which runs at 300 mK, is thermally connected to the helium fridge system housed below the primary mirror by copper cold fingers not pictured here. The half-wave plate and its air-bearing system are in red. The pulse tubes are mounted for optimal operation at an elevation of 45°. Figure courtesy of Thomas Essinger-Hileman.

index of refraction, the percentage of reflected light oscillates wildly within our band, ranging from $0 - 70\%$ (Fig. 2.3), and it reflects outgoing radiation back into the cryostat, modulated at $2f$. To minimize this effect, the sapphire was anti-reflection

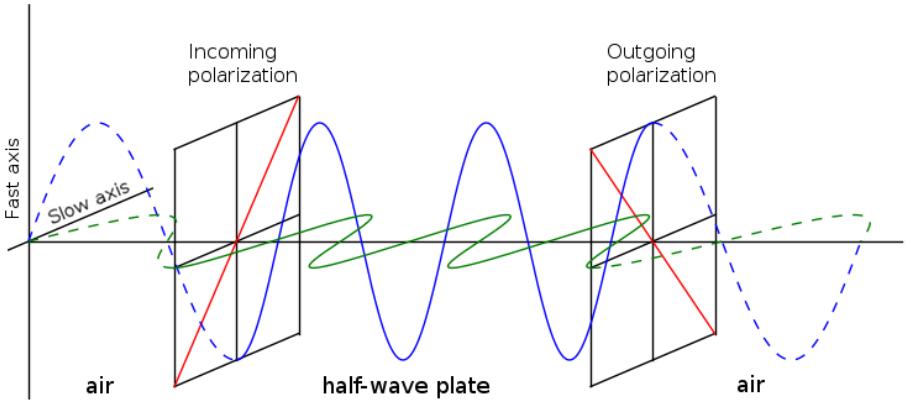

Figure 2.2: Propagation of a wave through a half-wave plate, decomposed into the fast (blue) and slow (green) components. The polarization is shown in red. The outgoing polarization is reflected through the fast axis, which for sapphire is the extraordinary axis. In a typical system neither component completes an integer number of oscillations in the material, as skeched here for simplicity.

coated on both sides with high density ceramic infused teflon, RT/duroid 6002[2], chosen for its index of refraction of $1.71 \sim \sqrt{3}$ and its low loss tangent of $\tan\delta = 0.0012$ in the ABS band.

RT/duroid is manufactured by melting teflon, mixing in ceramic particulates and then letting it cool back down under high pressure between two plates. It is about as flexible as teflon, and the added ceramic gives it a slightly rubbery feel. The final thickness of the material is determined by the distance between the plates, which can be adjusted in increments of 0.127 mm (0.005"). The optimal $\lambda/4$ thickness for the AR coating is 0.310 mm, so the 0.381 mm (0.015") sheet had to have 0.063 mm shaved off of it uniformly over its entire 855 cm^2 area. This feat was accomplished by Glenn Atkinson by first gluing the material to a large flat custom-made jig of aluminum to rigidize it and then machining it in the lathe. Due to the large variation of linear speed of the cutting tool over the 16.5 cm radius, two different angular speeds of

[2]Rogers Corporation, www.rogerscorp.com

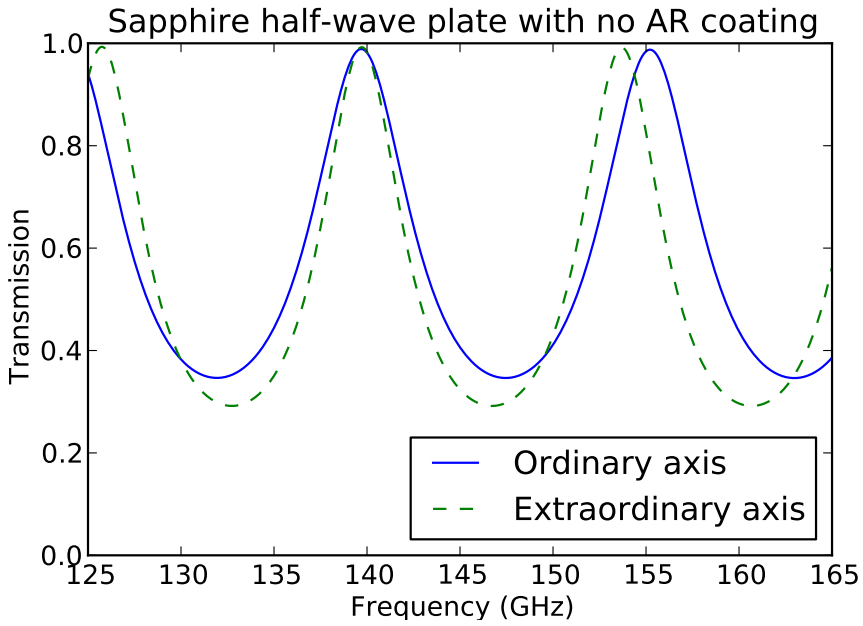

Figure 2.3: Transmission through 3.15 mm thick sapphire with no anti-reflection coating of polarized light parallel to the ordinary (slow) axis in solid blue and parallel to the extraordinary (fast) axis in dashed green.

the lathe were used to avoid tearing the material. The final sheet had a thickness of 0.31 ± 0.013 mm.

The glue of choice to adhere the RT/duroid to the sapphire was rubber cement, because it is sturdy, dries to a negligible thickness, and can also be removed if necessary by being soaked in acetone. To achieve a uniform thickness and avoid bubbles, a custom vacuum gluing jig was built. Each side was glued separately to ensure that the RT/duroid was centered on the sapphire. The transmission of the AR-coated sapphire was measured with a Fourier transform spectrometer built by Blake Sherwin and Mary Zhang. It employs a thermal source and an old iteration of an ABS detector, cooled in a test dewar. The sensitivity of the measurement is determined by the bandpass of the detector, which is $117 - 145$ GHz, approximately 10 GHz lower than the field detectors. The measured transmission at normal incidence compared to a simulation at the ABS central frequency of 145 GHz is shown in Figure 2.4. They match to within the error bars.

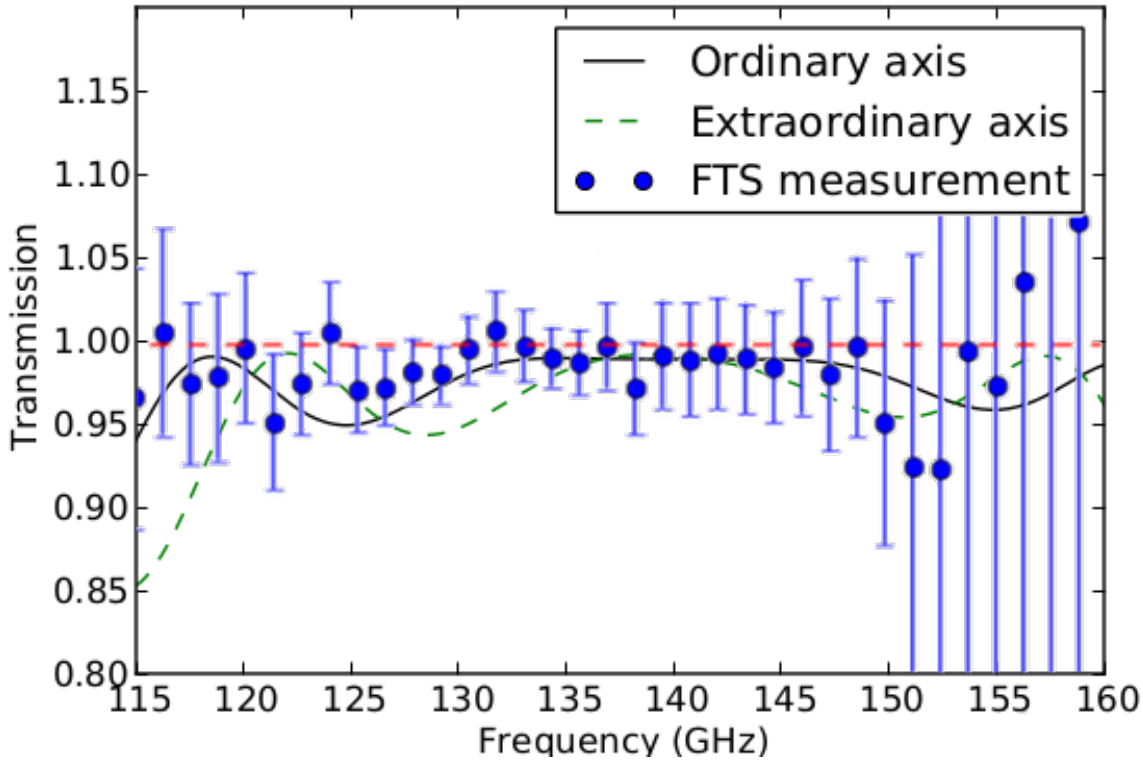

Figure 2.4: Measured transmission of the warm sapphire half-wave plate with optimal single-layer anti-reflection coating, 0.31 mm RT/duroid 6002. For comparison, the simulated transmission at 145 GHz is shown through the ordinary and extraordinary axes. The measurement was taken along a random axis using an FTS, and matches the simulation in the bandpass of the FTS detector, $117 - 145$ GHz, which is lower than the target bandpass of $127 - 163$ GHz.

2.1.2 Aperture

Having all the optics at 4 K reduces the loading on the detectors from emission from the reflector surfaces and from stray light and "spill" from the region around the optics. However, the requirement that they be inside the cryostat has the drawback that the aperture size is defined by the smallest opening in the optical path of the beam through the cryostat. The 30 cm diameter window is mounted in the center of the top lid. It is 0.3 cm (1/8") thick ultra-high molecular weight polyethylene[3], chosen for its high in-band transmission and its strength. It is AR-coated with porous

[3]Commercially available from McMaster-Carr

PTFE on both sides. Directly underneath the window, the 40 K and 4 K shells also have openings, on which are mounted and thermally sunk a series of quasioptical IR-blockers and absorptive low-pass filters which help reduce the thermal loading onto the 4K stage and the detectors. In ABS the openings at each thermal stage get progressively smaller, so that the smallest one is the 26.0 cm diameter 4 K filter ring mount, providing a common cold aperture stop for all detectors (Fig. 2.5).

The 4 K filter stack is composed of two absorptive IR blockers, a 2.54 cm (1") slab of polytetraflouroethylene (PTFE) and a 0.95 cm (3/8") slab of Nylon, and a quasioptical metal-mesh IR blocker. The overall thickness of the 4 K stack is geometrically constrained to avoid ray clipping. Nylon is much more absorptive than PTFE, and while it cuts over 99% of radiation above 1 THz, it also reduces the net in-band transmission by 2%. At 4 K, PTFE on the other hand is only an effective IR blocker above 6 THz, but it has a low in-band loss tangent of 3×10^{-4} and at 2.54 cm only cuts 3.7% in-band. It is used to block most of the IR radiation and reduce the thermal loading onto the Nylon, allowing it to equilibrate at a lower temperature. The centers of the PTFE and Nylon filters were measured to be 16 K and 6 K, respectively, during a test run in the field. Both of these pieces are AR-coated with Zitex G-115[4], porous teflon with an index of refraction of ~ 1.2 [6].

A second 2.5 cm thick piece of AR-coated PTFE is used as a filter at the 40 K cryogenic stage to reduce the loading onto the 4 K filter stack. At this higher temperature the absorptivity of PTFE is 90% above 800 GHz and greater than 99% above 3 THz. A total of 9 single-layer metal mesh IR-blockers are mounted above and below the PTFE. These are grids of aluminum squares patterned on 6 μm thick Mylar substrates, and are nearly purely reflective lowpass filters. The cutoff frequencies are determined by the grid spacing, and are 1.6, 2.0, and 3.1 THz. Finally, an additional 1.6 THz metal-mesh IR-blocker is placed just beneath the window at 300 K[16].

[4]Norton Films, http://www.norton-films.com/

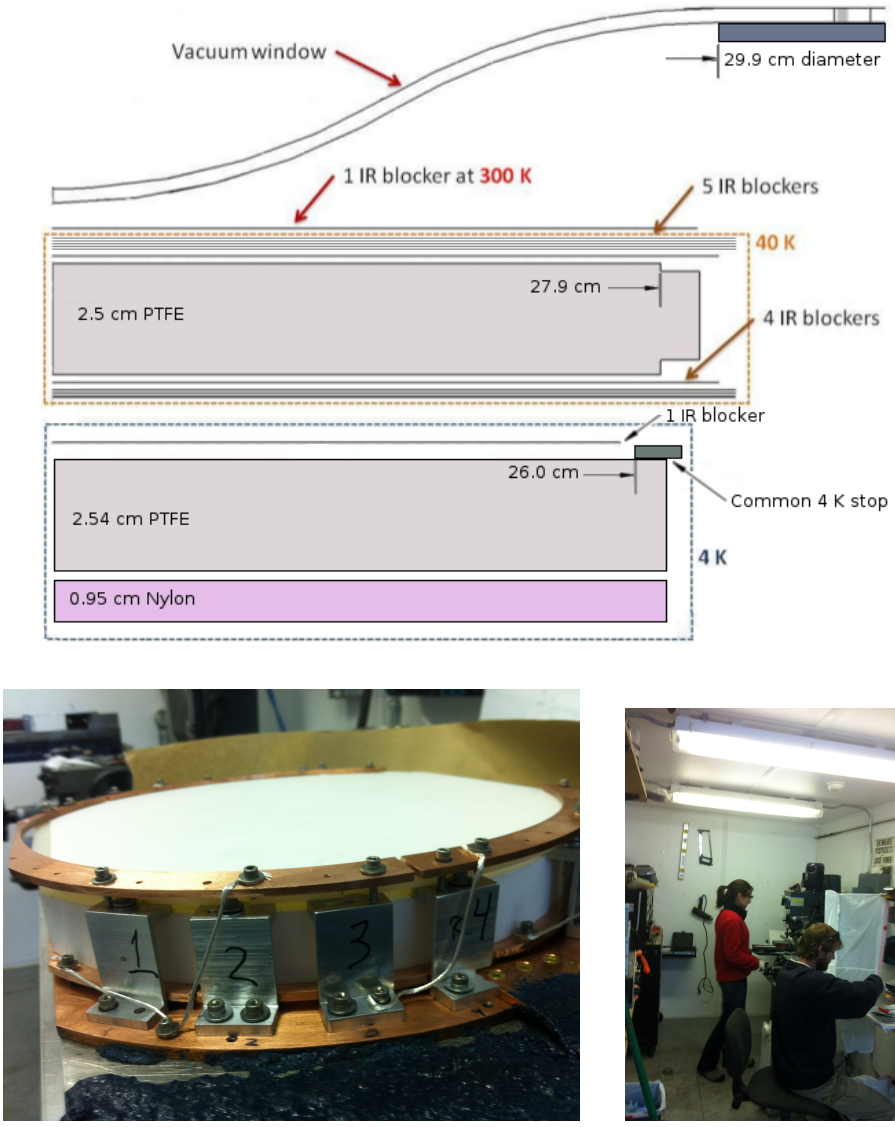

Figure 2.5: Top: Complete layout of the ABS aperture inside the cryostat. The IR blockers are single-layer square grids of aluminum on 6 μm mylar with cut-off frequencies of 1.6, 2.0 and 3.1 THz. Both PTFE filters and the Nylon filter are AR-coated with Zitex. The 4 K cold stop has a diameter of 26.0 cm (10."). Bottom left: The 4 K filter stack pictured upside down from its orientation in the cryostat, so that the PTFE is below the Nylon. The Z-brackets (numbered) allow for the plastics to differentially contract from the copper mount rings. Copper-tin alloyed wires are used to thermally sink the copper rings holding the PTFE and Nylon in place. Before the stack was mounted in the cryostat, aluminum tape was used to seal the sides and prevent radiation from leaking out from between the layers. Bottom right: Machining at the ABS site. The author milling the Z-brackets and Tom Essinger-Hileman tapping the holes for the mount.

2.1.3 Focal Plane

The focal plane is mounted next to the primary, at a 78° angle from the plane of the primary. Its 240 feedhorn-coupled polarimeters are mounted in 24 triangular pods of 10 each, and tile it hexagonally (Fig. 2.6). The numbering scheme used to label the pods and feedhorns is shown in Figure 2.7. To reduce edge effects and maximize the optical efficiency through the aperture, there is a slight concavity of the focal plane. Each pod is placed at a unique angle depending on its location in the focal plane, ranging from zero in the center to 4° at the edge, so that the rays from each central feedhorn pass through the center of the aperture stop. To achieve these unique angles the pods are mounted on the focal plane support (FPS), a spider web-like structure which was custom made using a 5-axis milling machine. The FPS is mounted in a hexagonal support (hex). To isolate the 300 mK stage from the 4 K surroundings, it is suspended using 635 μm thick Kevlar string, a good thermal insulator, from the 1 K hex, which is in turn suspended from the 4 K hex on the focal plane mount.

2.1.4 Pods

In addition to providing structural support for the feedhorns and detectors, the aluminum shells of the pods, which are superconducting below 1.2 K, provide magnetic shielding for the magnetically sensitive readout circuits within. The feedhorns with the detector chip emerge through the front of the pod interface plate, which keeps each detector at its optimal angle, minimizing the beam mismatch between the two orthogonal polarizations. Each pod's readout circuit board has two triangular rigid sections connected by a flexible bridge. One side is glued to the back of the interface plate and has 10 holes in which the detector chips lie. The detector signal and heater lines are traced from this section over the bridge and onto the other, which houses the interface chip with the shunt resistors and the Nyquist inductors, as well as the mulsiplexing (mux) chip. To further magnetically shield the SQUIDs, two niobium sheets

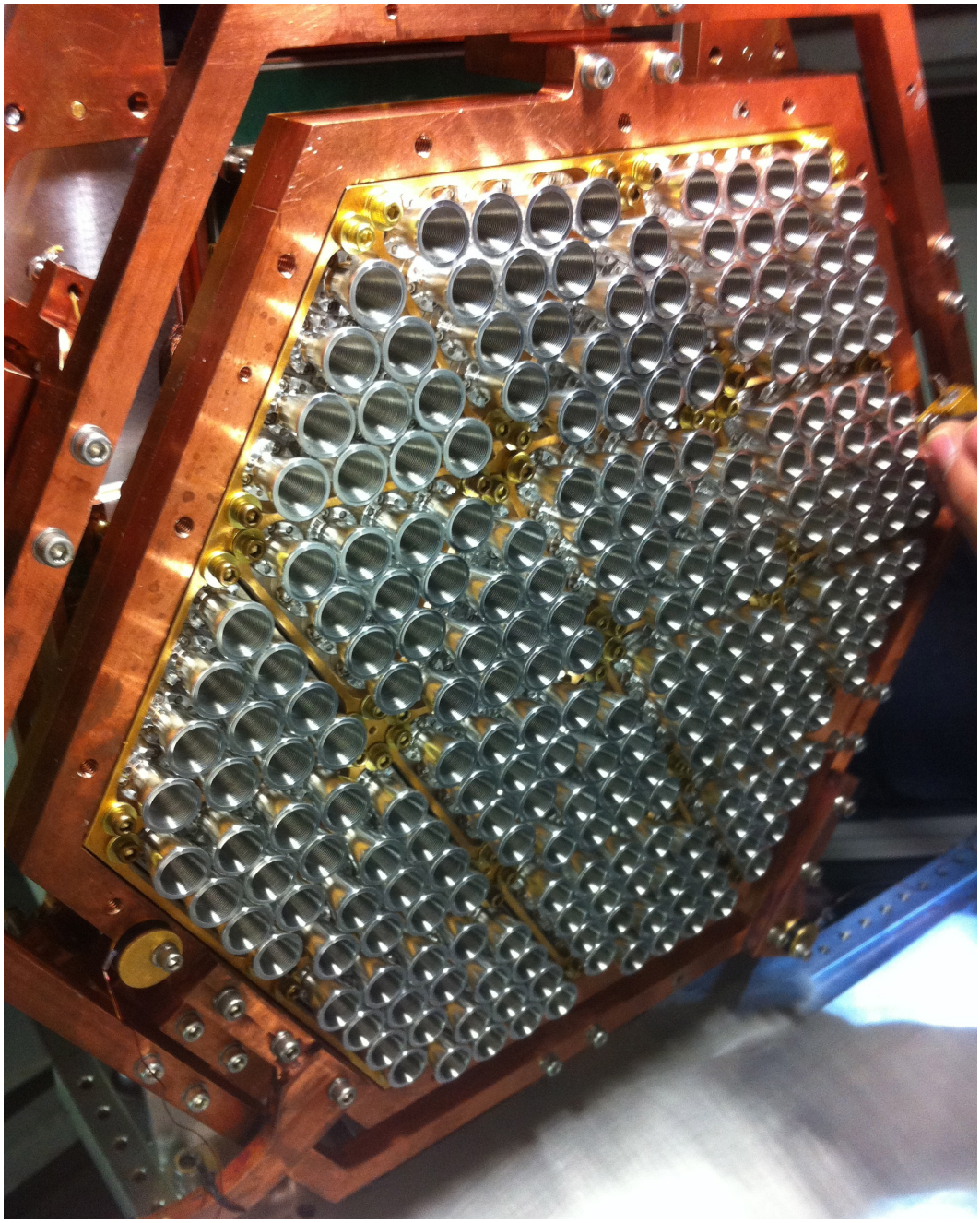

Figure 2.6: The focal plane is shown here with all 24 pods of 10 feedhorns each. The gold-plated copper focal plane support (FPS) can be seen between the pods. The FPS is mounted in the 300 mK hex, which is thermally coupled to the ^{3}He pot via the cold finger, which can be seen in the lower left corner along with the ROx thermometer. The 300 mK hex is nested in the 1 K hex with a kevlar suspension system, part of which can be seen here. The 1 K cold finger and ROx can be seen in the lower right corner of the focal plane. The 4 K hex is directly behind the 1 K hex, and part of it can be seen in the upper left corner of the photo. The aluminum in the lower right corner is part of the primary reflector plate, the curved part of which is outside of the frame of the photograph. The numbering scheme for the pods and feedhorns is shown in Figure 2.7.

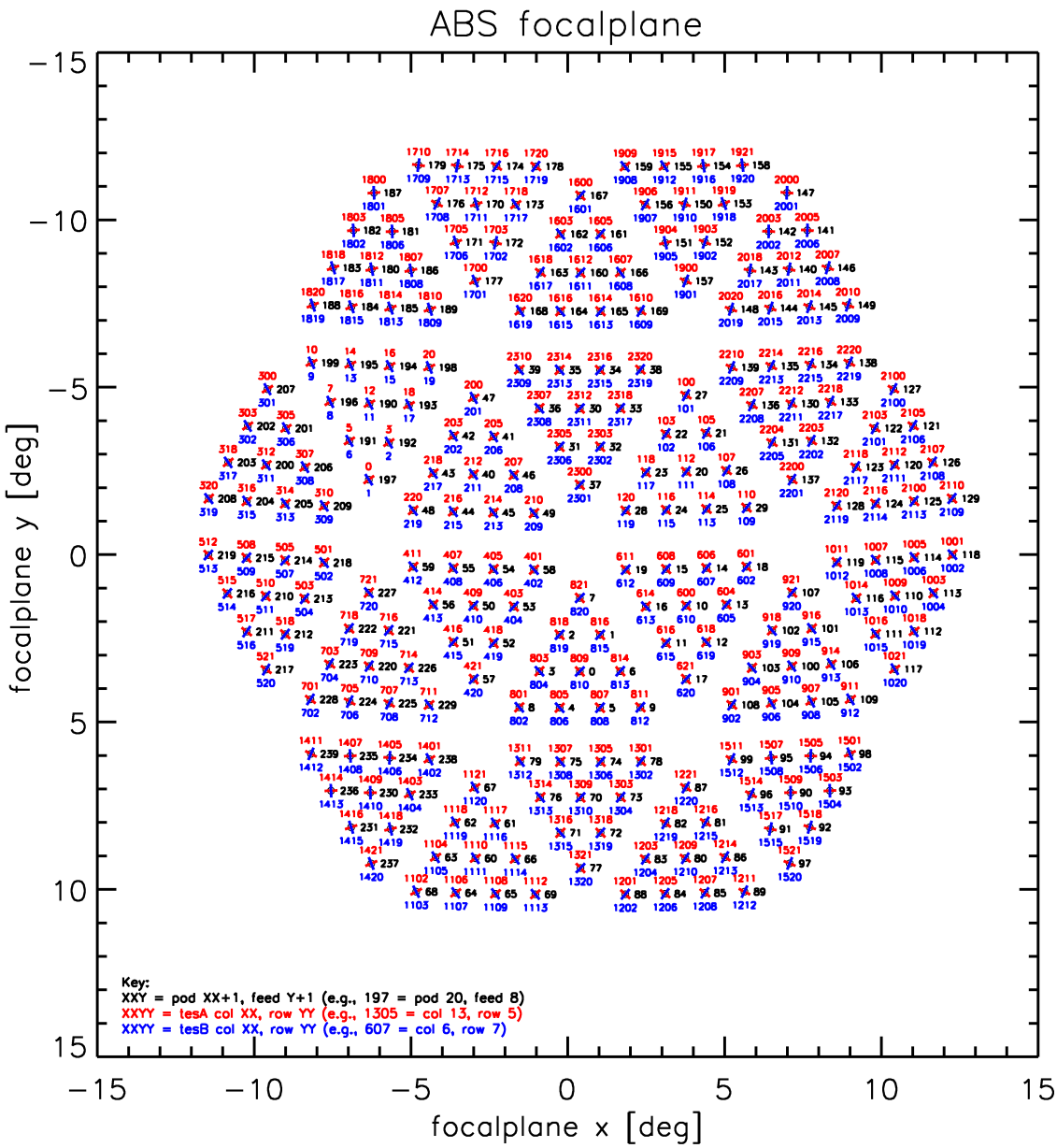

Figure 2.7: A map of the designed detector offsets from boresight, as well as the polarization angles of each pair. The red ticks and numbers signify TES As, and the blue TES Bs. The last two digits signify row number and the first two digits, assuming leading zeros, column number. TESes sharing an address line are said to be in the same row, and those in the same pod are said to be in the same column. Columns 0-3 and 16-23 comprise the 'top' half, and columns 4-15 the 'bottom' half. The detectors are displayed according to their physical position in the focal plane (Fig. 2.6), and so the projection onto the sky is flipped in elevation, indicated by the flipped y-axis. The 'top' half in fact looks lower on the sky than boresight, and the 'bottom' looks higher. Figure courtesy of Mike Nolta.

are installed above and below the mux chip. The electrical connection between circuit board and detector chips is made through aluminum wirebonds, done by Bert Harrop at Princeton. The flexible bridge is then folded, so that the two triangular sections overlap and fit into the aluminum pod casing directly behind the feedhorns[16, 3].

2.2 Cryogenics

Three closed cycle sorption refrigerators are used to cool the detectors and optics below the pulse tubes' base temperature. Our refrigerators were originally designed by Mark Devlin's group at the University of Pennsylvania[11]. At Princeton they were constructed, characterized, and optimized by Judy Lau for the C-Cam instrument [24]. One ^{4}He sorption refrigerator backs the ^{3}He fridge that cools the focal plane to ∼300 mK, while the other ^{4}He fridge cools the support structure of the focal plane and the detector cable heat sinks to ∼750 mK.

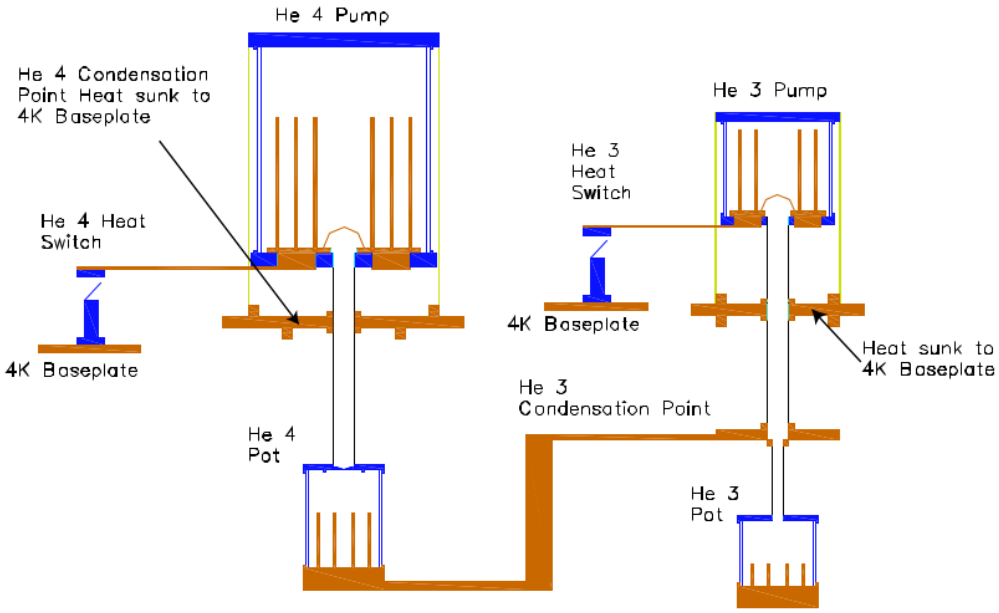

Figure 2.8: Schematic of the ^{4}He1 and ^{3}He refrigerator system used to cool the focal plane to ∼300 mK. The ^{4}He2 fridge is identical to the ^{4}He1 fridge, except that its pot is connected to the 1 K hex of the focal plane support. Figure from [24].

Sorption refrigerators cool by evaporation, lowering the pressure above a liquid allowing the higher energy molecules to escape, and thus cool the liquid until the vapor pressure equals the pressure above the liquid. Each of the ^{3}He/^{4}He sorption fridges is a cylinder with a condensation plate in the middle, a pot for collecting the condensate at the bottom, and a charcoal sorb at the top (Fig 2.8). At the start of the cycle, the charcoal is heated to 40 K to expel the helium, while the ^{4}He condensation plate, which is thermally connected to the 4 K baseplate, condenses the ^{4}He into the pot. The ^{4}He charcoal is then cooled by the baseplate via a heat switch to less than 10 K, at which point it starts pumping on the helium vapor, cooling the pot to $\sim$750 mK. This is below the condensation temperature of ^{3}He, and so the same process can be repeated with the ^{3}He fridge, whose condensation plate is thermally connected to the ^{4}He pot. With no thermal load, the ^{3}He pot reaches a minimum temperature of 218 mK.

Two annealed copper fingers, 0.64 cm (1/4") diameter and about 60 cm long each, are used to thermally couple the focal plane and its support structure to the 300 mK and 1 K pots. The fingers terminate in a flattened region termed the "spatula" to maximize the contact area with the focal plane hexes (Fig. 2.9). Ruthenium

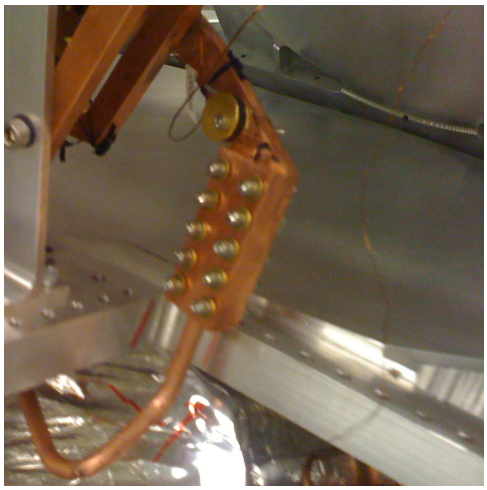

Figure 2.9: The 300 mK spatula, and just above it, a Ruthenium Oxide (ROx) temperature sensor.

Oxide temperature sensors (ROx's) were used to measure the load curves of the refrigerators and the thermal coupling coefficients G between the various joints. They were measured directly in the cryostat, with the optics and focal plane support (FPS) in place and with the window replaced with a reflective cover. The loads were applied with heaters on the 300 mK and 1 K stages of the focal plane, and the temperatures at the multiple joints were measured (Fig 2.10). The target temperature for the focal plane, i.e. the pod, is 300 mK, which is achieved as long as the extra thermal and optical loading on the 300 mK stage from the detectors and the open window do not exceed 10 μW. In the field, the base temperature of the focal plane is just below 300 mK. However, the scanning motion creates temperature spikes at the turn-arounds. Thus we run by servoing the temperature to 315 mK, and at low elevations where this effect is amplified, we servo to 330 mK. The temperature of the ^{3}He pot is 245 mK, consistent with a 17 μW loading on the focal plane.

2.3 Feedhorns

Corrugated feedhorns are often used at far infrared and microwave frequencies because they feature low sidelobes, and isometric beam patterns, where the received power is a function only of the angle from the axis of the horn to a good approximation. In addition to maximizing the efficiency, beam isometry also results in low cross-polar response, on the order of -30 dB, as compared to -20 dB for smooth wall circular horns [28]. This is particularly important for polarimeters, since a higher cross-polar response effectively decreases the polarization signal.

Achieving an isometric co-polarization beam pattern requires that the aperture electric fields in the horn also be isometric, a direct consequence of the fact that they are the Fourier transform of the radiated fields[28] . The only non-trivial field that satisfies this is the linear field, which also ensures zero cross-polarization. This

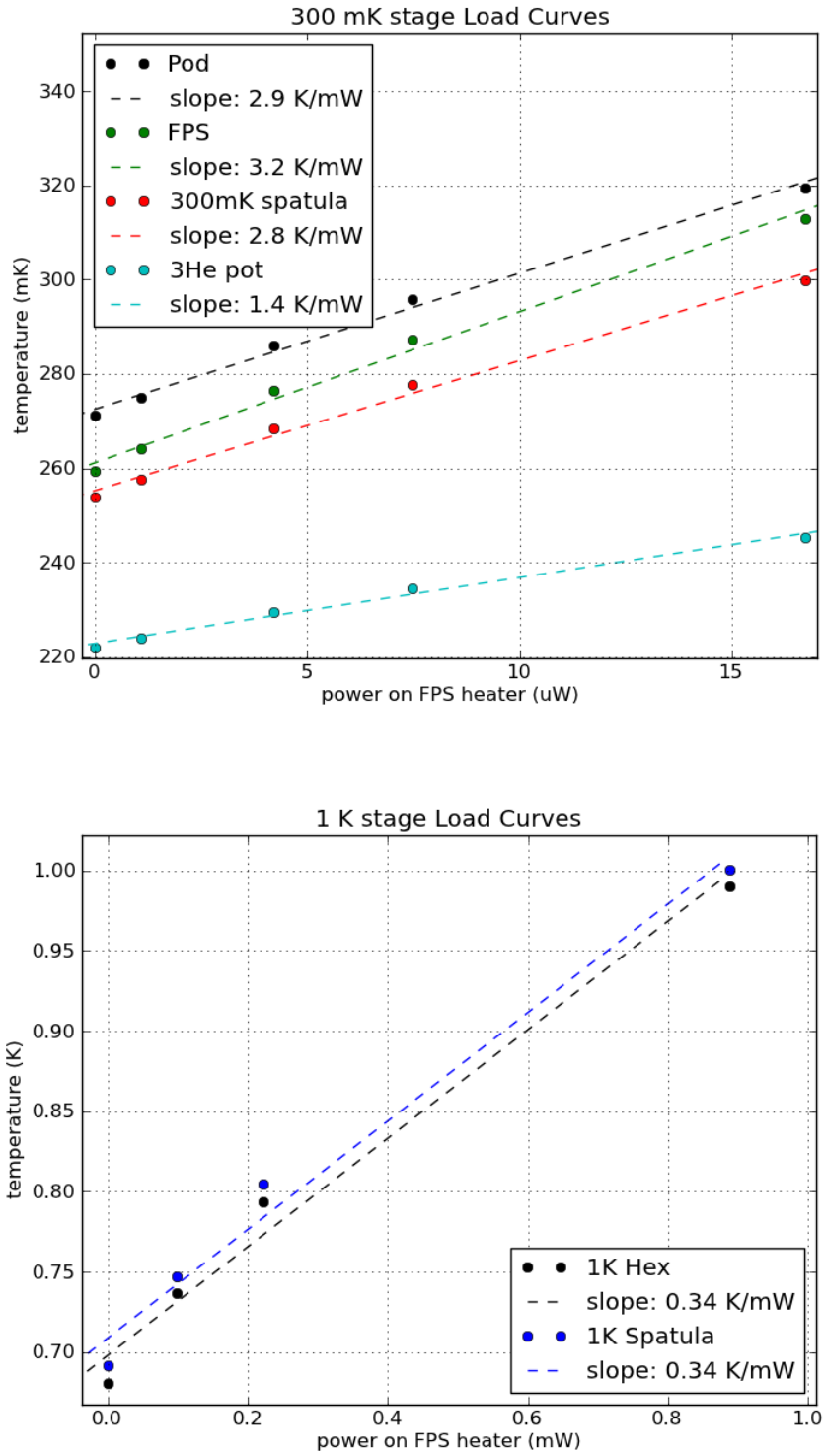

Figure 2.10: ^{3}He and ^{4}He refrigerator system load curves taken while the window of the cryostat was replaced with a reflective plate. The heaters were on the focal plane support (FPS) and the 1 K hex, respectively. The temperature gradient through the systems is clearly visible.

cannot be achieved with smooth-walled conductive feedhorns, since they only support pure transverse electric (TE) or transverse magnetic (TM) modes which have curved aperture field lines (Fig 2.11a). Only a hybrid mode, one that has both electric and magnetic field components in the direction of propagation, can produce nearly linear aperture fields (Fig 2.11b).

Corrugated feedhorns are one of two types of 'hybrid-mode feedhorns.'[5] The corrugations act as short circuited transmission lines, and if they are quarter wavelength deep, the short circuit at the end of the corrugation is transferred to an open circuit at the corrugation boundary. For corrugation spacing that is small enough compared to the target wavelength, the effect of the ridges can be ignored and the walls of the feedhorn can be approximated to a smooth surface with infinite impedance. This boundary condition allows hybrid modes to propagate through the feedhorn.

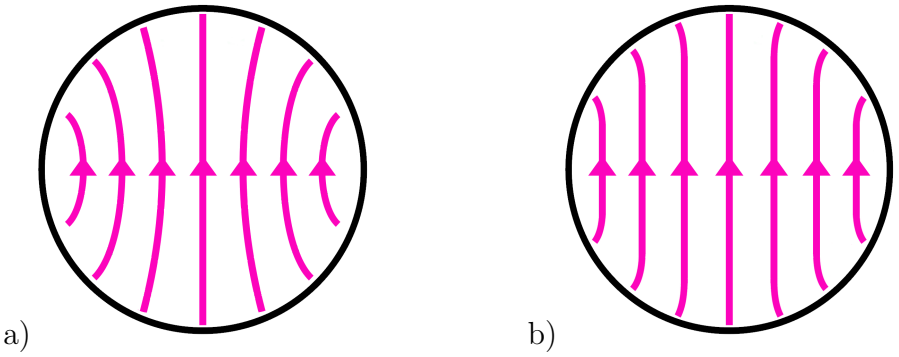

Figure 2.11: *Left* : The dominant transverse electric (TE_{11}) mode in a cylindrical waveguide. The lines represent the electric field lines in a cross-section of the waveguide where they are maximum. *Right* : Nearly linear electric field lines of the hybrid HE_{11} mode, supported by corrugated feedhorns. The linearity yields an isometric co-polarization beam pattern and low cross-polarization response. Figure adapted from [28] .

2.3.1 Design

The four aspects of a corrugated feedhorn that determine the radiation pattern and efficiency are the aperture diameter, the flare angle, the corrugations, and the throat.

[5]The other type is the dielectric-cone feedhorn, not discussed here.

The aperture diameter and flare angle together determine the FWHM of the copolar beam pattern and the variation of beam width over a range of frequencies[9]. The corrugation depth determines the central frequency, at which the E and H plane patterns are most similar, and the cross-polar response minimum. The transmission line model discussed above suggests that the optimal depth for a particular wavelength is $\lambda/4$, however owing to the annular shape of the corrugation wall, in practice this may vary from 0.25λ to 0.3λ. The corrugation spacing needs to be such that there are sufficient number of corrugations along the guide walls to mimic a continuous surface impedance; four corrugations per free space wavelength are usually sufficient [28]. Finally, the throat of the horn, usually the first 10 corrugations, serves to match the impedance of the waveguide to the $\sim \lambda/4$ deep corrugations. The first slot is half a wavelength deep, having zero impedance according to the transmission line analogy and matching the smooth-walled waveguide, and then the depths slowly taper to the nominal depth.

The performance of corrugated horns can be very accurately predicted using the "modal-matching" technique: the horn is divided into a series of short cylindrical waveguide sections and the fields are matched at each junction between sections. The exact geometry of the feedhorn can be investigated and the effect of a single corrugation of the wrong depth can be observed. The ABS feedhorn was designed by Jennifer Lin using the modal-matching program CCORHRN, which was developed by YRS Associates [37]. It was optimized for beam isometry and low voltage standing wave ratio (VSWR) in the observation band $127 - 163$ GHz. The VSWR is the ratio of the amplitude of a partial standing wave at an antinode to the amplitude at an adjacent node in a transmission line. A partial standing wave is a superposition of a standing wave and a transverse wave, or equivalently, two waves traveling in opposite directions of the same frequency but different amplitude, such as an incoming wave

and a partially reflected wave. It is related to the complex reflection coefficient Γ as

$$VSWR = \frac{1 + |\Gamma|}{1 - |\Gamma|}. \tag{2.1}$$

The VSWR is greater than or equal to unity, where unity signifies perfect transmission, and infinity signifies total reflection. Figure 2.12 shows the simulated VSWR of the horns overplotted with the Atacama atmospheric transmission in the ABS observation band. The simulated E and H plane beam profiles at central frequency 145 GHz (2 mm wavelength) are shown in Figure 2.13.

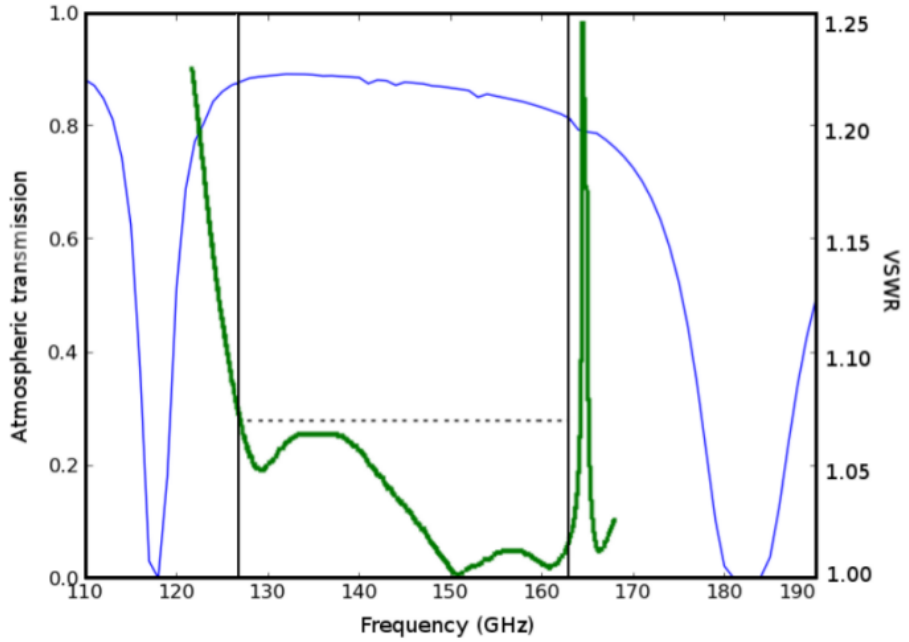

Figure 2.12: Atacama atmospheric transmission (thin blue) plotted with the voltage standing wave ratio (thick green). The ABS observation band is between the two vertical lines ($127 - 163$ GHz) and is bounded by the O_2 absorption line centered at 117 GHz and the H_2O absorption line centered at 183 GHz. In-band, the atmospheric transmission is typically above 80% and the VSWR does not exceed 1.07.

The feedhorns were manufactured from aluminum alloy 7075 by Glenn Atkinson, Master Instrument Maker in the Princeton Physics Department machine shop, on a computer numerical control (CNC) lathe. The waveguide is 1.6 mm in diameter and the corrugations are only 250 μm wide and up to 984 μm deep (Fig 2.14), and

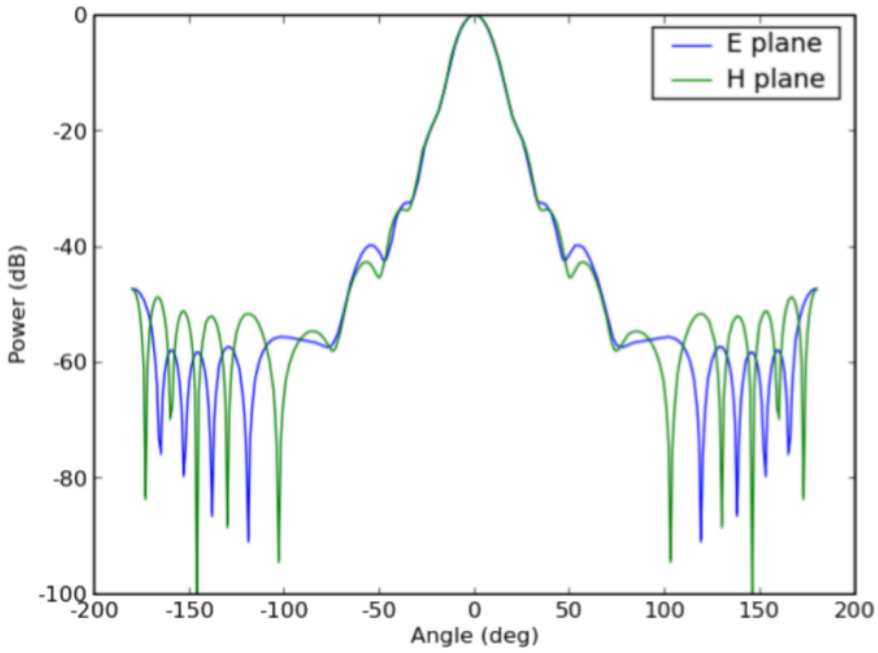

Figure 2.13: E− and H−plane simulated beam maps for the ABS feedhorn geometry at central frequency 145 GHz, as calculated by CCORHRN. The FWHM is 15.5° for the E−plane and 16.0° for the H−plane. The forward gain is 21.5 dB and the solid angle is 0.24 sr.

were made using a custom-made 90° steel tool. This extremely narrow tool could not be made long enough to reach the corrugations near the wave guide, and so the feedhorns were machined in two parts, called the detector package and the feed, which were bolted together prior to any testing, to ensure that the joint was accounted for in the beam maps. A total of 254 feedhorns were manufactured.

2.3.2 Room Temperature Testing

After machining, the feedhorns went through a cleaning process to rid them of grease and chips that may have been stuck in the corrugations. The first step was the standard ultra-sonic cleaning with isopropanol and acetone followed by a blow dry. A fiberscope was then used to find any remaining chips, and a flexible handle microbrush with a 1.5 mm diameter cylindrical polyurethane foam tip, slightly smaller

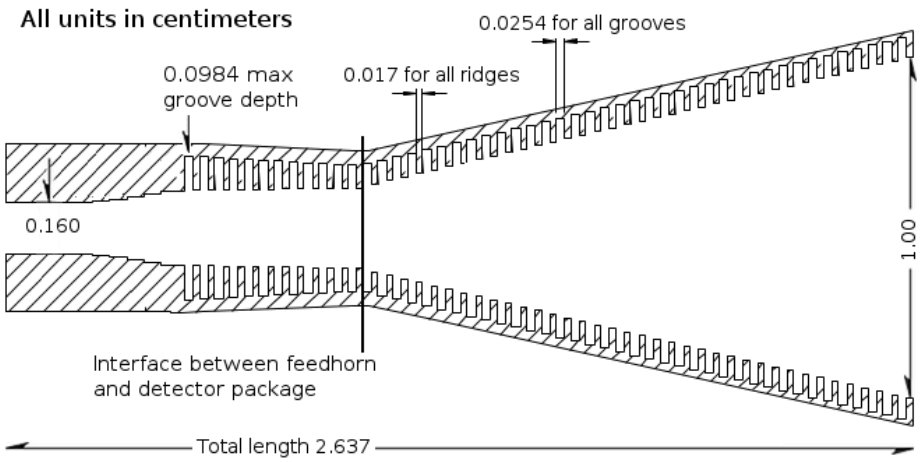

Figure 2.14: Cross-section of the cylindrically symmetric ABS feedhorn and waveguide. A solid black line indicates where the joint is between the detector package on the left and the feedhorn on the right. The steps in the throat provide a smooth transition For a full drawing of the design see [16].

Figure 2.15: Photo of an ABS feedhorn with a penny for scale. The corrugations are partially visible.

than the waveguide, was used to brush them out. A torque screwdriver was used to incrementally tighten the 3 screws at the joint to ensure that the two parts were coupled in a flat, symmetric manner.

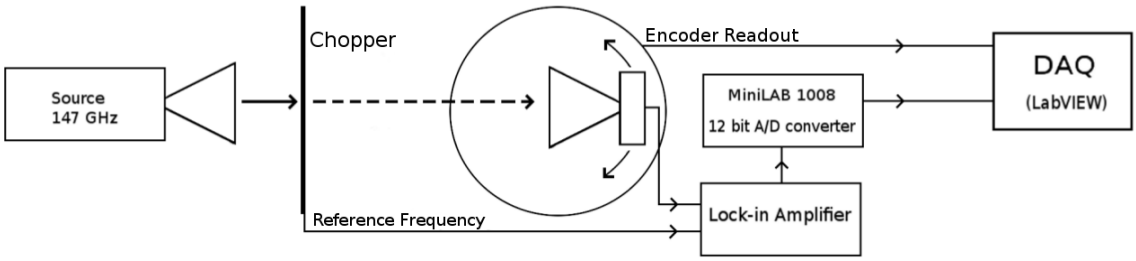

Figure 2.16: The room temperature testing apparatus was built to test one feedhorn at a time, using a narrowband 147 GHz source and a waveguide broad band detector (110-170 GHz). The source is stationary, and the horn and detector are attached to a rotary table, the axis of which is aligned with the phase center of the horn. The output of the detector is a voltage proportional to the signal. The signal from the source is chopped and filtered through a lock-in amplifier to eliminate out of band noise.

A room temperature beam mapping station was used to measure the beam maps of each feedhorn (Fig 2.16). The source used was a narrowband 147 GHz Gunn diode oscillator[6], and was placed in the far field approximately 0.6 m from the feedhorn being measured. The feedhorn, coupled to a D-band ($110-170$ GHz) diode detector[7], was attached to a rotary table, the axis of which was aligned with the phase center of the horn. The source was modulated at ~ 135 Hz by a chopper, and the output from the diode was passed through a series of pre-amplifiers and passband frequency filters before going to the lock-in amplifier. The total electronic gain was on the order of 10^5. Eccosorb foam was used to cover all surfaces and the wall to minimize interference from reflections and bring the noise floor to below -30 dB. The E$-$ and H$-$plane beam maps of all feedhorns were measured individually, an effort that was aided by several Princeton undergraduate summer students: Cheryl and Nicole Quah, Rutuparna Das[8], Sean Frazier and Dragos Potirniche.

[6]Zax Millimeter Wave Corporation
[7]Pacific Millimeter Products
[8]visiting from MIT

2.3.3 Selection

To compare the measured beam maps to the simulations, a 2-dimensional analog of the solid angle was used:

$$a = \frac{2\pi \int_{-\Theta}^{\Theta} F|\sin\theta|\,\mathrm{d}\theta}{2\pi \int_{-\Theta}^{\Theta} F_{\mathrm{sim}}|\sin\theta|\,\mathrm{d}\theta}, \tag{2.2}$$

where F is the measured beam map and F_{sim} is the simulated beam map for that plane. Introducing the absolute value and integrating over $\pm\Theta$ is equivalent to taking the average of the two halves of the measured beam map, which may not be the same. For an ideal beam map, the above integral would be taken over the full range $[-\pi, \pi)$, and in that case the numerator would be the solid angle of the beam assuming it is isometric. In this set-up the noise floor is at around -30 dB and dominates the beam maps at angles larger than 30°. For this analysis we use $\Theta = 25°$, which includes the main peak and the first side lobe, cutting off at -22 dB.

Several measures were used to identify faulty feedhorns. First, the feedhorns with too wide of a beam were identified by looking at a_E or a_H. Wide beams increase the loading onto the detectors from scattered light within the cryostat. Next, the feedhorns with excessive left-right asymmetry of either their E− or H−plane map were identified by looking at the difference of a_{left} and a_{right}, obtained by taking the above integral from $[-25°, 0°)$ and $(0°, -25°]$, respectively. This was done to ensure that feedhorns like number 224 (Figure 2.17 d.) with average overall width but with a big side lobe are also discarded. The effect of the asymmetrical testing station, with the wall on one side and the open room on the other, is on the order of 4% in $a_{\mathrm{left}}/a_{\mathrm{right}}$. Finally, the isometry of the beam pattern was tested by looking at the ratio a_E/a_H.

The means and standard deviations of each of those three measures of the 254 horns machined are shown in Table 2.1. A 3σ cut-off was imposed on each measure,

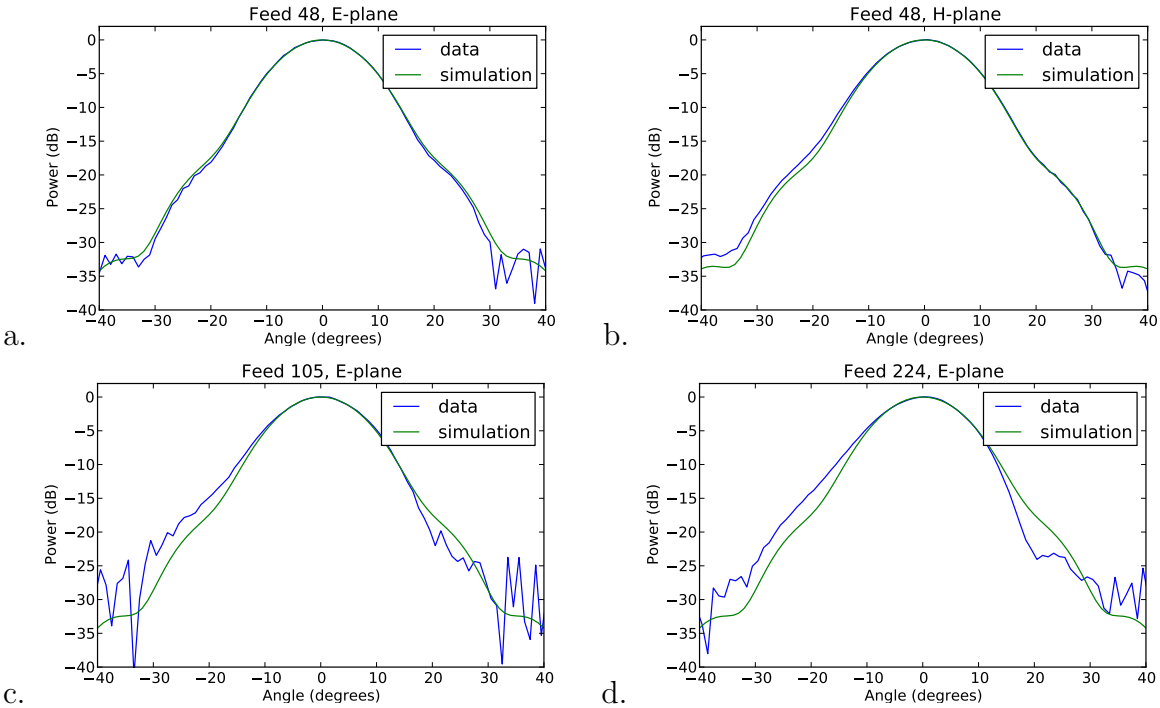

Figure 2.17: Examples of beam maps taken with the room temperature testing station. Panels a and b show the E− and H−plane patterns, respectively, of one of the best feedhorns. The E−plane matches the simulation to better than 1% and the H−plane is better than 4%. Panel c : An E−plane agreement of 13%, just barely passing the 15% cutoff. Panel d : Example of a beam map whose overall beam width matches the simulation to within 5%, but was discarded due to its left-right asymmetry of about 20%.

resulting in a total of 34 horns being discarded. The tops and bottoms of the discarded horns were taken apart and reassembled in different pairs and measured, and in this way the remaining 20 horns were obtained with desirable beam patterns. The final distribution of E− and H−plane solid angles of the horns can be seen in Figure 2.18, with the discarded ones highlighted, and the average beam maps are shown in Figure 2.19.

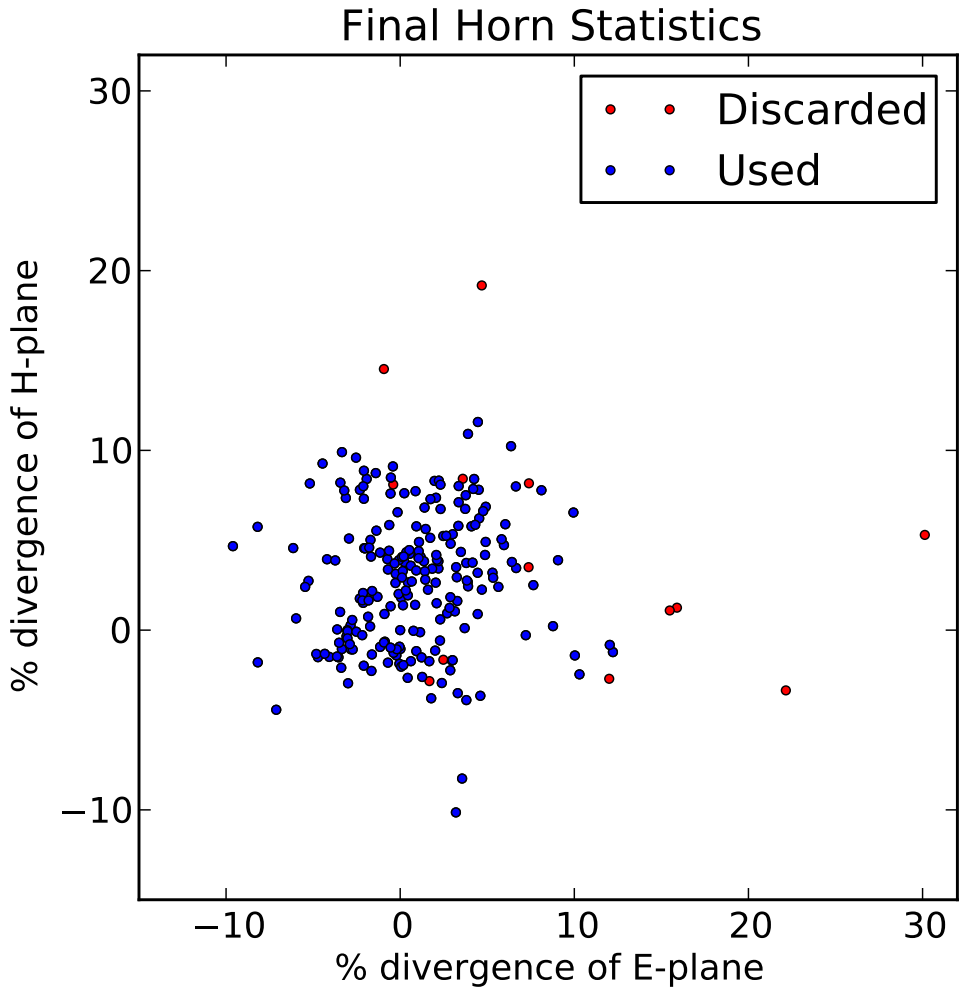

Figure 2.18: Scatter plot of the E− and H−plane divergences for the ABS feedhorns. The blue dots represent the ones that are currently in the focal plane. The red dots represent the ones that were discarded. The red dots that are not outliers displayed left-right asymmetry, which is not visible in this plot. Further, out of the 34 original feedhorns that were discarded, 21 are not shown here because they were discarded based on their E−plane beam map alone, and their H−plane map was not taken.

Measure	Original 254 Horns	Final 240 Horns
E−plane beam width	$1.7 \pm 5.3\%$	$1.2 \pm 3.4\%$
H−plane beam width	$3.5 \pm 4.0\%$	$3.4 \pm 3.8\%$
Left-right asymmetry	$4.9 \pm 3.6\%$	$4.3 \pm 2.9\%$
Isometry	$1.5 \pm 5.8\%$	$1.6 \pm 4.8\%$

Table 2.1: The final statistics of the feedhorn beam patterns most critical to ABS compared to the initial ones. The E− and H−plane beam widths are compared to their respective simulations. The left-right asymmetry compares the left half of the beam map to the right, and the isometry compares the width of the E−plane beam map to that of the H−plane.

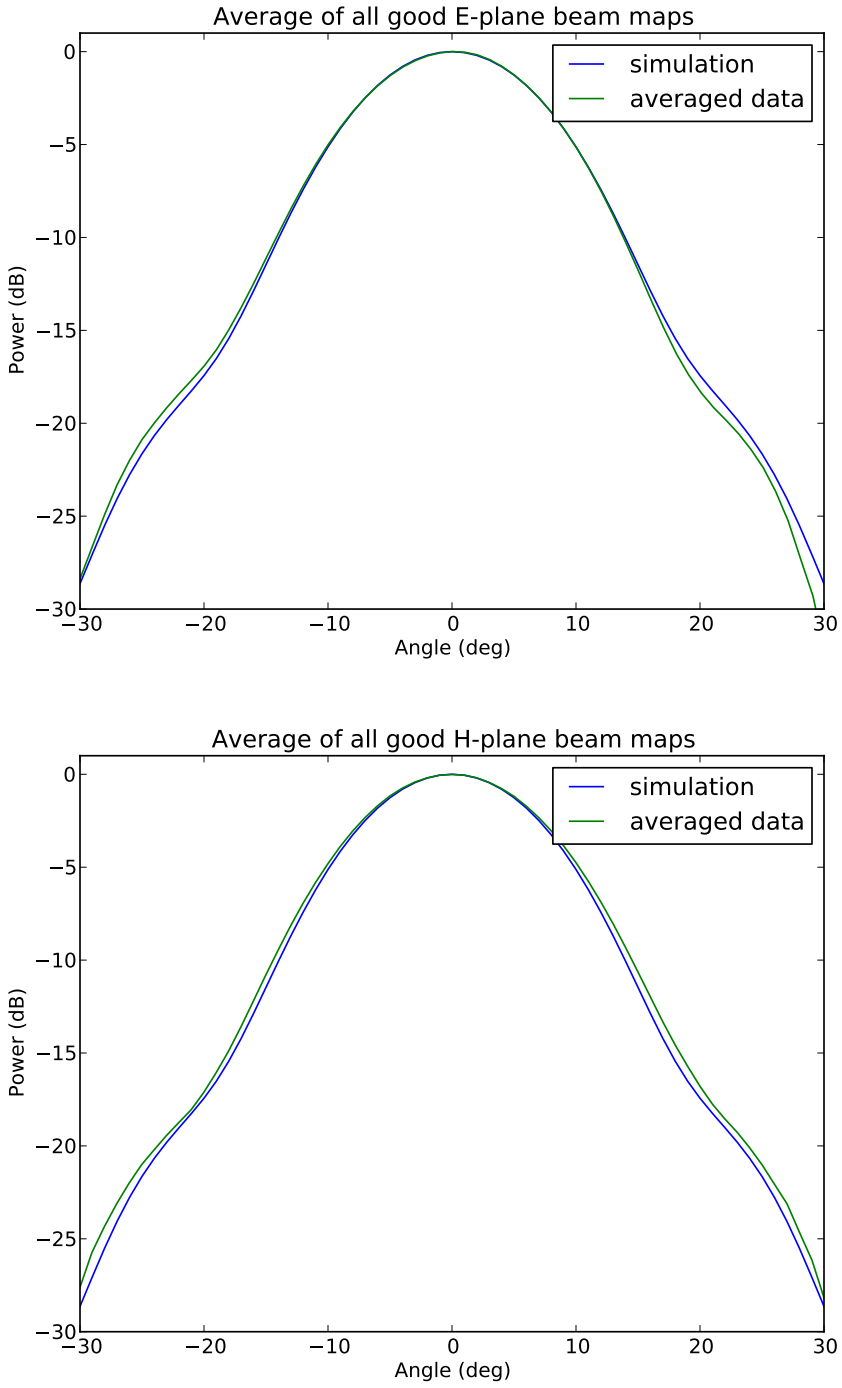

Figure 2.19: The average E− and H− plane beam maps of all good feedhorns are both within 1% of the simulated beam maps.

Chapter 3

Data Characteristics

3.1 First Season Observations

Landing at the site on Cerro Toco on 16 January, 2012, ABS took 6 weeks to deploy and saw first light on 27 February. The first CMB data with half-wave plate (HWP) and baffle mounted were taken on 13 March. The last day of the first season of CMB observations was 3 January 2013. Out of the 296 days total, 94 days were lost due to long-term mechanical repairs. Of the remaining 202 days (4848 hours), ABS was observing for 2,600 hours, or 54% of the time, and of those, 1,938 hours (40%) were spent observing CMB data. The other 662 hours were spent observing the galaxy, calibrating off point sources such as the moon, planets, the polarized galaxy Tau A and the embedded cluster RCW 38, doing scans in elevation called sky dips, and various other tests. While ABS is running consistently, the recycling of the fridges takes 8 hours and each cycle lasts approximately 40 hours, completing a full 2 day period. This means that an additional 11% of the 202 days was devoted to cycling the fridges. Current versus voltage curves (IV curves) for each TES and SQUID biasing before each observation account for an additional 77.7 hours, or 3.0%, leaving 32% ($\sim$1550 hours) to smaller scale maintenance and adjustments of software

and hardware. Table 3.1 summarizes the major events that occurred throughout the season, and Table 3.3 breaks down the total observation time by target.

3.1.1 Observation Strategy

ABS employs a few types of observation strategies, depending on the purpose and target of the observation. The primary one, used when observing targets, involves scanning in azimuth at a constant elevation, and letting the sky move across the field of view with time. With constant elevation scans (CESes), the atmosphere thickness through which the signal travels is constant and the cryogenics remain stable for the duration of the scan. Complementary central azimuth angles around south are used to catch the same patch of sky as it rises and sets and scan it in complementary directions. This cross-linking technique reduces systematic effects in the mapping due to the scan and improves the sampling of CMB modes perpendicular to the scan direction. The elevations and central azimuth angles used for the four CMB fields are summarized in Table 3.2. The scan speed and width are 0.75°/s and 10°, respectively, as measured by the azimuth encoder, so the speed and width on the sky depend on the elevation (Tab. 3.2).

Field A is the primary and largest CMB field, and so a single elevation with complementary azimuth angles is required to observe it. The other three fields are smaller, and move through the field of view faster, thus requiring four different observation points, two while rising and two while setting, to observe them efficiently. ABS also observes smaller, point-like targets, like the moon, Saturn, Jupiter, Venus, the galaxy Tau A and the star cluster RCW 38. The purpose of these observations is to calibrate the pointing of the telescope, the optical efficiencies of the detectors, and, for the polarized Tau A, to calibrate the polarization sensitivity of the focal plane and the absolute detector polarization angles.[1]

[1]Once we start seeing the CMB in the data, the final calibration will come from comparing to WMAP [7] and the latest Planck results[32].

Date	Event
17 January	ABS lands at the Cerro Toco site.
7 February	First cool down, no focal plane.
27 February	First light, without HWP, baffle, or ground screen.
28 February	Saw the moon.
9 March	Half-wave plate mounted.
11 March	Baffle mounted.
12 March	Tightened HWP spring.
13 March	Database starts.
14 March	Scanning motor turn-around smoothed.
22 March	HWP airbearing screws adjusted.
23 March	Added heat tape to HWP enclosure
2 April	Saran wrap tests.
4 April	1" wire-grid measurements.
7 April	Ground screen mounted.
9 April	Sequential data acquisition set up.
16 April	Saran wrap layer inserted at base of baffle
16 - 21 April	HWP compressor burned and replaced.
23 April	HWP air bearings tuned.
16 May - 6 June	Down time due to crushed pulse tube line.
8 June	TES biasing problem fixed after down time.
10 June	HWP working again after down time.
6 July	Bump starts being visible in 1/f noise, also in dark squids.
8 July	Cable wrap problems start.
8 - 21 July	Down time due to bad weather and cable wrap problems.
5 August	Azimuth drive malfunction.
7 August	Clutch alignment problem discovered.
8 August	Switch to scanning with azimuth motor.
25 August	Blackened baffle loading tests.
	TOD lengths changed to 150 frames = 5 min.
31 August - 11 Sept	Down time to make baffle shiny.
14 September	Scan motor reinstalled with newly aligned clutch.
	Azimuth motor motion smoothed.
19 September	9° azimuth shift discovered.
27 September	Adjusted the azimuth encoder offset by 9 degrees.
20 November	Problem with elevation brake and clutch not working.
25 November -	Down time due to cable wrap.
27 December	
3 - 21 January	FTS and wire-grid measurements.
21 January	End of season, ABS turned off.

Table 3.1: A log of major events and changes that took place during ABS's first season of observation.

Field	CES elevation (°)	Central azimuth (°)	Scan width (°)	Scan speed (°/s)
Field A	46.5	130	6.8	0.52
	46.5	230	6.8	0.52
Field B	44.5	67	7.1	0.53
	63.5	30	4.5	0.33
	63.5	330	4.5	0.33
	44.5	293	7.1	0.53
Field C	64.5	106	4.3	0.32
	78.5	117	2.0	0.15
	78.5	225	2.0	0.15
	64.5	254	4.5	0.32
Field D	51.5	126	6.2	0.47
	70.5	148	3.3	0.25
	70.5	210	3.3	0.25
	51.5	233	6.2	0.47

Table 3.2: Elevation and azimuth positions of CMB field observations. Angles are defined so that an elevation of 90° points to zenith, and azimuth of 0° points north. Field A is large enough that it only requires two complementary observation positions, and the other three fields require four.

3.1.2 The Data

Each detector acquires data at a frequency of 200 Hz, which is stored as time ordered data (TOD) in binary dirfiles named

$$\underbrace{1339311311}_{\text{ctime}}\_\text{dirfile}.\underbrace{003}_{\text{seq}}$$

where ctime is the unix time stamp of the start time of the TOD, and seq represents the sequence number of the TOD within a particular CES. Figure 3.1 is an example of a CES. Each TES is named after the row and column, with TESes sharing a pod being in the same column, and TESes sharing a bias line being in the same row (Fig. 2.7). There are 24 columns and 22 rows. In addition to the 20 TESes (2 for each of the 10 feed horns), each row has 2 "dark" SQUIDs which are not connected to any

Target	num_frames	Time (seconds)	Time (hours)	% total
Field A	2,402,165	4,804,330	1,334.5	51.3
Field B	356,828	713,656	198.2	7.6
Field C	503,904	1,007,808	279.9	10.8
Field D	729,523	1,459,046	405.3	15.6
Moon	256,267	512,534	142.4	5.5
Saturn	62,384	124,768	34.7	1.3
Jupiter	42,527	85,054	23.6	0.9
Venus	8,474	16,948	4.7	0.2
Tau A	62,008	124,016	34.4	1.3
RCW 38	40,744	81,488	22.6	0.9
sky-dips	53,566	107,132	29.8	1.1
testing	159,726	319,452	88.7	3.4
All targets	4,679,650	9,359,300	2,599.8	100.0
IV curves		279,720	77.7	3.0
Fridge cycling			~ 300	11

Table 3.3: Time spent on each target during the first observation season. Fields A, B and D are CMB fields and Field C is a galactic field. The 'testing' category includes side lobe measurements using the sun, and various tests like baffle tests, azimuth and scan motor tests, saran wrap tests and HWP tests. The IV-curves and fridge cycling are not included in the total time for the targets, and the fridge cycling time is an estimate.

TESes. The readouts from the dark SQUIDs provide useful information about the non-optical noise present in the detectors.

We varied the length of TODs during the season until finally settling on 5 minutes. At first, following ACT, we aimed for approximately 15 minutes, but because we wanted to have the number of samples in a TOD close to a power of 2, we chose 2^{17} samples = 10.9 minutes. To increase the versatility of observation schedules this number was soon decreased to 2^{16} samples = 5.46 minutes. It was soon realized that when a TOD was stopped in the middle of a 2 second frame, the rest of the 400 samples in that frame were given the value zero, creating a slight complication when combining multiple TODs together to form a CES. For greater ease in combining

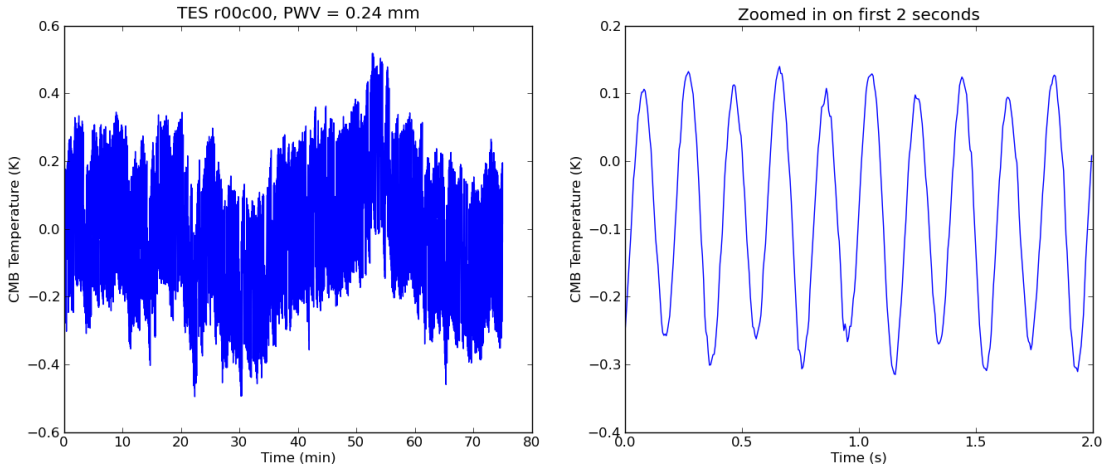

Figure 3.1: An example of a constant elevation scan (CES) from TES r00c00. It is 75 minutes long and consists of 15 TODs of 5 minutes each, with no time gap between them. At 200 Hz data acquisition rate, there are 9×10^5 samples. The sched_id and sched_subid of this CES are (1983,13), and it was taken on 6 October, 2012. This was a very good observing night with a PWV of 0.24 mm. The slow drift is dominated by changes in atmospheric brightness. The high-frequency noise is dominated by the half-wave plate modulation of the incoming polarization, seen in more detail on the right. The y-axis is the change in temperature in CMB equivalent units.

TODs, their length was further reduced to a round number of 60,000 samples, or 5 minutes, eliminating the creation of null samples.

The raw units of the TODs are DAC counts, representing the current that is flowing through each TES after being amplified by a series of SQUIDs. To convert DAC counts to observed temperature in the sky one must take into account both electrical and optical properties of the system. The responsivity, converting DAC counts to power fluctuations on the TES islands, are derived from the IV curves taken at the start of each CES[3]. To get from power on the TES to temperature on the sky, the optical efficiency ϵ is required, which is a combined efficiency taking into account the detector on-chip efficiency, and the loss from the feed horns, optical filters, window and baffle. They are discussed in more detail in Section 3.4.

To better understand the fluctuations visible in the timestream, it is useful to look at the power spectrum. Figure 3.2 shows the power spectrum for the timestream

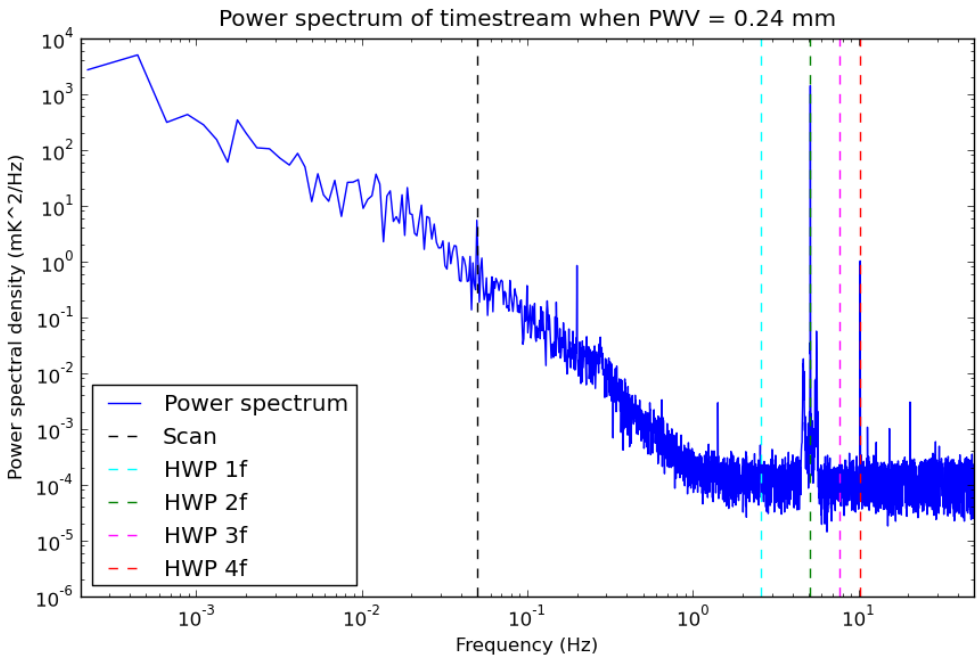

Figure 3.2: Power spectral density of a constant elevation scan, the timestream of which is shown in Figure 3.1, taken when the PWV = 0.24 mm. The scan frequency is denoted by the vertical dashed black line. The knee frequency, at which the dominant source of noise changes from being the atmosphere to detector Johnson noise, is at around 1 Hz. The half-wave plate frequency at 2.56 Hz and its multiples, up to even the 7f, are visible. By far the largest peak is the $2f$ peak, which is about 100 times the $1f$ peak.

shown in Figure 3.1. The best fit line is removed from the timestream and the Welch apodization function is applied prior to taking the FFT, to reduce ringing created by the abrupt jumps at the beginning and end of the file. The atmosphere, described in more detail in section 3.2, is the source of the $1/f$ noise visible at frequencies lower than ~ 1 Hz. We avoid taking CESes longer than 75 minutes due to the possibility that the SQUID tuning may drift. Above 1 Hz, the detector white noise dominates over the atmosphere, and the HWP frequency and its harmonics are clearly visible. The scan frequency is visible at 0.02 Hz

3.2 The Atacama Atmosphere

The atmosphere is the primary foreground of the CMB signal, as it is an absorber-emitter of radiation in the ABS band. The dominant lines are due to excitation of rotational modes of water molecules centered at 183 GHz and one of the two lines of a molecular oxygen doublet centered at 117 GHz[2]. The ABS band was chosen to be in the relatively transparent region between these lines, but it is still affected by the tails of the distributions. The O_2 level in the atmosphere remains relatively constant over time, whereas the H_2O level depends on the weather. The level of water is quantified by the precipitable water vapor (PWV), the depth of water in a column of the atmosphere, if all of that water were precipitated as rain, and as such is measured in units of length.

Figure 3.3 shows how the transmission of the atmosphere in the nominal ABS band depends on the PWV, and in turn how the temperature of the sky depends on PWV. In fact, only one half of the focal plane has the nominal pass band; the second half was fabricated with a pass band shifted higher by 15 GHz, namely $142 - 178$ GHz, making it more sensitive to the water line. The nominal and shifted halves coincide with the 'top' and 'bottom' halves of the focal plane as defined in Figure 2.7. Figure 3.4 shows the distribution of PWV during the 2012 observation season, and Figure 3.5 overplots the PWV and detector RMS over the first season.

Before we calculate the expected loading on the detectors, we first introduce some telescope definitions. For each feed horn we define the normalized beam pattern, similar to section 2.3, but taking into account the optics of the telescope. The normalized beam pattern is defined as

$$P_n(\theta, \phi) = \frac{P(\theta, \phi)}{P_{\max}}, \tag{3.1}$$

[2]The other line is at 60 GHz

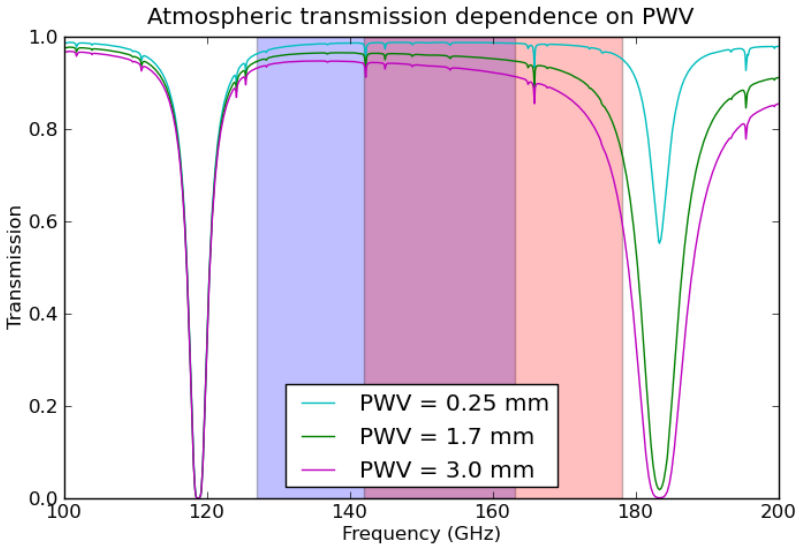

a.

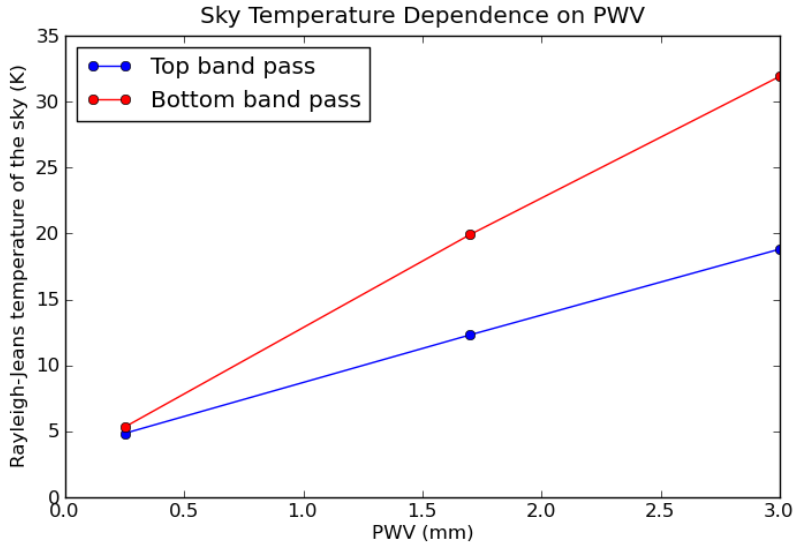

b.

Figure 3.3: Top: The transmission of the atmosphere for several values of precipitable water vapor (PWV). The nominal ABS band (top half) is shaded in blue and the shifted band (bottom half) in red. As expected, the O_2 line at $\sim$ 118 GHz stays constant, whereas the water line at $\sim$ 183 GHz gets bigger and wider for higher PWV. The data are according to the Chajnantor Weather Model[1], taken from the ALMA site on the Chajnantor plateau a few miles from the ABS site, at an altitude of 5,040 m. Bottom: The temperature of the sky as seen by the two groups of detectors when they are both at 55° elevation, assuming top-hat bandpasses with with a 35 GHz width. Due to the 15 GHz shift, the bottom half of the detectors see a hotter sky than the top half for a given elevation, an effect which is amplified with higher PWV.

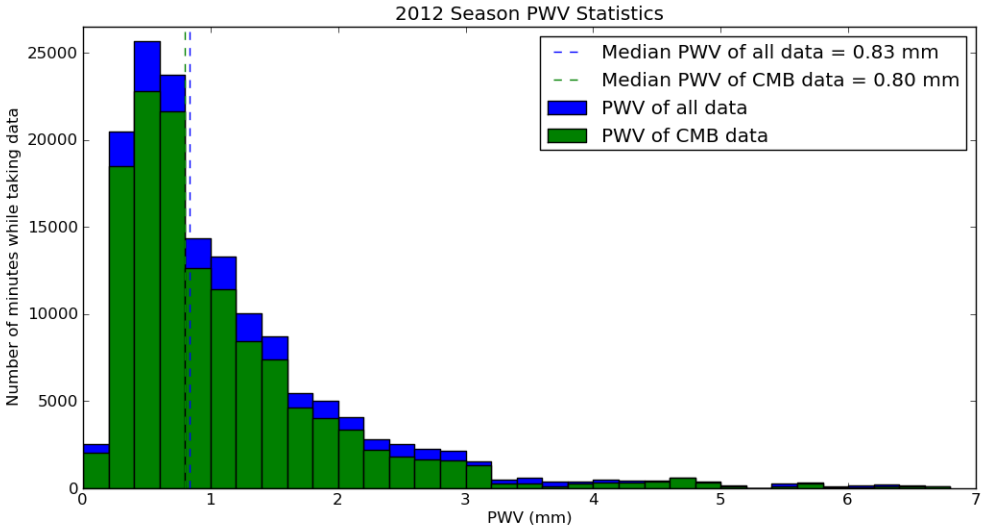

Figure 3.4: A histogram of the number of minutes of data taken over a range of PWV. The blue indicates all data, and green is CMB data only. The lower and upper quartiles were at 0.50 mm and 1.39 mm, respectively. PWV data are taken from the APEX weather monitor, which is shut down during storms and for a period of time following the storms, until their site is accessible again. An additional 112 hours of CMB data were taken during which PWV data were not available.

where $P(\theta, \phi)$ is the power received from a given direction relative to the center of the feed horn. The beam solid angle is then defined as

$$\Omega_b = \int \int_{4\pi} P_n(\theta, \phi) \mathrm{d}\Omega. \tag{3.2}$$

The effective aperture parameter, A_e, describes how much power is captured from a plane wave arriving from the direction of maximum gain of a feed horn. If p is the surface power density of the plane wave and P_t represents the power deposited on the detectors, then $A_e = P_t/p$ in a system with no loss. A general relation for the effective aperture in terms of the beam solid angle for a single mode of radiation is given by

$$A_e = \frac{\lambda^2}{\Omega_\mathrm{b}}. \tag{3.3}$$

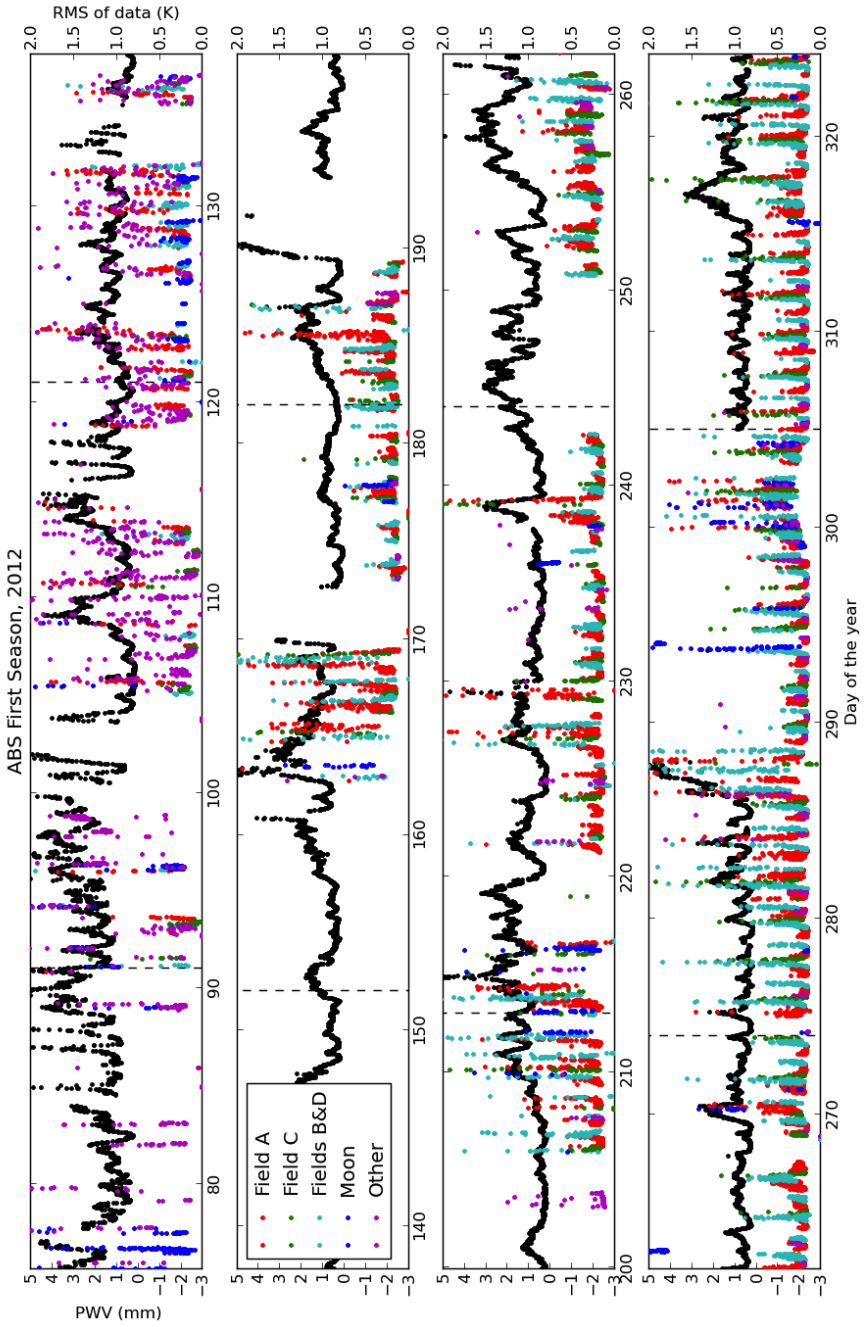

Figure 3.5: PWV (black) over the first season, and the RMS of a detector samples at 200 Hz in the top half of the focal plane, r00c00, with color coded targets. The diurnal variations in PWV are due to Easterly winds in the evenings which carry moisture from the Amazon basin. The gaps in the data correspond to the down times outlined in Table 3.1. The gaps in PWV are due to the APEX monitor shutter being closed during storms and sometimes for days afterwards, until their site is accessible again.

In other words, a more focused beam has a larger effective aperture than a wide beam.

Now we are ready to apply these definitions to the atmosphere. We model the atmosphere as a grey body, and since its temperature is $T_{\rm atm} \sim 270$ K, at 150 GHz where $\lambda = 2$ mm we can work in the Rayleigh-Jeans regime. We define the optical depth of the atmosphere with transmission coefficient T at zenith as $\tau = -\ln(T)$, and fractional air mass at elevation angle θ_{el} as $\alpha = \sec(90^\circ - \theta_{el})$, such that at zenith α is unity and increases towards the horizon. This is a good approximation for $\theta_{el} > 20^\circ$ using the slab model of the atmosphere. Then the intensity of the atmosphere is

$$I_{\rm atm} = \frac{2kT_{\rm RJ}}{\lambda^2}, \tag{3.4}$$

where $T_{\rm RJ} = T_{\rm atm}(1 - e^{-\tau\alpha})$ is the Rayleigh-Jeans equivalent temperature. The factor of 2 accounts for both polarizations. For the beamwidth per feedhorn of $\theta_{\rm fwhm} = 0.58^\circ$, the maximum variation of α across a beam, occurring at the lowest observable elevation of $\theta = 35^\circ$, is around 1% and can be approximated as a constant. The flux of power through the aperture arriving at a particular feed horn then is

$$S_{\rm atm} = \int_{\rm beam} I_{\rm atm} {\rm d}\Omega \simeq I_{\rm atm}\Omega_{\rm b}. \tag{3.5}$$

The ABS band is narrow enough that we can assume that the net flux is constant through the entire band, and equal to its value at the central frequency, $f_0 = 150$ GHz, or $\lambda_0 = 2$ mm. Doing so allows us to write the net power as

$$W = \int_{\Delta f}\int_{A} S_{\rm atm}(f){\rm d}f{\rm d}A \;\simeq\; A_e S_{\rm atm}(f_0)\Delta f \;\simeq\; 2kT_{\rm RJ}\Delta f, \tag{3.6}$$

where the last relation is in the Rayleigh-Jeans regime and uses the effective aperture relation from Eq. 3.6. It is worth noting that the effective aperture is different for each feed horn, since the angle between the center of each feed and boresight varies

from approximately 1° to 12° over the focal plane, which in turn affects the size of the physical aperture at the 4 K cold stop. This effect is countered by the variations in Ω_b for each feed, and so the final power incident on each feed is dependent only on its bandpass. According to this calculation, on a day when the PWV is 0.25 mm and the temperature of the atmosphere is 250 K, the loading onto the detectors should be around 4 pW when pointing at zenith.

This calculation assumes perfect optical transmission, while in reality we must multiply by an efficiency ϵ_i to get the actual power absorbed by detector i. This calibration is discussed in section 3.4.

3.2.1 Atmospheric Turbulence

The water vapor in the atmosphere acts not only to absorb radiation in the ABS band, but it also refracts the radiation which is not absorbed. To characterize the full effect of the refraction, one must consider the dynamic properties of the atmosphere. Turbulence causes the local density of water to vary across the field of view and over time. The result is that as the atmosphere moves across the field of view, fluctuations in the effective PWV for each detector causes temperature fluctuations in the timestream of the detectors.

According to the Kolmogorov model of turbulence (Tatarskii 1961), the power spectrum of the fluctuations in a large 3-dimensional volume is proportional to $\kappa^{11/3}$, where κ is the wave number of the fluctuations. The main assumption of the model is that the kinetic energy from larger scale fluctuations is almost entirely transferred to smaller scale fluctuations, being dissipated into heat only at the smallest, critical scale. Fluctuations which are large compared to the physical size of the system fall into the 2-dimensional regime, and their power spectrum is proportional to $\kappa^{-8/3}$.

The field of view of each detector, 0.58°, is small enough that the spatial inhomogeneities in the atmosphere due to turbulence are essentially frozen in time, i.e., they

form a fixed pattern, which blows across the field of view with wind. The relationship between the fluctuations' wave number κ and their frequency f in the timestream is proportional, and the constant of proportionality is determined by a combination of the scan speed and the wind speed, and so the $\kappa^{-11/3}$ and $\kappa^{-8/3}$ dependence of the power spectrum translate to $f^{-11/3}$ and $f^{-8/3}$ relation in the timestream power spectrum, for the 3- and 2-dimensional regimes, respectively. The physical dimension of the system in this case is the thickness of the atmospheric layer supporting the turbulent motions (Church 1995; Lay & Halverson 2000), on the order of a few kilometers. It is the source of the increased noise at low frequencies.

Figure 3.6 shows the effect of the atmospheric turbulence on the CES power spectra. the curves are the average of the power spectra of CESes taken in the PWV bins 0.24 ± 0.1 and 1.7 ± 0.1 mm. As expected, the overall power due to the atmosphere is greater for higher PWV. At frequencies below ~ 0.3 Hz the fluctuations follow the 2-dimensional model, and at slightly larger scales, corresponding to frequencies up to ~ 2 Hz, they slowly transition into the 3-dimensional regime. Above 2 Hz the detector white noise becomes the dominant source of noise.

3.2.2 Beam Overlap

To calculate the overlap of beams from adjacent feed horns, one must take into account both the finite aperture size and the full width half maximum (FWHM) of each beam. Considering only the former would give the overlap provided the beams were perfectly collimated. This is a good approximation for short distances, where (aperture size)/(distance from aperture) >> (angle between the beams). Considering only the latter gives the asymptotic overlap of the beams on the sky, where the aperture size is negligible (Fig. 3.7). For a more accurate description at intermediate distances, the beam profile must be convolved with the finite aperture size.

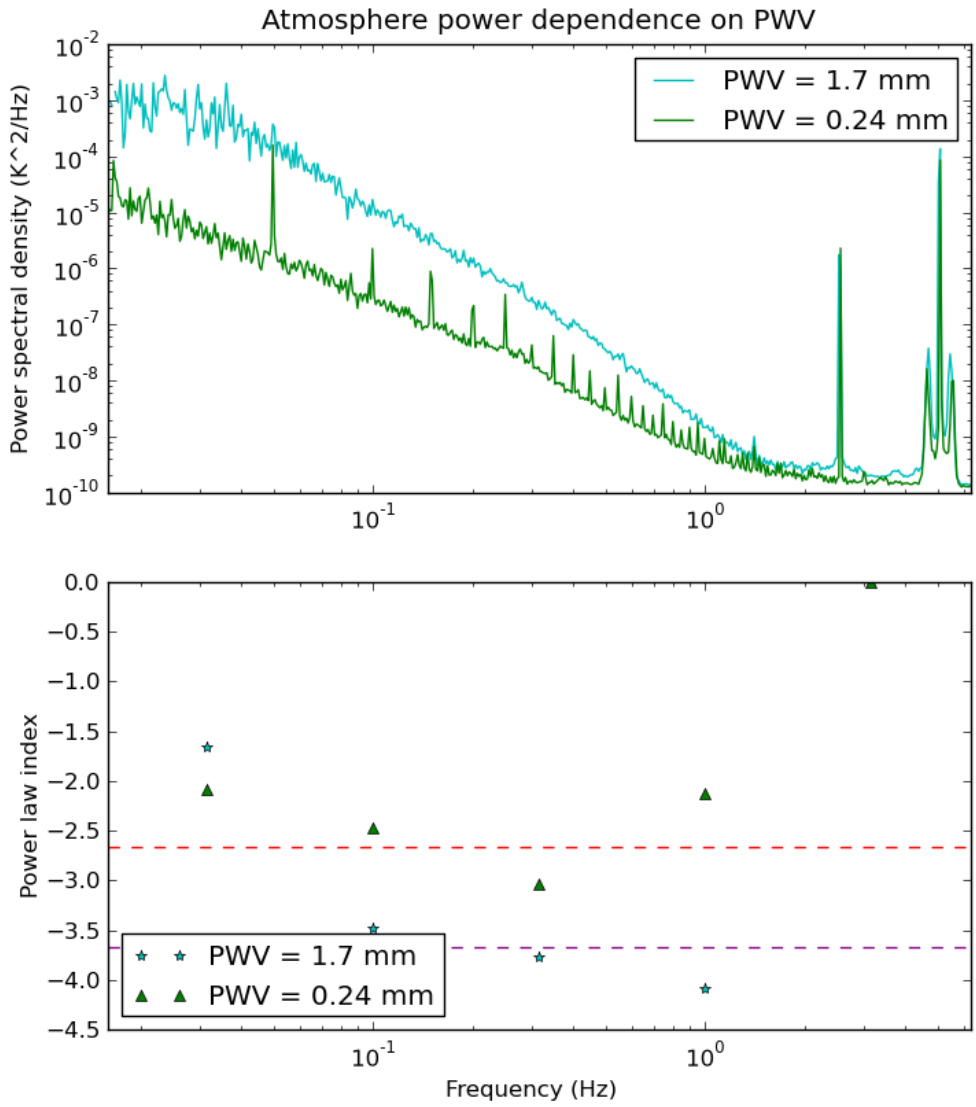

Figure 3.6: Atmosphere power dependence on PWV. The curves follow the expected pattern, with 2-dimensional turbulence at low frequencies or larger physical scales (red dotted line), and increasing to 3-dimensional at around 0.3 Hz (purple dotted line), until the detector white noise takes over at around 2 Hz The regular peaks are the scanning frequency and its harmonics. [14]

In spherical coordinates (θ, ϕ, r) where θ and ϕ are both defined to be zero at the center of the beam, the beam profile $F(\theta, \phi)$ is independent of r. The angular diameter, $\Delta\theta$ of the aperture of physical diameter a decreases as $\Delta\theta = 2\tan^{-1}(a/2r)$,

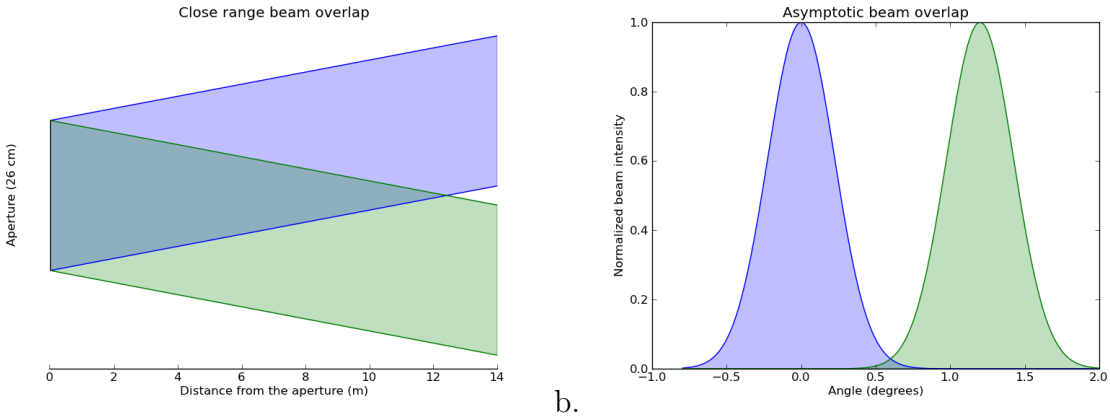

a. b.

Figure 3.7: Beam overlap in the limiting cases of being very close to the aperture (a), where the physical aperture size dominates the overlap, and very far from the aperture (b), where its physical size becomes negligible.

which in the limit of large r simplifies to the inverse square law for the solid angle $\sigma \sim \Delta\theta^2 \sim 1/r^2$.

For ABS, the aperture is the 4 K cold stop, with a diameter of 0.26 m. The FWHM of the beam was measured to be 0.58° and the angle between beams of adjacent feeds within the same pod is 1.2°. Approximating the beams as Gaussian, the overlap as a function of distance from the aperture is shown in Figure 3.8. Higher than $\sim$ 20 m above the aperture adjacent feed horns see almost non-overlapping regions of the atmosphere, which means that atmospheric fluctuations in the timestreams of detectors across the focal plane are uncorrelated, and the common mode will capture only large scale fluctuations, of angular diameter $> 20°$.

3.3 Demodulating the Half-Wave Plate

ABS employs a technique unique among ground-based telescopes to effectively see through the atmosphere. It uses a continuously rotating half-wave plate (HWP). This takes advantage of the fact that the atmosphere produces an unpolarized signal. As described in Chapter 2, the effect of a HWP on linearly polarized incident radiation

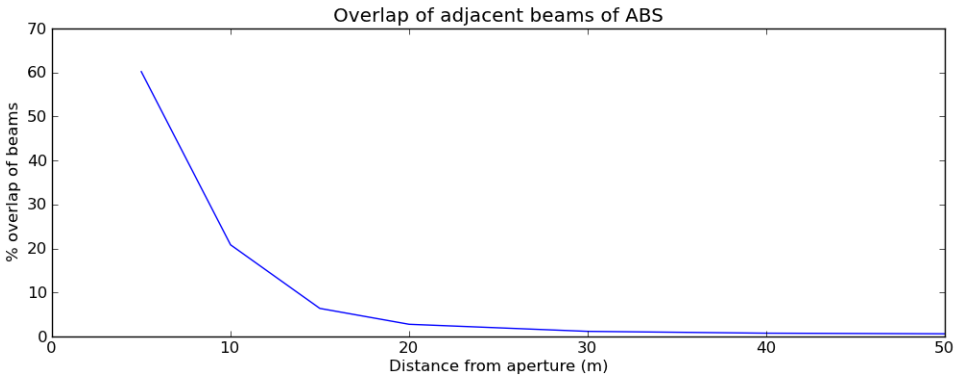

Figure 3.8: Percent overlap of beams from adjacent feed horns within the same pod of ABS. It takes into account both the finite aperture size and beamwidth by convolving a solid disk of angular size depending on the distance from the aperture, with a Gaussian beam. By 20 m above the aperture the overlap has fallen to 2.5%, meaning that the feeds are largely decoupled, and any common mode is due to large scale fluctuation in the atmosphere. The asymptotic overlap is 0.4%.

is to reflect the direction of polarization across the fast axis. For a HWP spinning at frequency f, the constant incoming polarization is modulated at $4f$ (Sec. 2.1.1). The ABS HWP rotates at ~ 2.5 Hz, bringing the modulation frequency up to ~ 10 Hz, well above the atmospheric knee frequency.

All of the celestial polarization signal is in the $4f$ peak in the timestream's power spectrum. The process of demodulation was adapted from that of the Dicke receiver [12] to extract all of the I, Q and U signals, by Akito Kusaka and Tom Essinger-Hileman, and is described briefly below. The modulated timestream can be written as

$$d_m = \mathrm{Re}[m(t)\{Q(t) + iU(t)\}] + \bar{T} + A(\phi),$$

where $\bar{T}$ denotes the background noise, including the $1/f$ atmospheric noise and the white detector noise, ϕ is the HWP angular position, and $A(\phi)$ is independent of input, representing the signal coming directly from the HWP including thermal emission and the effects of the mechanical system on the detectors. The first term contains all of the information, and $m(t) = e^{2i\pi f_m}$ with $f_m = 4f_{hwp}$. The timestream represents the projection of the polarization onto the orientation of the TES in question. The first

step is subtracting off $A(\phi)$, which is determined by binning the entire timestream by HWP encoder values, and low-pass filtering in HWP frequency space to include only the first ten harmonics. The next step involves multiplying the result with the complex conjugate of the modulation function, $e^{-2i\pi f_m}$, yielding

$$\begin{aligned} d_d(t) &= \frac{1}{2}\Big\{Q(t) + \cos(4\pi f_m)Q(t) + \sin(4\pi f_m)U(t) + 2\cos(2\pi f_m)\bar{T}\Big\} \\ &\quad + \frac{i}{2}\Big\{U(t) - \cos(4\pi f_m)U(t) + \sin(4\pi f_m)Q(t) + 2\sin(2\pi f_m)\bar{T}\Big\}. \quad (3.7) \end{aligned}$$

Effectively this makes two copies of the polarization signal, shifting one to $2f_m$ and the other to its original frequency, prior to its being modulated. In addition, this shifts the low frequency atmospheric noise up to the modulation frequency, so that the noise floor at low frequencies is due to the detector white noise (see Fig 3.9). Finally, this stream can be low-passed to recover the demodulated data, which is of the form

$$d_d^{lp}(t) = \frac{1}{2}Q(t) + \frac{i}{2}U(t) + \bar{T}_w$$

where $\bar{T}_w$ is the white noise floor and has both a real and imaginary component. An example of a demodulated timestream is shown in Figure 3.10.

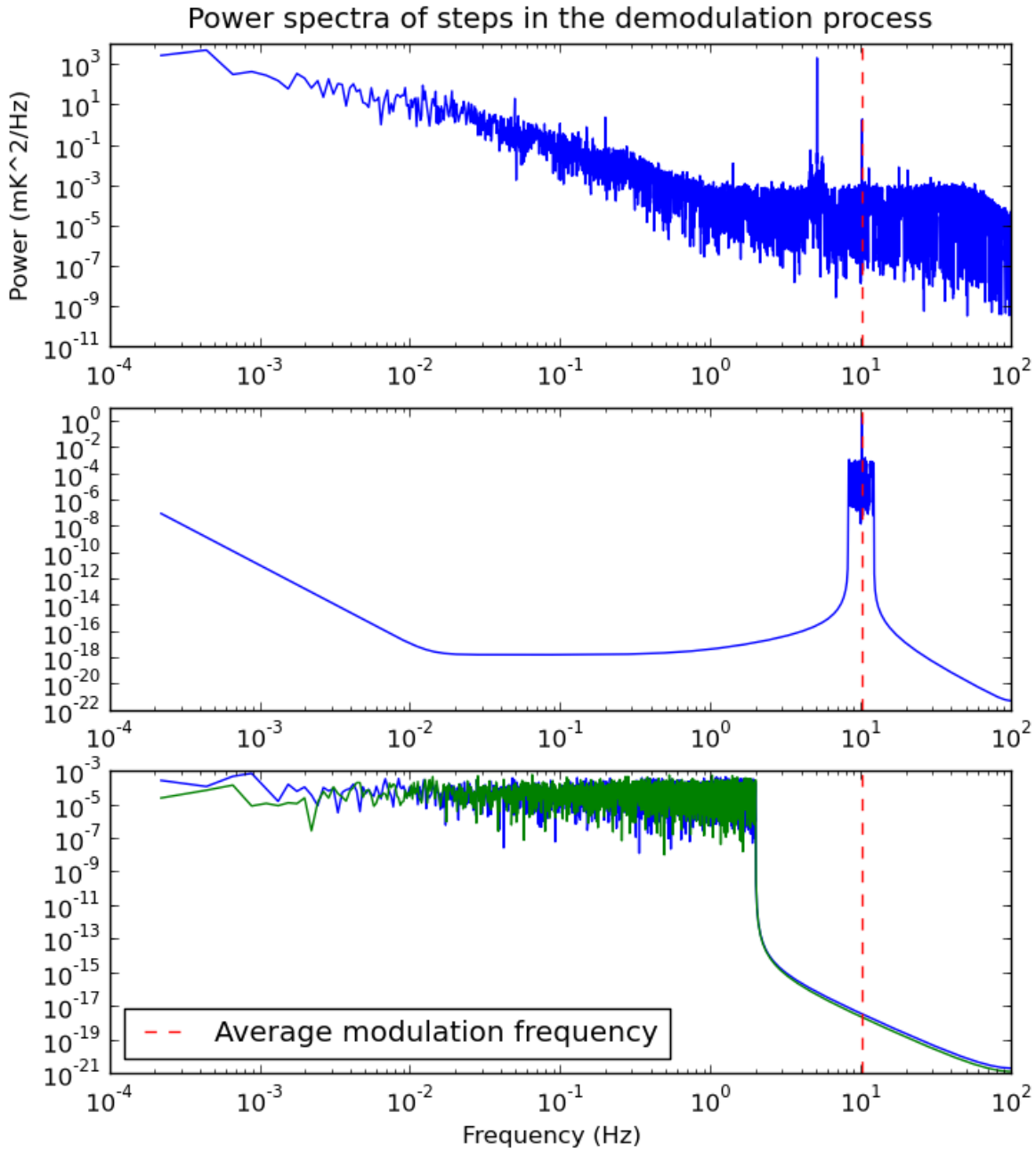

Figure 3.9: Power spectra of each step of the demodulation process. The $y-$axes all have the same units. The top plot shows the raw timestream power spectrum, with the $4f$ modulation frequency highlighted by the red dashed line. The second plot shows the band-passed data, with band-width 4 Hz. This width is large enough to ensure that the Q and U signals are not modified by the filter, and narrow enough to exclude the 3^{rd} and 5^{th} harmonics. The final plot shows the spectra of the real (Q) and imaginary (U) components of the demodulated and subsequently low-passed data.

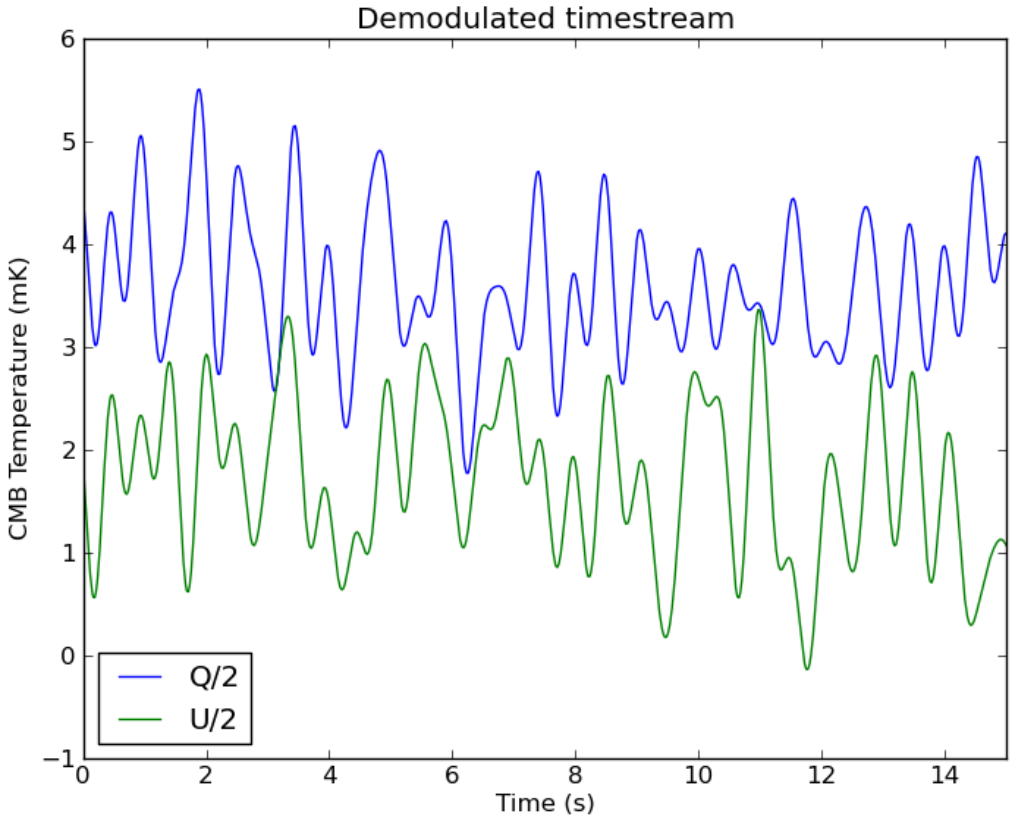

Figure 3.10: Demodulated Q abd U timestreams.

3.4 Optical Efficiencies

The optical efficiency of each TES is determined by measuring targets with known temperatures and comparing the expected to measured responses of each detector. The targets used for ABS include Jupiter and Venus, and so-called 'sky dips,' measurements of the variation in atmospheric brightness while scanning in elevation. The latter method takes advantage of the variation of the loading as a function of elevation angle (Sec. 3.2). The temperatures of the planets are known to high accuracy, however due to their small size not all detectors can scan across the planet at once. On the other hand, the sky dips calibrate all detectors at once, but the Rayleigh-Jeans temperature of the atmosphere, which is dependent on PWV, is not as accurately known, and can vary across the array and over the timestream of the sky dip due to

turbulence (Sec. 3.2.1). Combining the advantages of these two types of targets, we use sky dips to get the relative optical efficiencies of all the detectors, and measure the absolute efficiencies of a few select detectors for over all scaling.

3.4.1 Relative Optical Efficiencies from Sky Dips

Determining the relative efficiencies from sky dips involves 3 steps. In the first step, the peak to peak amplitude in pW, called the response $R_{\rm meas}$, is determined for each detector. The detector responses depend on both elevation angle and atmospheric brightness, in addition to the efficiencies. The next two steps seek to divide out the dependence of the first two factors and isolate the relative efficiencies. Since the temperature of the atmosphere, correlated with PWV, is not very accurately known, we calculate the expected response, $R_{\rm 10K}(\theta_{el})$, using Eq. 3.6 assuming a 10 K sky at zenith and a bandwidth of 30 GHz. The elevation angles were derived from a combination of the boresight pointing model and the detector offsets from the boresight by Srinivasan Raghunathan.

The top of the array (Fig. 2.7), which looks lower on the sky than the boresight, has a larger expected response than the bottom. The second step involves taking the ratio for detector i,

$$\epsilon_{\rm 10K,i} = \frac{R_{\rm meas,i}(\theta_{el})}{R_{\rm 10K,i}(\theta_{el})}, \tag{3.8}$$

which should be independent of elevation. We don't know the PWV accurately, but for this calculation we assume that it is the same for all detectors at any given time, and so the ratios $\epsilon_{\rm 10K,i}/\epsilon_{\rm 10K,j}$ do not depend on PWV. We define a reference efficiency $\epsilon_{\rm ref}$ for each sky dip as the average of the efficiencies of the most stable detectors over the season. Details of the reference set follow. The reference efficiency should have the same PWV dependence as each individual detector, and so the final step is to

obtain the relative efficiencies

$$\epsilon_{\mathrm{rel,i}} = \frac{\epsilon_{\mathrm{10K,i}}}{\epsilon_{\mathrm{ref}}}. \tag{3.9}$$

Figure 3.11 shows an example of a typical sky dip timestream. Their peak to peak amplitude in elevation is 5°, and the period is $\sim$ 24 seconds (corresponding to $\sim$ 0.04 Hz). The duration is $\sim$ 2.5 minutes, completing between 6 and 7 full periods. The boresight central elevation angle for each sky dip ranges from 45° to 85°. The expected responses for a 10 K sky assuming 100% transmission vary from 0.4 pW at the highest elevation offset to 1.2 pW at the lowest.

To determine the detector response, the atmospheric temperature model (Eq. 3.6) is calculated the elevation timestream and is linearly fit to the detector timestream. The model takes the form

$$W_{\mathrm{exp}} = 2kT_{\mathrm{RJ}}(\theta_{el}(t))\Delta f, \tag{3.10}$$

$$T_{\mathrm{RJ}}(\theta_{\mathrm{el}}) = T_{\mathrm{atm}}(1 - e^{-\tau \sec(90^\circ - \theta_{el})}), \tag{3.11}$$

where T_{atm} and optical depth τ are chosen to be 250 K and 0.04, respectively, so that $T_{\mathrm{RJ}}(\mathrm{zenith}) = 10$ K at central frequency 145 GHz. The first order coefficient of the fit represents the efficiency, and when multiplied by the peak to peak amplitude of the model yields the measured power (Fig 3.11). The first three periods of each sky dip timestream are discarded in the fit to allow for the temperature of the focal plane to equilibrate. If there were more 'dips' per sky dip file, this would be equivalent to measuring the power in the 0.04 Hz peak of the power spectrum. To assess the goodness of the fit, the figure of merit is defined as the root mean squared of the difference between the data and the fitted model. The figure of merit has units of power, and typical values are $\sim 1.5 \times 10^{-14}$ W. In this case a lower value implies a better fit. The figure of merit for the pictured sky dip in Figure 3.11 is 1.4×10^{-14}

W. The top left plots in Figures 3.12 and 3.13 show the responses $R_{\rm meas}$ and the efficiencies $\epsilon_{\rm 10K}$, respectively, of all detectors over the entire season.

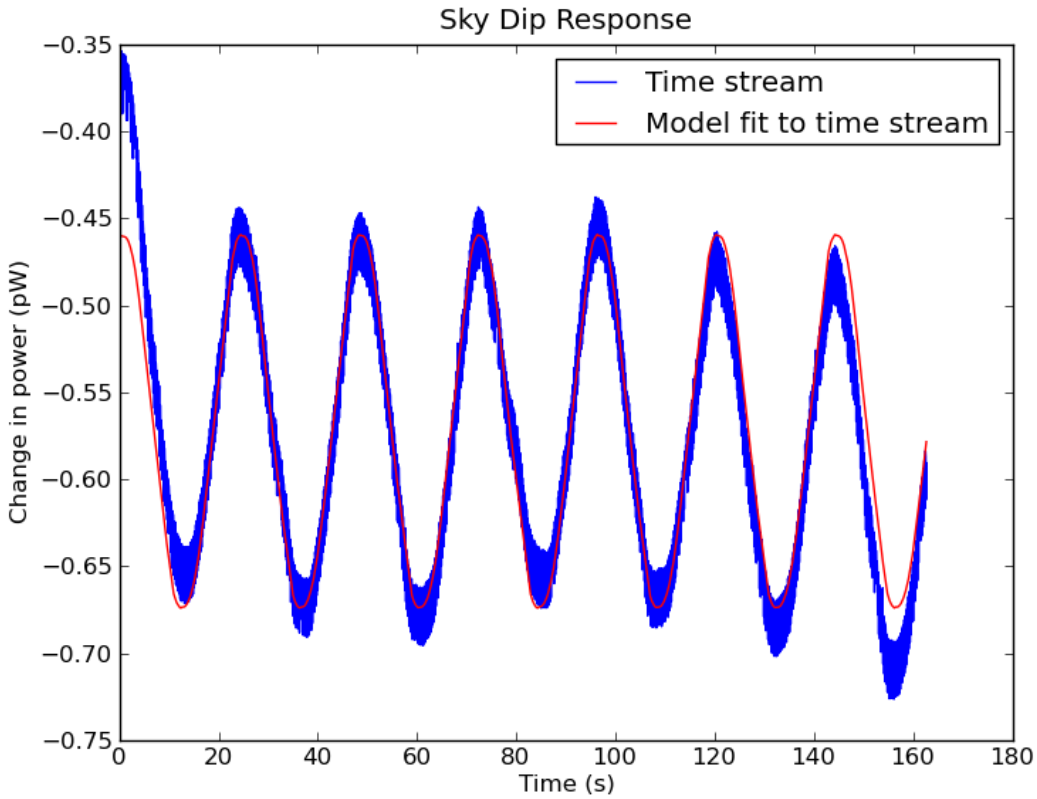

Figure 3.11: Example of a detector's response to a sky dip. The timestream is shown in blue, and the model discarding the first three periods ($\sim$ 75 s) in red. The half-wave plate was spinning when these data were taken. This causes oscillations which are too high frequency to be distinguished here, but which appear as a thickening of the timestream. There is little atmospheric drift during this sky dip, and fitting for it gives $< 0.5\%$ correction to the linear fit. The figure of merit (see text) is 1.4×10^{-14} W, significantly lower than the cut-off at 3.0×10^{-14} W.

Due to fabrication differences between the top and bottom halves of the detectors, the two groups are compared to different references, $\epsilon_{\rm ref,top}$ and $\epsilon_{\rm ref,bottom}$, and are scaled to their absolute efficiencies separately. The groups are clearly visible in the figures: detectors 81-320 are in the bottom, and 1-80 and 321-480 are in the top. The bottom detectors have a lower response despite seeing a hotter sky due to their shifted band, in part because they are looking higher in the sky. The efficiencies shown in

Figure 3.13 account for the different elevations, and the detectors in the bottom half can be seen to have a higher variance in efficiencies than the top half, discussed in more detail below.

Obtaining $\epsilon_{\mathrm{ref,top}}$ and $\epsilon_{\mathrm{ref,bottom}}$ involved two iterations of cuts on sky dip files and detectors. There were 636 sky dips taken during the first season. Of those, the ones taken when the PWV was above 3 mm were excluded from the analysis to ensure that the loading on the detectors was not too high. Those taken when central boresight elevation was above 65° were also excluded because the amplitude of the signal from the sky dips at higher elevations is too small to be reliable. There were 336 sky dips within these cuts. In addition, sky dips during which a large number of detectors were not biased properly were also cut, as were those with a figure of merit greater than 2.0×10^{-14} W. In the first iteration, 206 sky dips remained.

The first iterations of $\epsilon_{\mathrm{ref,top}}$ and $\epsilon_{\mathrm{ref,bottom}}$ are obtained by averaging the responses of the most stable detectors in their respective groups. They are defined as detectors such that $min(\epsilon_{\mathrm{10K,bottom}}) > 0.1\%$, $min(\epsilon_{\mathrm{10K,top}}) > 1\%$, and $10\% < median(\epsilon_{\mathrm{10K,all}}) < 100\%$. Figures 3.12 and 3.13 show the detector responses and efficiencies, respectively, of the 3 steps in the selection process to obtain the reference efficiencies. The latter also shows the reference efficiencies over time of the two halves of the focal plane.

The second iteration of cuts involves looking at the relative efficiencies of each detector, obtained using Eq. 3.9. The results are shown in Figure 3.14. At this stage the elevation and PWV dependence has been divided out, and so the variations visible in each detector trace, represented as horizontal lines, are the uncertainties in the detector efficiencies. The final cut was made on sky dips during which one or more detectors had unusually low (5%) relative efficiency, leaving 154 sky dips in the final analysis.

Before calculating the relative efficiencies ϵ_{rel}, the reference efficiencies are explored in more details. As expected, there is a strong correlation between the reference

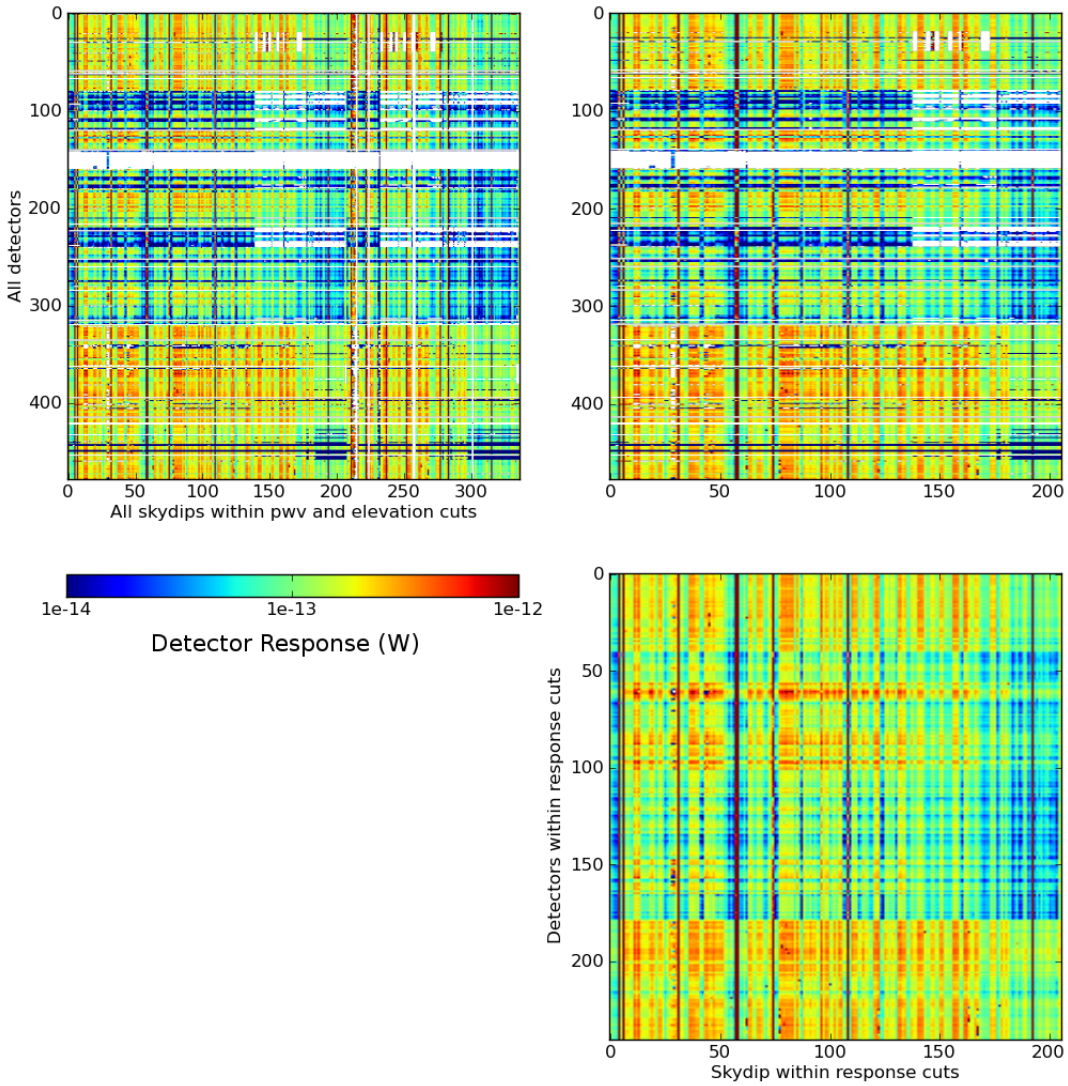

Figure 3.12: Detector responses over the 3 cut steps to determine the reference. The y-axes enumerate the detectors, and the x-axes enumerate the sky dip files in chronological order. Top left includes all detectors, and all sky dips taken when PWV < 3.0 mm and central boresight elevation $< 65°$. Detectors which were not working or which unlocked appear as white and black, respectively. The top and bottom batches are clearly visible: detectors 81-320 are bottom, and 1-80 and 321-480 are top. Going to the top right plot, the y-axis is the same, but only sky dips with a low figure of merit and those with enough working detectors are included. There are 206 such sky dips. The final plot includes the same sky dip files, but only the detectors that were stable over all sky dips are displayed. There are 241 stable detectors, 103 from the top and 138 from the bottom.

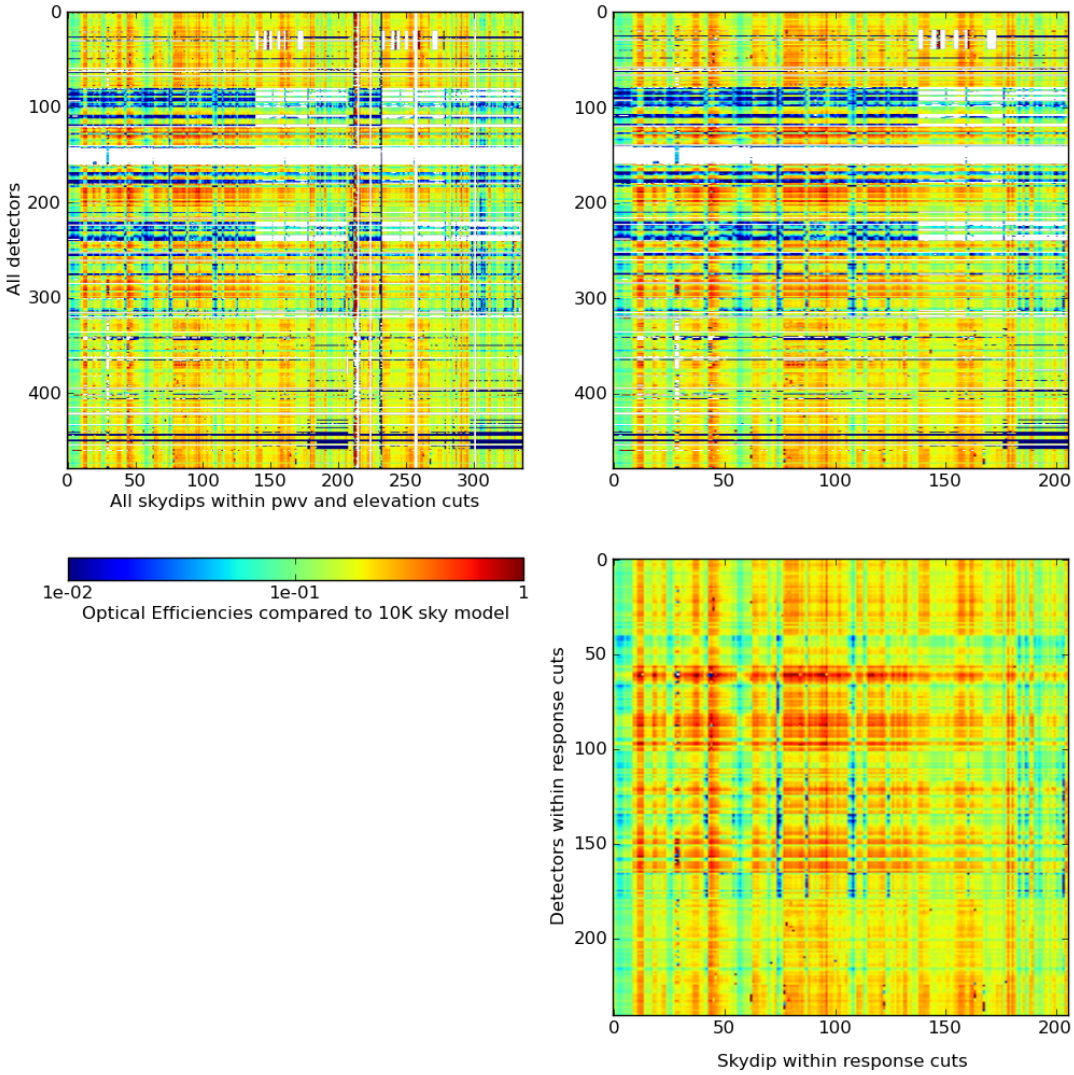

Figure 3.13: Detector efficiencies ϵ_{10K} using a 10 K sky model, over the same 3 cut steps as Fig. 3.12. The variation in the efficiencies over the sky dips is primarily due to variations in PWV.

efficiencies and PWV (Fig 3.15a). Further, the bottom half has a stronger dependence on PWV due to its shifted band pass, as anticipated in Figure 3.3. In addition to a PWV dependence there is also a dependence of efficiency on the azimuth position of the telescope, as shown in Figure 3.15b. On the y-axis are the reference efficiencies corrected for their PWV dependence by dividing by the best fit linear model shown

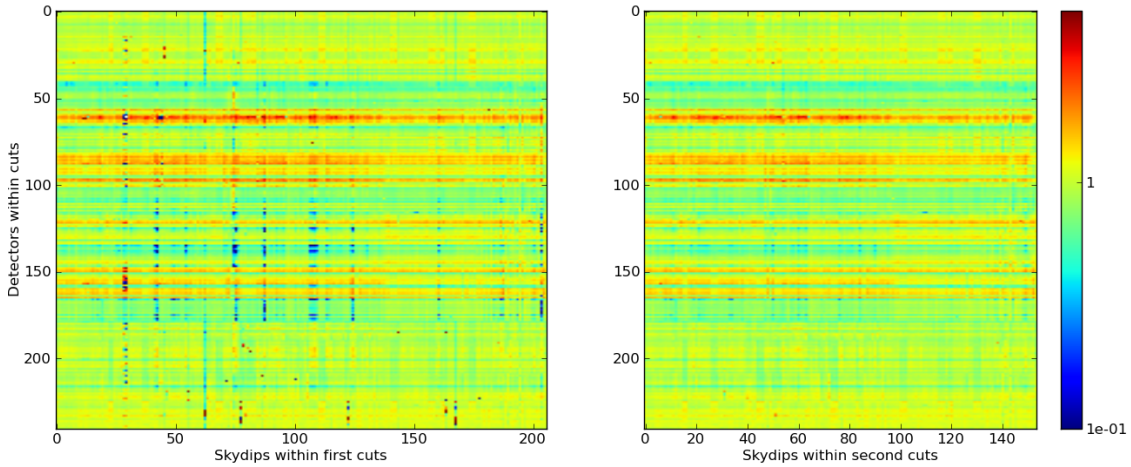

Figure 3.14: Relative optical efficiencies $\epsilon_{\rm rel}$ for the 241 detectors within the response cuts. The dependence on average PWV is divided out when top and bottom halves are compared to their respective references. The plot on the left shows all 206 sky dips, and on the right the sky dips with anomalies, visible as vertical lines, are removed, leaving 154 sky dips. Each horizontal line represents a detector's relative efficiency $\epsilon_{\rm rel}$ over time. The detectors are grouped by column, and detectors in the same column are physically close to each other and observe adjacent patches of sky. The fact that the vertical striations still visible in the right plot seem to be correlated in groups, *i.e.* 200-220 follow a similar pattern and 221-241 follow a different pattern, suggests that the variance is due to variations of PWV across the focal plane during a single sky dip.

in Figure 3.15a. The azimuth dependence could be in part due to different ground pick up, for example from the Cerro Toco peak or the ACT ground screen.

To determine if there were any changes in the efficiencies over the course of the season, we look at the reference efficiencies after being corrected for both PWV and azimuth position dependence, over time (Fig. 3.16). Although the scatter is significant, 17% for the top half and 23% for the bottom, the Figure 3.16b in particular reveals that the efficiencies measured in the three time periods outlined in Table 3.4 follow different statistics. Changes in focal plane servo temperature were found to coincide with these changes in efficiency statistics (Fig. 3.17). Field tests are currently planned to further investigate this dependency by taking sky dip data while varying the focal plane servo temperature.

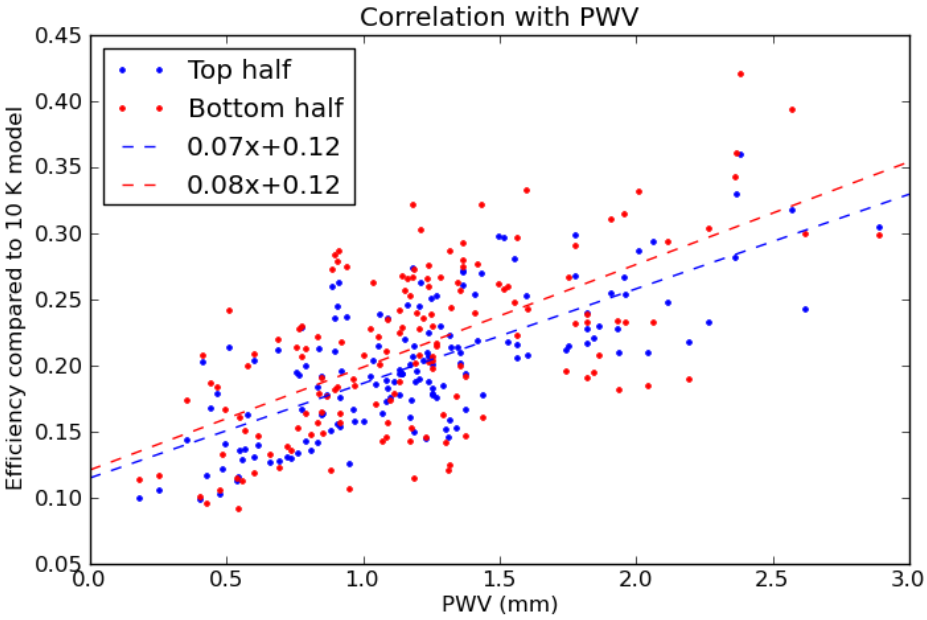

a.

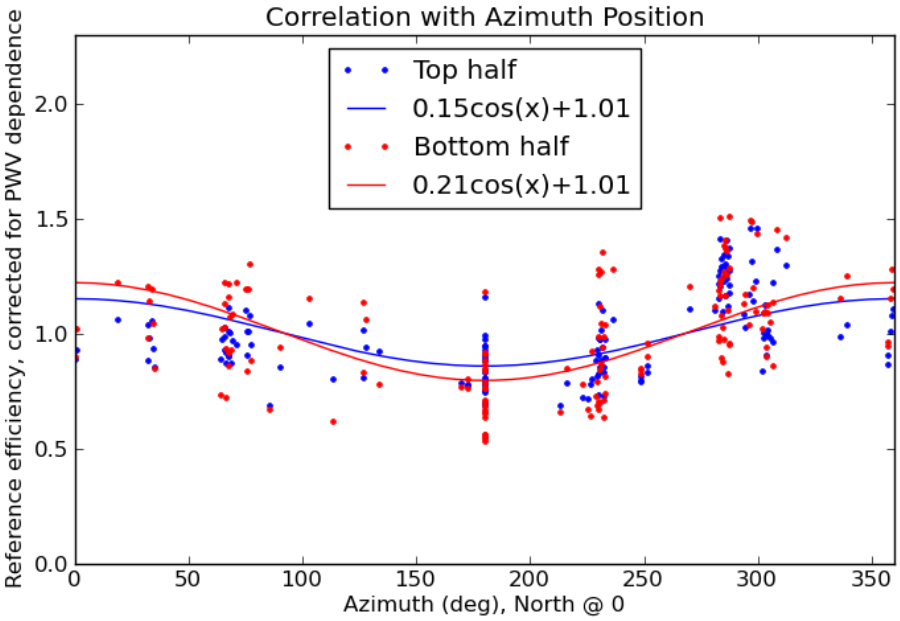

b.

Figure 3.15: Top: correlation between reference efficiency $\epsilon_{\rm ref}$ and PWV. As expected, higher PWV leads to higher response in detectors, and when compared to the same 10 K sky, they appear to have higher efficiency. The bottom half shown in red, which sees more of the 183 GHz water line, has a stronger dependence on PWV. Bottom: Correlation between reference efficiencies and azimuth position. The reference efficiencies are corrected for their PWV dependence by dividing out the best fit line in *a*.

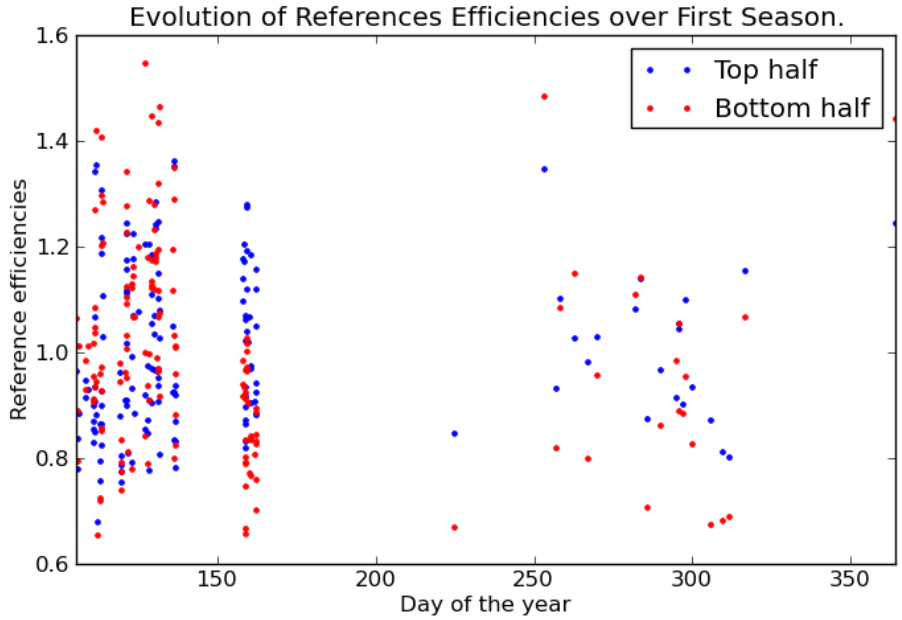

a.

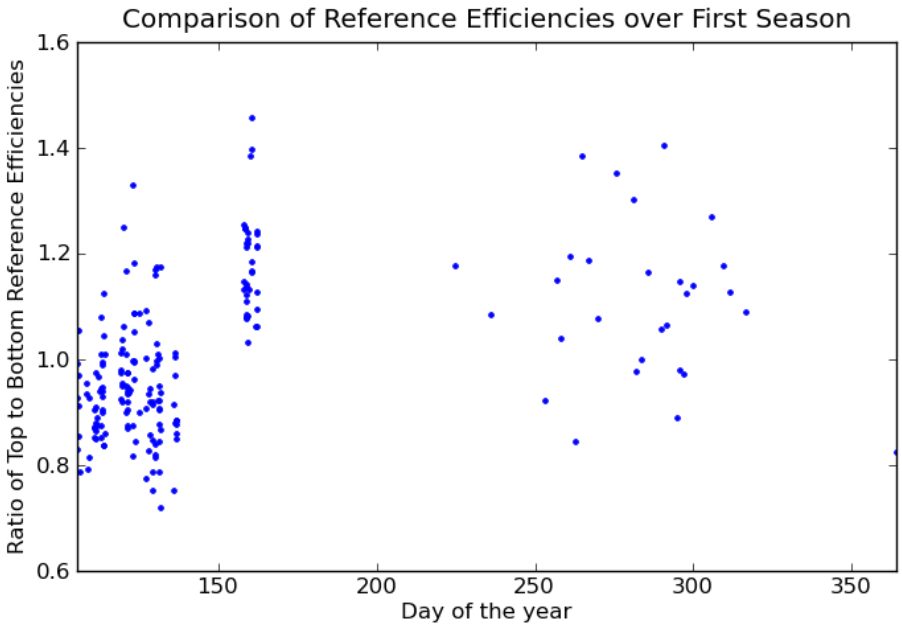

b.

Figure 3.16: a. Reference efficiencies, with dependence on PWV and azimuth position divided out, of top and bottom halves during first season. Days 136 - 158 (March 15 - June 6) ABS was not observing due to long term maintenance. Days 162 - 225 (June 10 - August 12) ABS was running but no sky dips were taken. b. Three different efficiency statistics are clearly visible.

The relative efficiencies of each detector were obtained from their traces over the 154 final sky dips in two steps, mainly to assure that detectors with good efficiencies

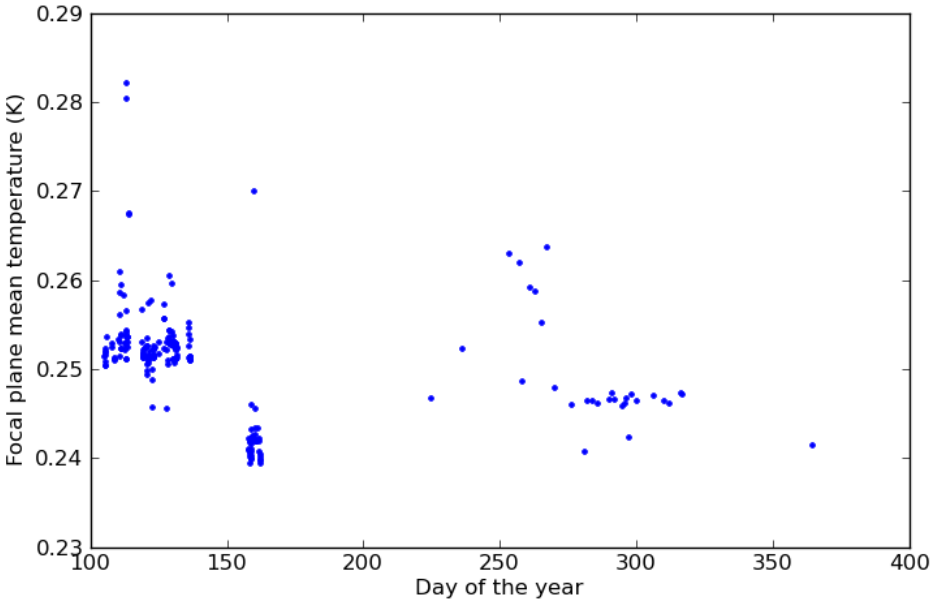

Figure 3.17: Focal plane mean temperature during sky dip data acquisition. The high temperature outliers indicate that the temperature broke through the servo during the sky dips.

but which did not work for more than half of the sky dips were assigned accurate values of efficiency. The final values are shown in Figure 3.18 as a histogram and by detector number. The overall scaling of the values is arbitrary, as is the relative scaling of the top to the bottom detectors. They are each set so that their respective reference is 1. As is visible in the second plot, the 'top' detectors (0-88 and 352-528)

	Period I April 14 - May 15	Period II June 6 - June 10	Period III August 11 - December 29
$\epsilon^*_{\rm ref}$(top half)	0.99 ± 0.16	1.03 ± 0.13	1.01 ± 0.13
$\epsilon^*_{\rm ref}$(bottom half)	1.06 ± 0.18	0.86 ± 0.10	0.95 ± 0.22

Table 3.4: Mean reference efficiencies for each of the three periods of sky dips; the star indicates that the PWV and azimuth dependence has been divided out. Although the scatter in the top half within each period is only slightly better than the bottom half, the mean stays stable over the first season to within a few percent, whereas the bottom half varies by around 20%.

have much tighter distribution of efficiencies, and the bottom detectors are much more scattered.

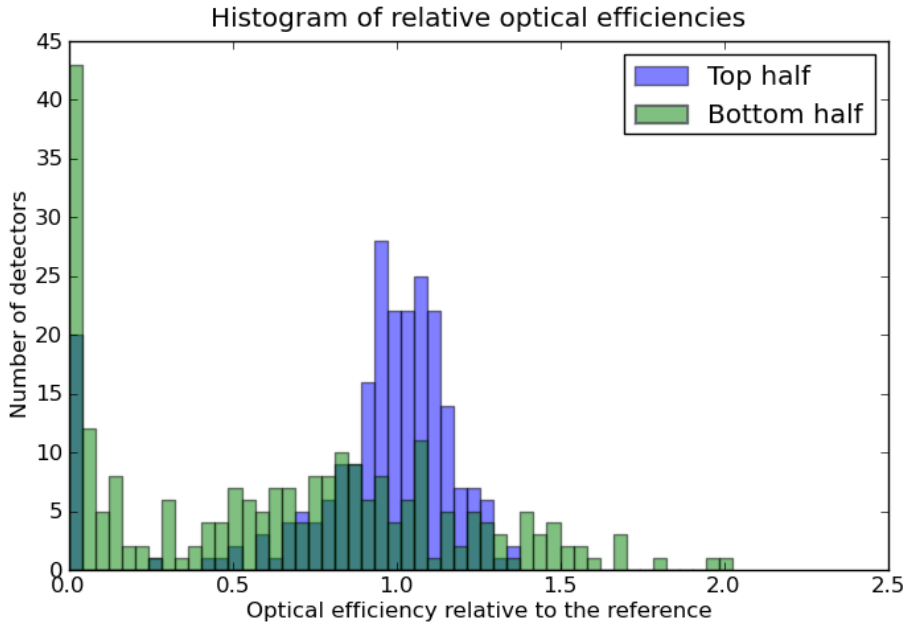

a.

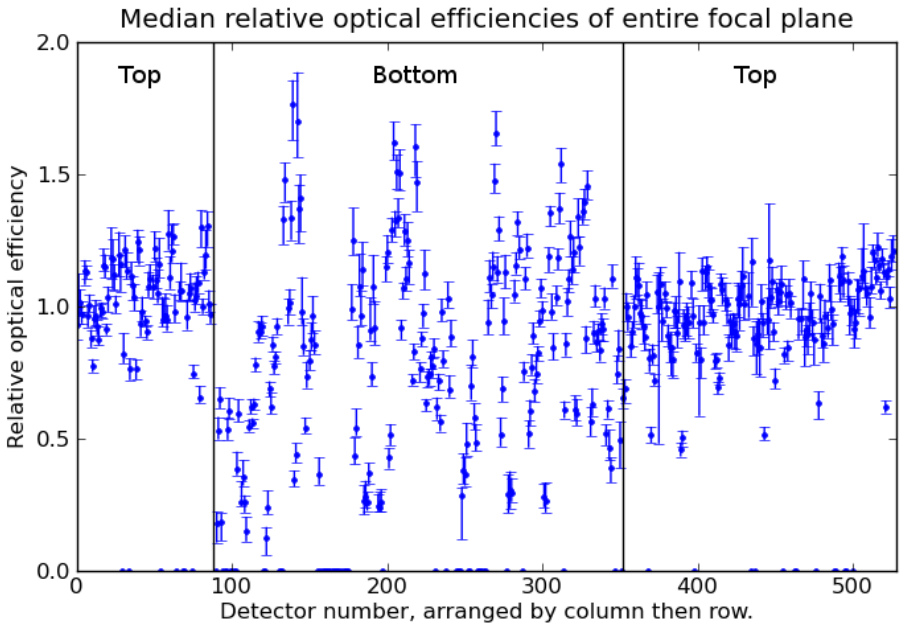

b.

Figure 3.18: Detector optical efficiencies as determined by sky dips. The values at zero represent TESes which were working for fewer than 10 sky dips throughout the season. The distribution of the top half has a clear gap between working and non-working detectors, whereas the bottom half has a family of detectors with low but non-zero efficiencies. A cut-off of 0.2 was imposed on relative optical efficiency, and non-working or low-efficiency detectors are discarded in all subsequent analysis.

3.4.2 Comparison of Sky Dips with other measurements.

Relative optical efficiencies were also calculated using an entirely different method, by measuring the detector response to a coarsely spaced (1") wire grid polarizer placed at the top of the baffle. The slightly polarized signal produced by the coarse grid, after being modulated by the spinning half-wave plate, produced a response in the detectors modulated at $4f$. Similarly to the sky dips, the absolute response due to the wire grid was not known accurately, but it was assumed to be the same for all detectors within each of the top and bottom halves to extract the relative efficiencies.

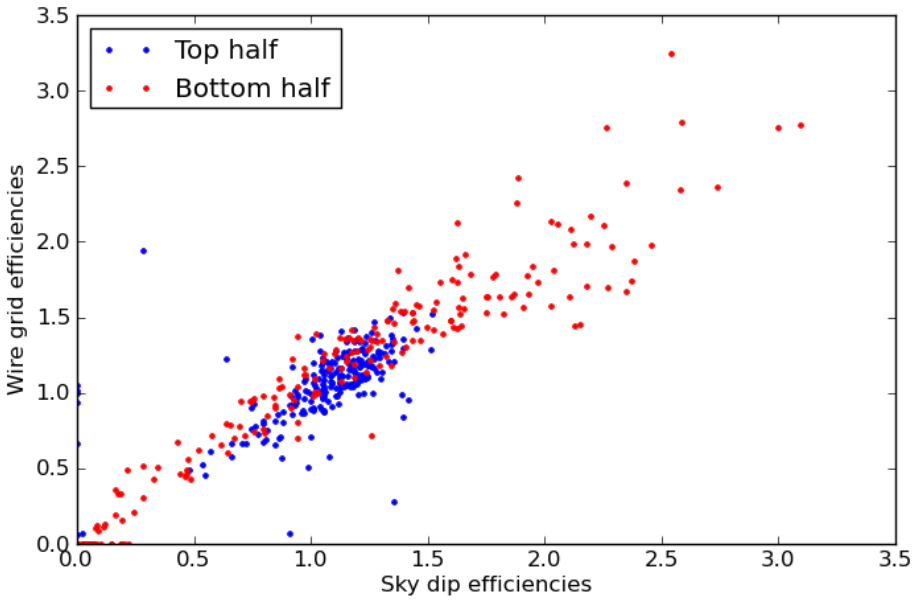

Figure 3.19: Comparison of relative optical efficiencies calculated from sky dips and from wire grid measurements. The top and bottom halves are separately normalized to have a mean of 1. The agreement of the measurements considering only the detectors with relative efficiencies higher than 0.2 is within 16% for the top half and within 15% for the bottom.

The comparison of the sky dip efficiencies and the wire grid efficiencies is shown in Figure 3.19. Agreement between the numbers is determined by the linearity of the data. The overall scaling factor is arbitray, and the top and bottom halves are separately normalized to have a mean of one. The agreement of the measurements

for detectors with relative efficiency higher than 0.2 is within 16% for the top half and within 15% for the bottom.

Chapter 4

Data Processing

Analyzing the data obtained from the telescope to produce maps is a considerable task. This chapter describes the steps from raw ABS data to preliminary maps of the primary CMB patch, Field A, for a subset of the 2012 season of observation, during which ABS operation was stable. We focus on a roughly one month reference period, days 284 - 312 of the year corresponding to October 11 - November 7 (Tab. 3.1 and Fig. 3.5) which includes a total of 236 hours of observation prior to data selection of the 2940 $\deg^2$ Field A (Fig 4.1).

The first step of the data analysis is to select the fraction of the data that can be used for map making, discarding defective data and identifying pathological behavior of individual detectors. The design of algorithms to perform these cuts requires an understanding of the data properties and all possible defects. Section 4.1 describes the first iteration of data selection algorithms, developed by Akito Kusaka, and how they affect the sensitivity of the focal plane. The selection criteria are conservative, cutting the observation time down to 135 hours. We also discuss possible improvements for future iterations. Section 4.2 shows estimates of the current and projected sensitivity of ABS in multipole ℓ space. Finally, Section 4.3 shows the preliminary polarization maps made using the current set of data selection criteria.

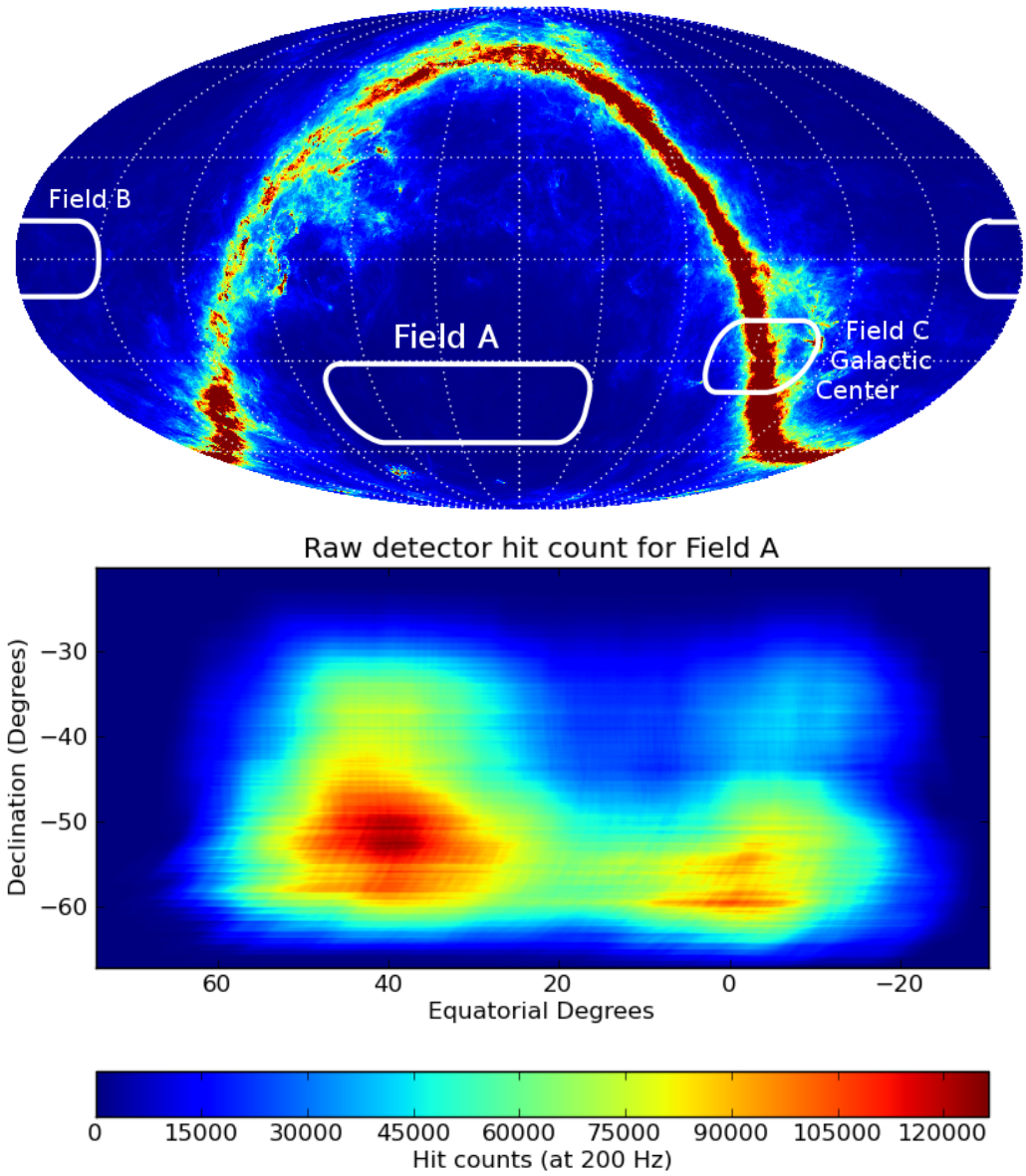

Figure 4.1: Top: The three ABS observation fields shown in equatorial coordinates, overplotted with our galaxy for reference. The primary observation field is Field A, chosen for its low level of contamination from galactic dust emission. Field D, located at the same right ascension as Field B at a declination of $-40°$, is the lowest priority field and is not shown here. Bottom: Detector hit count map for Field A during the reference period, including the cuts outlined in Section 4.1. The hitcount represents the number of samples over all detectors observing a particular pixel, where the pixel size is $5'$ and the data acquisition rate is 200 Hz. The total area of the field is 2940 deg^2. Its shape is distorted due to the projection from spherical coordinates onto the plane, appearing slightly bigger than it is on the sky. More observations are needed to fill in the field.

4.1 Data Selection

The first step of data selection is detector selection, in which faulty detectors are cut for the entire period of interest. This class of detectors includes those with faulty readout circuits, those with working readout circuits but which are not optically coupled to the sky, and those which are otherwise working fine but have low optical efficiency. The first group is identified by a flat output, and the other two by doing optical tests such as sky dips (Fig. 3.18) and sensitivity to HWP modulation (Sec. 3.3) and wire grid polarization (Sec. 3.4.2). Of the 480 live detectors in the ABS focal plane, 401 pass these cuts, or about 83%.

Cuts on timestreams fall in three categories. The first cut is on full constant elevation scans (CESes), the second is on individual detector timestreams within a CES, and the third is on portions of detector timestreams. The first type of cut determines the overall observation time, and the other two determine the effective number of detectors, D_{eff}, defined as the sum of the fraction of time that each detector passed the data selection. The upper bound from detector cuts only is D_{eff}=401, and timestream cuts will further decrease this number.

4.1.1 Masking glitches

The first cut we apply is to mask portions of detector timestreams. Data timestreams which are otherwise perfectly healthy sometimes have 'glitches' which need to be masked. Glitches are spikes in the data ranging in length from a single sample to ~ 10 samples, or 0.05 s. Effective glitch identification over the HWP signal, detector noise, and atmospheric drift, and efficient masking, are key elements in the data filtering process. Three types of glitches have been identified. The first is a single sample glitch, the second is a 2 sample glitch with a ring of ~ 4 more samples, and the third is a sharp increase in signal with a ~ 10 sample decay. Because of the decay

time, the last type of glitch is attributed to a physical spike in power on the TES island, likely due to cosmic rays hitting it directly. The first two are attributed to electrical glitches in the readout circuit, mainly because of their unphysically short duration of ~ 10 ms.

The current glitch finding program identifies glitches by first subtracting the HWP shape ($A(\phi)$) from the timestream in the same way as the first step of the demodulation process (Sec. 3.3), and then by splitting the ~ 1 hour timestream into less than one second sections to minimize the atmospheric drift. After these steps the dominant variation in signal is due to detector noise. Within each section the data are averaged in two ways, each targeting a characteristic glitch size. For identifying the 1 and 2 sample glitches, the data in each eighth second (25 sample) section are averaged for every adjacent pair and compared to the average of all data within that section. For the 10 sample glitches, the data in each quarter second (50 sample) section are averaged for every set of 10 adjacent samples and compared to the average of all data within that section. A sample is flagged as a short or long glitch if its pairwise or 10-sample average, respectively, deviates by more than 10σ from the section baseline. In addition to all the flagged samples, the glitch mask masks an additional 10 samples at the beginning and end of each short glitch and 20 samples at the beginning and end of each long glitch. The glitches are masked prior to all other data analysis.

Jumps in the data are also flagged by the glitch finder. Jumps differ from glitches in that the DC level of the data before and after a glitch is the same, whereas for a jump it is different, with the level shift sometimes up to several orders of magnitude greater than the HWP signal. Although the glitch finder flags the jump and masks a section of the timestream before and after, it does not reset the DC level, and so effectively the jump is still there. The jump finding algorithm is currently in development and so there is no cut criterion related directly to jumps yet. However,

indirectly they affect some of the other criteria discussed below, and most if not all timestreams featuring jumps are cut by at least one of the others.

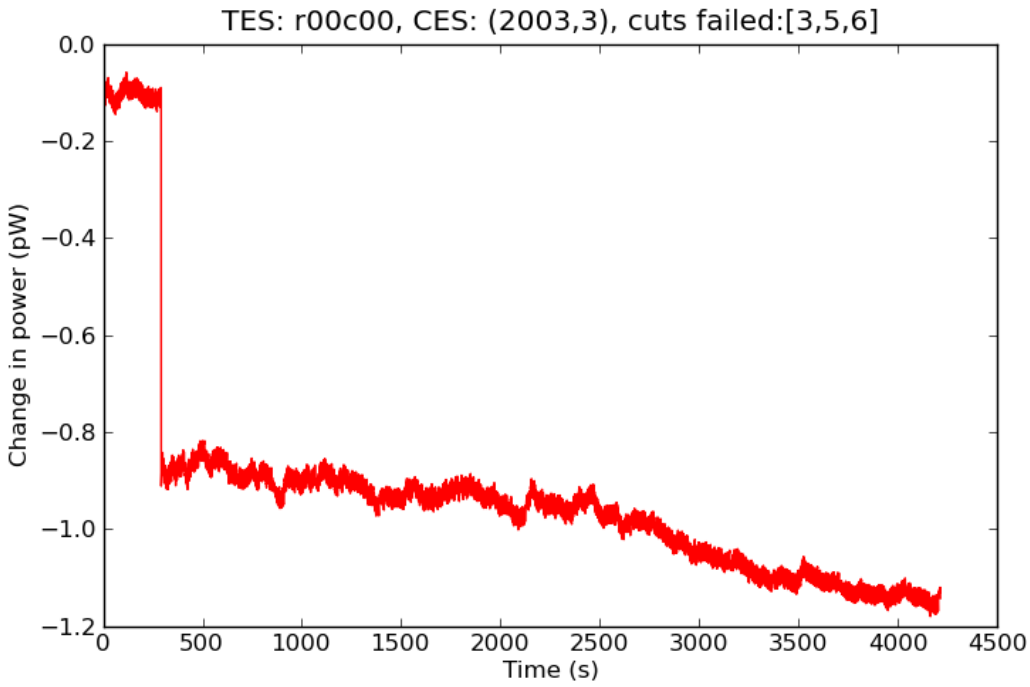

Figure 4.2: An example of a jump in the raw timestream. The values of raw stationarity, kurtosis and skewness for this timestream are 2.66, 21,000, and 83, respectively, well above the cutoffs listed in Table 4.1.

4.1.2 Full Timestream Cuts

Cuts on the individual detector timestreams are done by looking at the statistical properties of both the raw and demodulated glitch-masked data. The full set of the criteria described in this section is listed in Table 4.1 along with the current cutoff limits. We expect the detector noise to be white; however, in the raw timestream the HWP signal and atmospheric drift dominate over the detector noise statistics on short and long timescales, respectively. To isolate the detector noise, first the glitch mask is applied, then the HWP shape $A(\phi)$ is removed, and then the DC offset is subtracted from each 50 sample interval, eliminating all features below 4 Hz

including the atmosphere. The stationarity is determined by calculating the rms of the data for each 50 second interval and comparing to the average over all 50 second intervals. It is a dimensionless quantity with zero signifying perfect agreement among all intervals of that timestream. The skewness and kurtosis are calculated for the full CES timestream at once.

In addition to noise properties, there are two more criteria imposed on the raw timestream. The first is related to the HWP signal. A reference HWP DC shape is calculated for each detector by averaging the HWP structure obtained from timestreams taken at all times during the 236 hour reference period when the PWV was 1 mm, and the shape of each timestream is compared to the reference by taking the average of the ratio. The second is related to the glitches - timestreams which have an excessive number of glitches are cut entirely.

A jump in the timestream manifests itself as a large non-stationarity parameter and, depending on its location within the 50 second interval, as large skewness and kurtosis. To see this consider the case where the jump is close to the middle of the interval. Subtracting the mean offset would place roughly an equal number of samples at the same level above and below zero, preserving the symmetry of the data and not affecting the skewness. However these points far above and below the rest of the distribution would lengthen its tails and increase the kurtosis into the tens of thousands. Conversely, if the jump is near the edge of an interval, subtracting the mean would place most of the samples very close to zero and not affect the kurtosis as much, but the few samples which are displaced are all in the same direction, and would increase the skewness into the hundreds. Figure 4.2 shows an example of a jump in the timestream, with a stationarity of 2.66, kurtosis of 21,000, a skewness of 83. Generally, the data jump to the new DC level over the course of 2 samples, and so even if the jump happens to land on the boundary between two intervals, it will affect the DC offset removal of both intervals and still be flagged.

The cuts on the raw timestream based on non-stationarity, skewness, kurtosis and HWP shape are very loose: $[0, 0.60]$, $[-3, 3]$, $[0, 1000]$, and $[0.1, 3]$, respectively. They are meant to identify only severely flawed timestreams, in particular ones with jumps, before they get demodulated. This is important because the band-passing step of the demodulation process does not filter out the in-band signal introduced by the jump. It does, however, filter out the high frequency ringing, wiping out all non-Gaussianities in the noise. Thus even a timestream with a jump or unmasked glitch will still appear Gaussian when demodulated, and testing for Gaussianity is not a sufficient selection criteria.

The criteria used to identify pathological data in the demodulated timestream are the white noise amplitude and the $1/f$ knee frequency (Sec. 3.3), and a χ^2 fit of the power spectrum to a simple white-noise-plus-$1/f$ model, $P(f) = A^2(1 + (f/f_{knee})^k)$. The parameters A, f_{knee} and k are determined, and the (reduced) χ^2 is the goodness of fit. It is calculated separately for frequencies above and below 1 Hz, and in the latter case the scan frequency and its harmonics are removed prior to the fit.

4.1.3 Constant Elevation Scan Criteria

Once the flagged timestreams are removed, the final cut is on entire CESes. Those with fewer than 150 working detectors are cut, as well as those whose duration is less than 1000 seconds, or about 17 minutes. The latter only cuts 2 hours from the reference period observation time, reducing it to 234 hours, whereas the former reduces it to 135 hours. Although this threshold cuts the observation time almost in half, it only cuts about 10% of the data by time. In practice, the cut on CES duration is done first and short CESes are not processed at all, hence this cut is defined as cut number 0 in Table 4.1.

Cut number	Cut definition
0	CES duration $>$ 1000 s
1	HWP shape ratio to reference $\geq$ 0.1
2	HWP shape ratio to reference $\leq$ 3.0
3	Raw stationarity $\leq$ 0.6
4	Raw skewness ≥ -3
5	Raw skewness $\leq$ 3
6	Raw kurtosis $\leq$ 1000
7	No. 2 sample glitches $\leq$ 100
8	No. 10 sample glitches $\leq$ 200
9	Demodulated white noise amplitude $\geq$ 5 aW$\sqrt{s}$
10	Demodulated white noise amplitude $\leq$ 100 aW$\sqrt{s}$
11	Demodulated χ^2 above 1 Hz $\leq$ 3
12	Demodulated χ^2 below 1 Hz $\leq$ 5
13	Demodulated knee frequency $\leq$ 0.04 Hz

Table 4.1: List of the first iteration of data selection criteria for the reference period October 11 - November 7. The numbers in the left column are used throughout this chapter to refer to particular cuts.

4.1.4 Selection Statistics

This first iteration of cuts was determined by looking at the array-wide statistics for each criterion and cutting the tails of the distributions by eye (Fig. 4.3). The purpose of this pass is twofold. It is meant to test the accuracy of the algorithms in flagging the intended defects and to provide a baseline on which to improve with further iterations. In this section the baseline is determined, and the cuts which result in the greatest decrease in effective detector number D_{eff} are identified.

Figure 4.4 shows the time efficiency for each criterion separately for every detector in the focal plane. Time efficiency is defined relative to the 401 detectors within the detector cuts, and the remaining 127 squares, representing the 79 defective detectors and the 48 dark channels, are displayed in black in the top left plot. Defined in this way, the time efficiency is related to D_{eff} by a factor of 401. Imposing all of the criteria yields a time efficiency of 42.3%, or $D_{eff} = 170$. The criteria which reduce D_{eff} the most are the cutoffs on raw kurtosis and number of glitches, cut numbers

6, 7, and 8 in Table 4.1. The detectors in high numbered rows and columns feature a large number of glitches for reasons not fully understood yet.

Array Sensitivity

The effective detector number D_{eff} is a measure of how sensitive the focal plane is, given that all detectors are equally sensitive. In fact for ABS this is not the case, and so a more consistent measure needs to be considered. In order to define detector sensitivity, we first introduce the noise equivalent power (NEP) of a detector, defined as the signal power that gives a signal-to-noise ratio of one in a 1 Hz output bandwidth. It is effectively the amplitude of the detector white noise after the raw DAC counts are converted to Watts, and it is measured in units of $\mathrm{W}/\sqrt{Hz}$[39].

The sensitivity of a detector is quantified by the noise equivalent temperature (NET), which is the temperature fluctuation that gives signal-to-noise ratio of one after integrating over one second. As such, a lower NET indicates a more sensitive detector. It can be calculated from the NEP using

$$\mathrm{NET} = \frac{\mathrm{NEP}}{\epsilon_{\mathrm{abs}} \frac{dP}{dT} \sqrt{2}}, \tag{4.1}$$

where ϵ_{abs} is the optical efficiency of the detector (Sec. 3.4) and $\epsilon_{\mathrm{abs}} dP/dT$ is the conversion factor between temperature observed by and power deposited onto the detector. The units of NET are $\mathrm{K}\sqrt{s}$, and the factor of $\sqrt{2}$ is there to convert $1/\sqrt{\mathrm{Hz}}$ to $\sqrt{s}$, since an output bandwidth of 1 Hz is equivalent to half a second of integration time. The NETs of the ABS detectors were calculated by John Appel [3] and are shown in Figure 4.5. From now on s_i will be used to denote the NET of detector i, and the total array sensitivity is determined by

$$s = \left(\sum_i \frac{1}{s_i^2} \right)^{-1/2}. \tag{4.2}$$

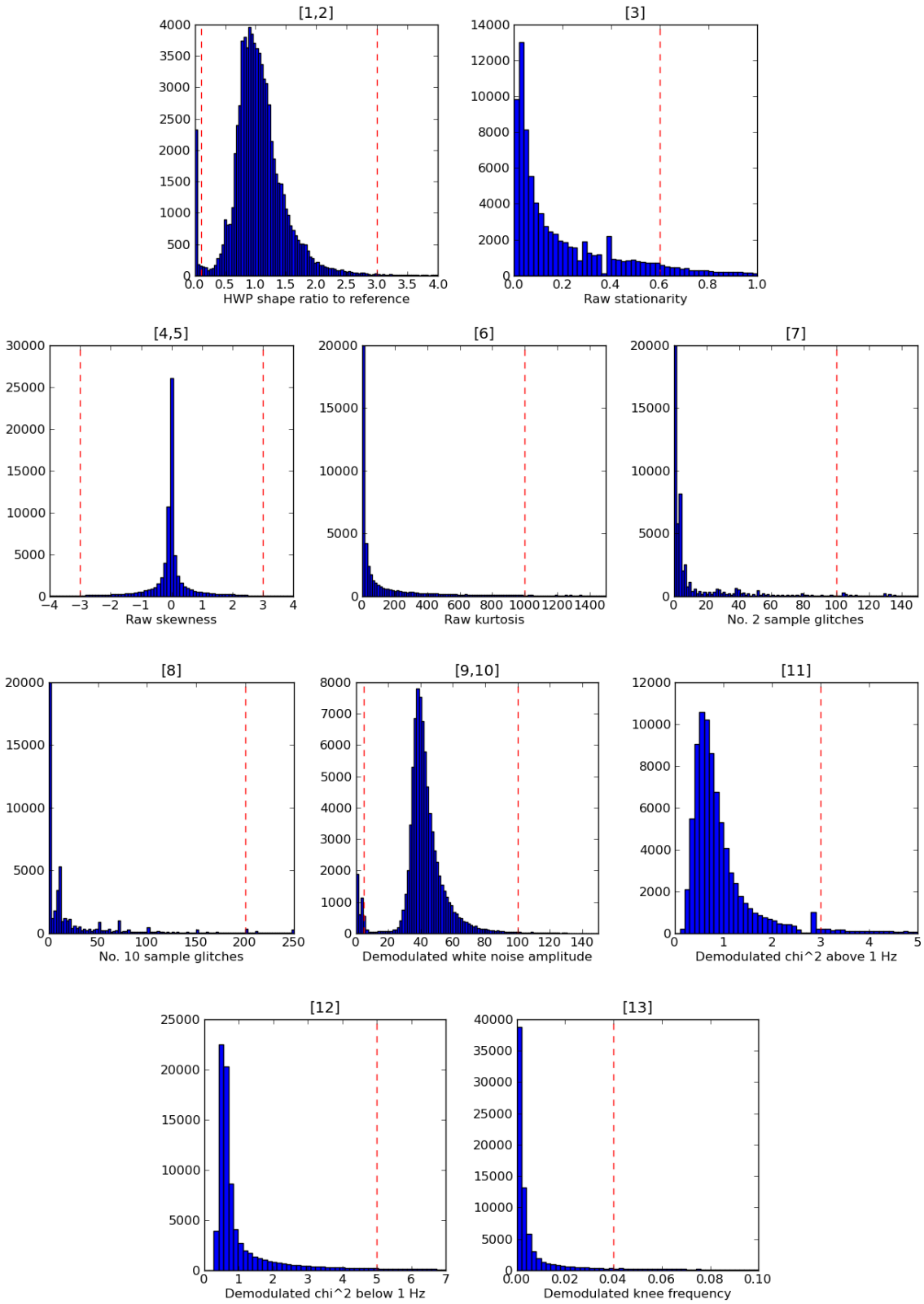

Figure 4.3: Distributions of parameters on which the cuts are made, over CESes during Field A observations in the reference period (see text). The red dashed lines represents the first pass at the cut level.

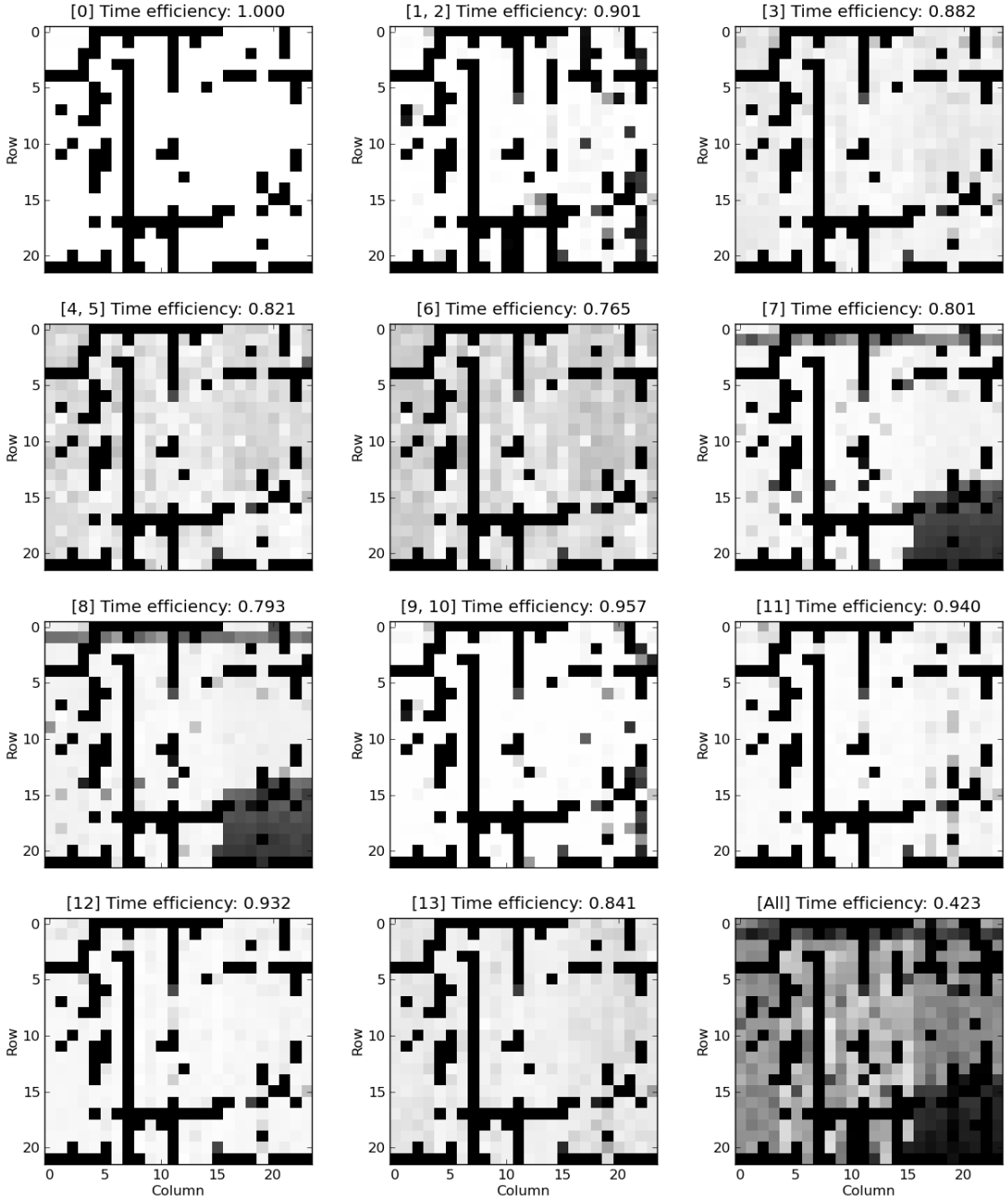

Figure 4.4: Time efficiency of each detector, for each cut individually. A detector is represented by a square in the grid, The cuts applied in each frame are indicated by the number(s) in square brackets in the titles, and correspond to the cuts in Table 4.1. Panels [7] and [8] capture the large number of glitches in the detectors which have a high number row and column. The reasons for these glitches is not fully understood.

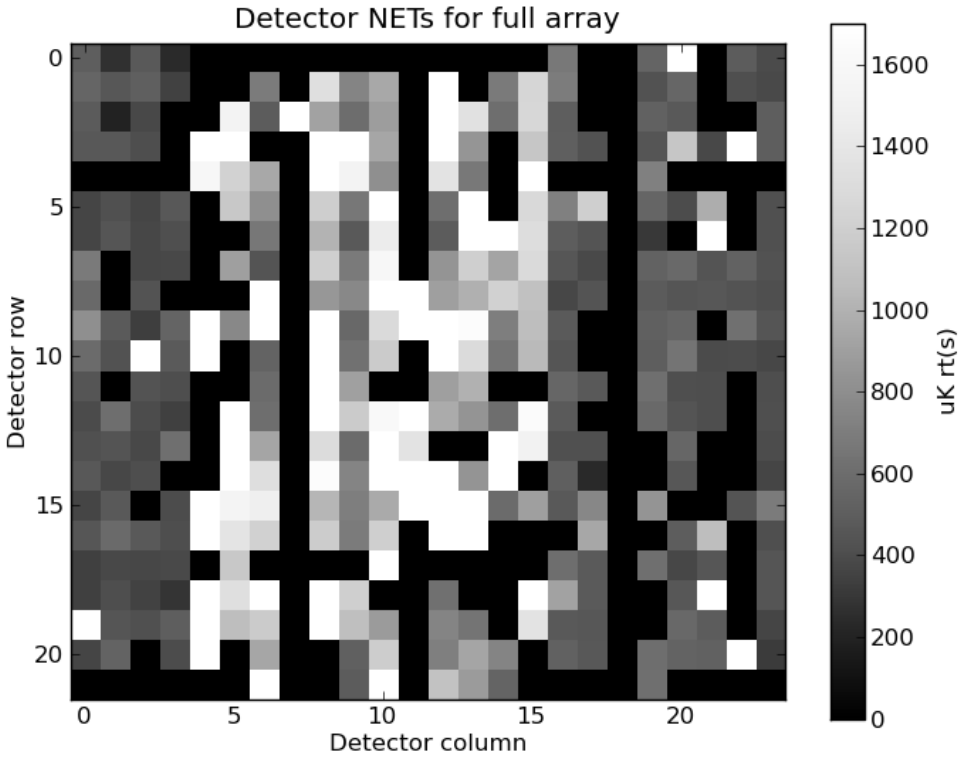

Figure 4.5: Noise equivalent temperature (NET) of all ABS detectors. Black squares represent dark and otherwise not working detectors, and white squares detectors whose NET is greater than 1700 $\mu\mathrm{K}\sqrt{s}$. Most of the latter are in columns $4-15$, which are detectors in the 'bottom' half of the focal plane as in Figure 2.7.

We define the effective array sensitivity for period of observation time t_{obs} as

$$s_{\mathrm{eff}} = \left(\sum_i \frac{t_i}{s_i^2 t_{\mathrm{obs}}} \right)^{-1/2}, \tag{4.3}$$

where t_i is the total time during which detector i passes the selection criteria. The effective sensitivity s_{eff} can never be less than s, and matches it only when $t_i = t_{\mathrm{obs}}$ for all i. The sensitivity of the ABS focal plane including all optically coupled detectors is 30 $\mu\mathrm{K}\sqrt{s}$. Cutting detectors with low optical efficiencies increases this by less than $\sim 0.1\%$. The effect of each selection criterion considered separately on the focal plane effective sensitivity is shown in Table 4.2.

Selection Criteria	Sensitivity (μK$\sqrt{s}$)
Full array	30.5(67)
Relative optical efficiency $\epsilon_{\rm rel} \geq 0.2$	30.5(71)
HWP shape ratio to reference≥ 0.1	31.2
HWP shape ratio to reference ≤ 3.0	30.6
Raw stationarity ≤ 0.6	33.1
Raw skewness ≥ -3	32.5
Raw skewness ≤ 3	32.4
Raw kurtosis ≤ 1000	36
No. 2 sample glitches ≤ 100	34
No. 10 sample glitches ≤ 200	35
Demodulated white noise amplitude ≥ 5	30.7
Demodulated white noise amplitude ≤ 100	30.9
χ^2 above 1Hz ≤ 3	31.8
χ^2 below 1Hz ≤ 5	31.8
Demodulated knee frequency≤ 0.04	33.8
All cuts	48.4

Table 4.2: Effective array sensitivity for various detector and data cuts. The sensitivity of the full array is calculated using NETs measured by John Appel. All the other effective array sensitivities impose a relative optical efficiency cut-off of 0.2 (Sec. 3.4). The biggest hits to the sensitivity come from the kurtosis and glitch criteria.

4.1.5 Possibilities for Future Selection Criteria

As described above, the current limits on stationarity, skewness and kurtosis are primarily in place to flag jumps and glitches, and end up cutting a lot of healthy data in the process. Having a cut criterion directly for jumps would allow us to relax these limits to include more data without the the chance of letting a jump slip through. A jump-finding algorithm is currently in development, and once that is implemented the proper limits to place on the stationarity, skewness, and kurtosis in the absence of jumps will be determined.

There is an of over-counting of glitches with the current glitch finding algorithm, primarily due to large amplitude single-sample glitches. The algorithm was written before the single sample glitches were discovered, and was meant to target the generally much smaller amplitude 2- and 10- sample glitches. If a glitch is big enough, it

affects the mean offset removal of an entire 25 (50) sample interval in the short (long) glitch finder, and when compared to zero, all 25 (50) samples are flagged as glitches. This artifact is visible in the distributions of the number of glitches as regular spikes every 25 (50) samples (Fig. 4.6). Four or more large single-sample glitches in a CES will cause it to be flagged as over the current limits of both the 2- and 10-sample criteria, indicating that the $\sim 20\%$ of the data which is cut by each of these limits is largely overlapping. A new iteration of the glitch finding algorithm is currently being implemented by Akito Kusaka which removes the median offset as opposed to the mean offset. In this way a glitch of any size would not significantly affect the offset, and the mask would be applied properly to the glitch and not to the entire interval. This change is expected to recover at least 75% of the data cut due to glitches.

4.2 Sensitivity

As mentioned in Chapter 1, the primary goal of ABS is to probe the tensor-to-scalar ratio of the primordial perturbations, r. The current limit on r from CMB data only is 0.12 from Planck[33]. In this section we estimate the sensitivity to r which ABS will be able to achieve, from observations during the one month reference period, October 10 - November 7, 2012. Based on these results, estimates of the minimum r for the entire first season and projections including the second season are made.

Consider a single detector i with sensitivity s_i observing temperature fluctuations $\langle \delta T \rangle$ over a patch of sky. For each pixel, the temperature has contributions from both the CMB and the noise,

$$\delta T_{\rm pix} = \delta T_{\rm pix}^{\rm CMB} + \delta T_{\rm pix}^{\rm noise}. \tag{4.4}$$

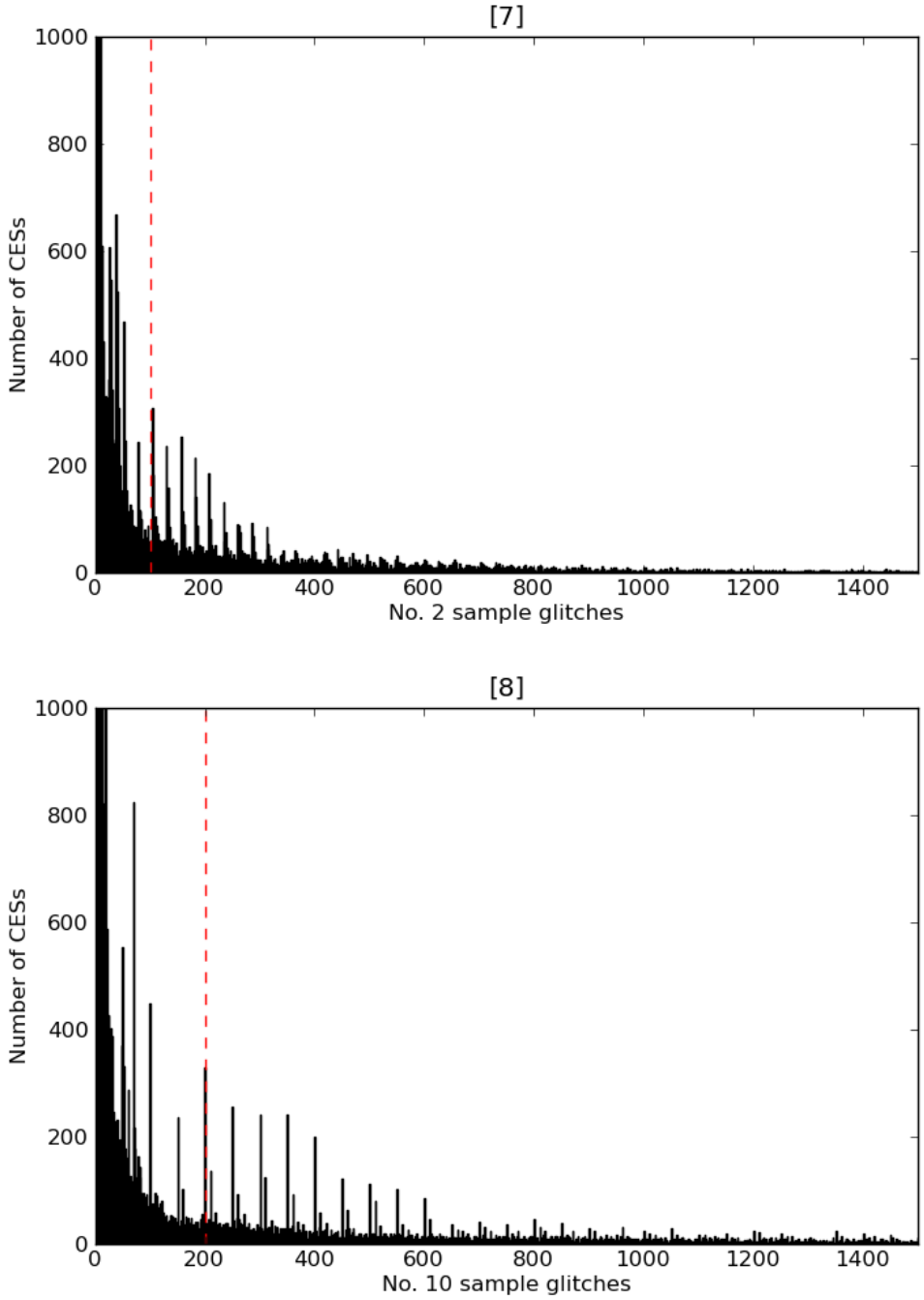

Figure 4.6: Histograms of the number of glitches per constant elevation scan (CES), zoomed in on the y-axis so that the features are distinguishable. The regular peaks are an artifact of the first iteration of the glitch finding algorithm, which counts one large single-sample glitch as 25 2-sample glitches and 50 10-sample glitches. A timestream with 4 or more such single-sample glitches is cut entirely due to this artifact.

The noise variance is assumed to be uncorrelated for different pixels, and follows the relation

$$\langle \delta T_{\rm pix}^{\rm noise} T_{\rm pix'}^{\rm noise} \rangle = \sigma_{{\rm pix},i}^2 \delta_{\rm pix,pix'}, \tag{4.5}$$

where $\sigma_{{\rm pix},i} = s_i/\sqrt{t_{{\rm pix},i}}$ and $t_{{\rm pix},i}$ is the time detector i spent observing the pixel. In other words, $\sigma_{{\rm pix},i}$ represents the temperature fluctuation of the pixel that can be observed with signal-to-noise ratio of unity after 1 second of observation with detector i. It is convenient to work with the weight of the pixel, $w_{{\rm pix},i} \equiv \sigma_{{\rm pix},i}^{-2}$. The weight per solid angle, $w_{{\rm pix},i}/\Omega_{\rm pix}$, is a measure of noise that is independent of pixel size $\Omega_{\rm pix}$, allowing for comparison among experiments with varying beam sizes.

To generalize this result to include multiple detectors in the focal plane, one can simply add the weights for each detector for each pixel,

$$w = \sum_{\rm pix} w_{\rm pix} = \sum_{\rm pix} \left(\sum_i w_{{\rm pix},i} \right). \tag{4.6}$$

For observation strategies like the one ABS uses, which observe Q and U polarizations equally, the weight for polarization is obtained from the total weight by taking $w_{Q,U} = w/2$. Figure 4.7 shows the weight map of Field A observation. Summing over all pixels gives a weight of $(0.057\mu{\rm K})^{-2}$, and an average weight per solid angle of $(3.13\mu{\rm K})^{-2}$ deg^{-2}. The average weights per solid angle for polarization are then $w_{Q,U} = (6.26\mu{\rm K})^{-2}{\rm deg}^{-2} = (376\mu{\rm K})^{-2}{\rm arcmin}^{-2}$.

With the weight map in hand we can estimate how well ABS will be able to probe r using the Knox equation [23], which gives the expected error per multipole coefficient C_ℓ:

$$\frac{\Delta C_\ell}{C_\ell} = \sqrt{\frac{2}{2\ell+1}} \left(1 + \frac{W_\ell}{w C_\ell} \right). \tag{4.7}$$

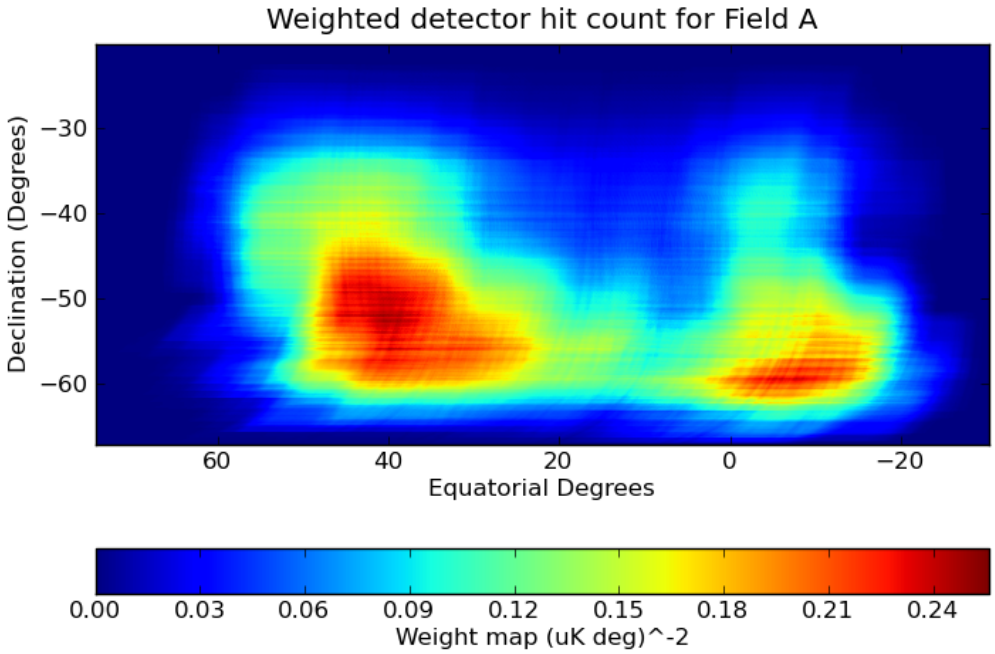

Figure 4.7: The weighted detector hit count for Field A observations during the reference period. The total area is 2940 deg^2 and the weight per solid angle is $(3.13\mu\text{K})^{-2}\text{deg}^{-2}$. This gives a polarization weight of $(6.26\mu\text{K})^{-2}\text{deg}^{-2}$. Compare with the raw hit count in Figure 4.1.

As expected, a larger weight w will result in smaller error bars. Here, W_ℓ is called the window function, which is the analog of the Fourier Transform in multipole pace of the beam profile. For a Gaussian beam with full width at half-maximum θ_{FWHM}, $P(\theta) = P_0 \exp(-\theta^2/2\sigma_b^2)$ where $\sigma_b = \theta_{\text{FWHM}}/\sqrt{8\ln 2}$. In this case window function is also Gaussian[44, 29], taking the form

$$W_\ell = e^{-[\ell(\ell+1)]^2\sigma_b^2}. \tag{4.8}$$

Narrow beams will have a larger window function for higher ℓ, and will thus be more sensitive to smaller scales. In effect W_ℓ is a low-pass filter, representing the smearing

done by a finite beam on scales smaller than its characteristic size. The ABS beam has $\theta_{\mathrm{FWHM}} = 0.58^\circ$ as calculated from Jupiter and Tau A observations by Srinivasan Raghunathan and Jon Sievers. As can be seen from its window function (Fig. 4.8), ABS is sensitive to scales $\ell <\sim 250$.

The second term in Eq. 4.7, quantifies the error from instrument noise. Even with a perfect instrument however, the error on measurements of C_ℓ will not be zero. This is because each C_ℓ represents an average over a finite number $(2\ell + 1)$ of $a_{\ell m}$ coefficients (Sec. 1.1.2), and as such there will always be sample variance. In the context of CMB power spectra, this effect is known as cosmic variance. The error due to cosmic variance is largest for small ℓ, and decreases as $1/\sqrt{\ell}$. The cosmic variance term becomes important for drawing conclusions from the power spectra about cosmological implications, and in particular inflation. For describing ABS's sensitivity to the observed BB spectrum, which the remainer of this section does, the relevant term is the second one. In the case where only a fraction of the sky, f_{sky}, is being observed with a Gaussian beam, the uncertainty becomes

$$\Delta C_\ell = \sqrt{\frac{2}{(2\ell+1) f_{sky}}} \left(w e^{[\ell(\ell+1)]^2 \sigma_b^2} \right)^{-1}. \tag{4.9}$$

Figures 4.8, 4.9, and 4.10 show the estimated binned errors for three different weights. The first is the weight achieved with the current set of selection criteria. The second is the weight calculated for the same reference period, assuming that 80% of the data can be recovered. The final one assumes the same sensitivity as the second, but for a full year of observation time. The power spectra are simulations from the Code for Anisotropies in the Microwave Background[1] (CAMB) using the parameters most favored by Planck. With the weights ABS is expected to achieve, the ΔC_ℓs are much bigger than even C_ℓ^{EE}. Binning them over a set of ℓs to reduces

[1] Available on NASA's Legacy Archive for Microwave Background Data Analysis (LAMBDA).

the overall uncertainty of the bin to

$$\Delta C_{\mathrm{bin}} = \left(\frac{1}{\Delta C_\ell^2} \right)^{-1/2}. \tag{4.10}$$

Bin sizes in the figures are chosen such that as many significant detection bins are displayed as possible.

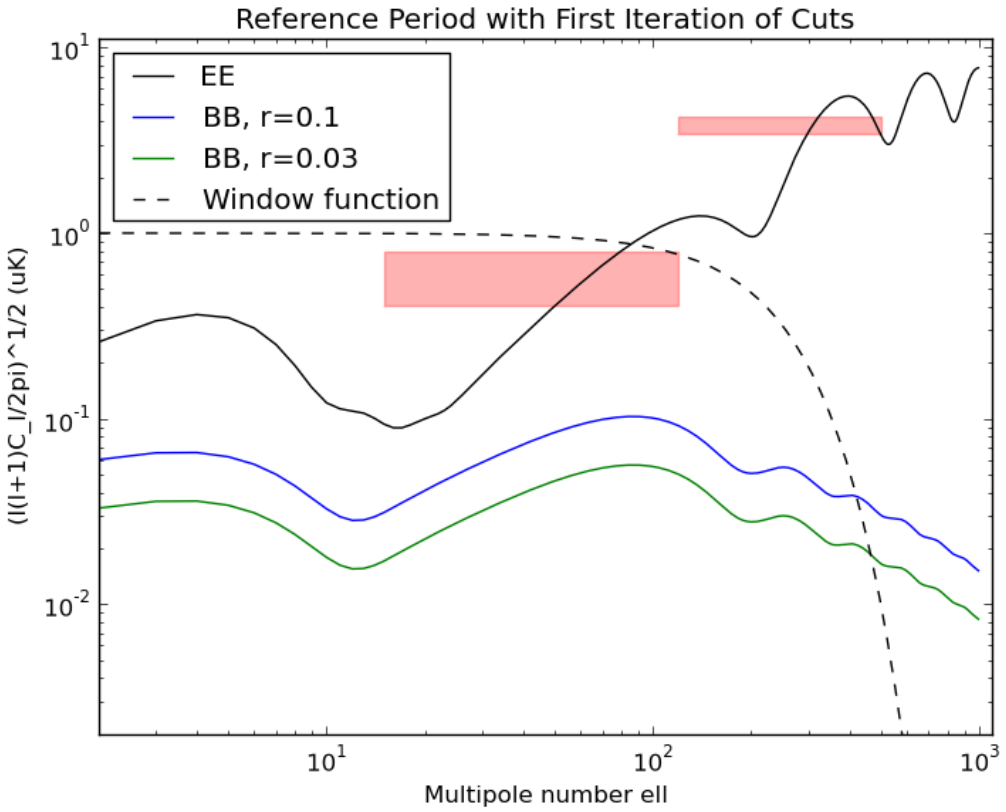

Figure 4.8: The sensitivity of ABS for the one month reference period and the first iteration of cuts. Shown are the EE power spectrum and the BB spectra for two different reference values of the tensor to scalar ratio r, for a ΛCDM cosmology with the most recent Planck parameters. The estimated binned error for the EE spectrum is shown in light red. The effective focal plane sensitivity is 48.5 $\mu\mathrm{K}\sqrt{s}$ and the average weight over the field is $(6.26\ \mu\mathrm{K})^{-2}\mathrm{deg}^{-2}$. With the current cuts for the reference period, ABS should be able to detect the E modes, although it will not be sensitive enough to discern the features of the power spectrum. The window function is calculated assuming a Gaussian beam with full width at half maximum of 0.58°.

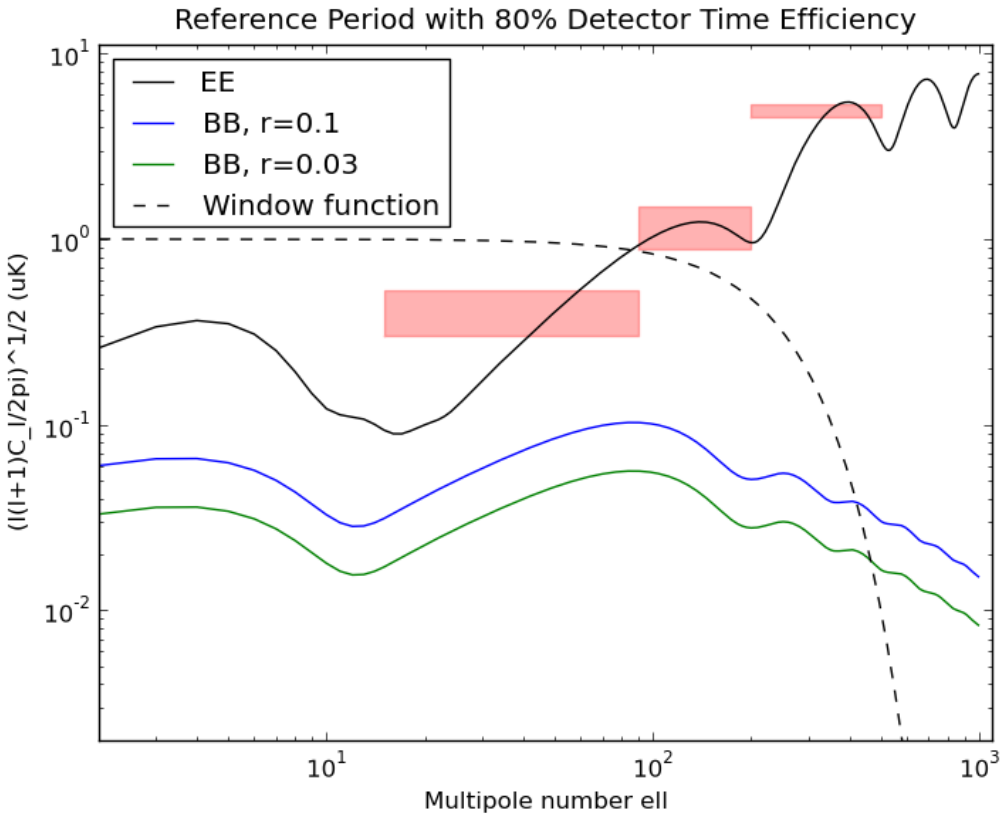

Figure 4.9: Similar plot to that shown in Figure 4.8. The binned errors for the EE spectrum assume an even coverage of 2000 deg^2 and a detector time efficiency of 80%, believed to be achievable with improved data selection algorithms. In this case the focal plane sensitivity would be 34.2 μK$\sqrt{s}$, and the weight would be (1.7 μK)$^{-2}$deg^{-2}. At this sensitivity the features of the E mode power spectrum start to appear, but B modes below $r = 0.1$ are still inaccessible, even when the error is binned over the entire peak of the BB spectrum, $\ell = 15 - 250$.

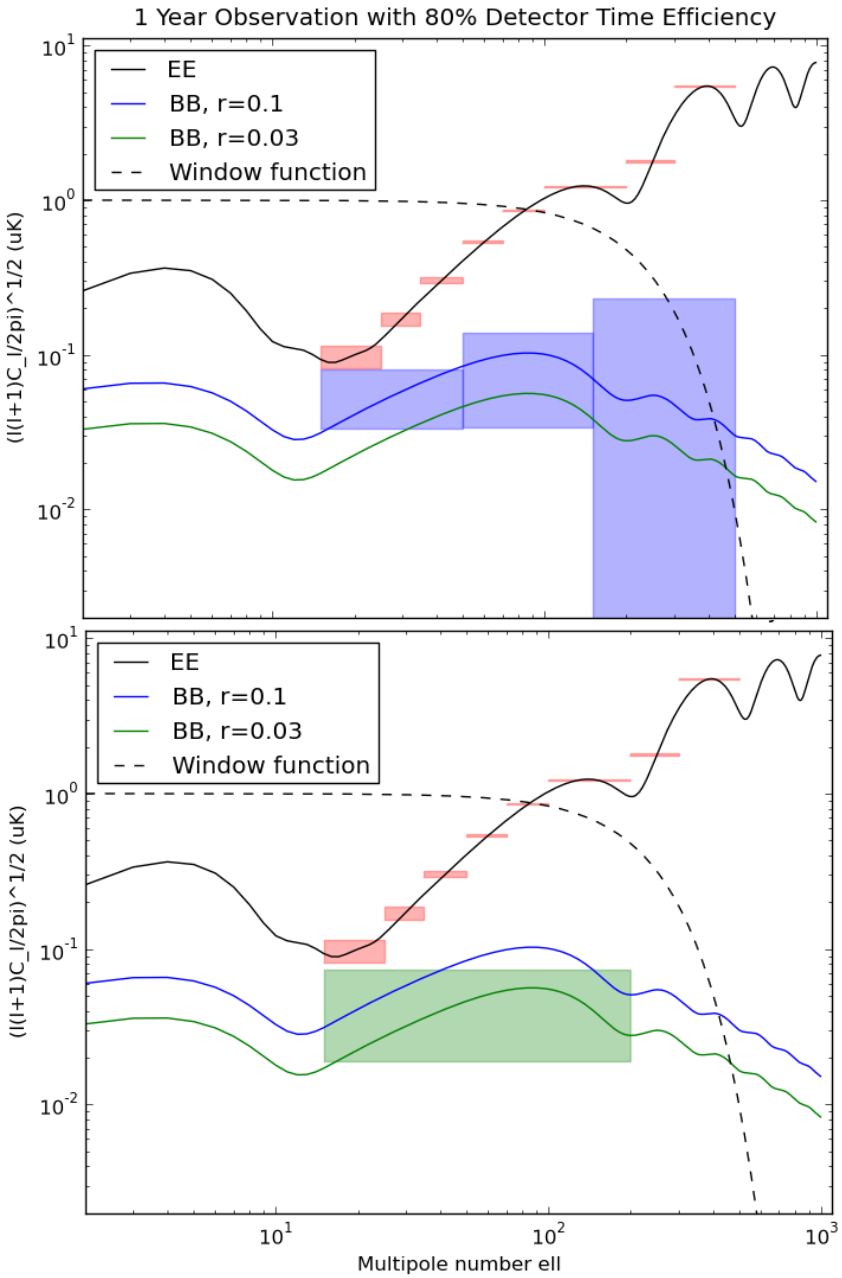

Figure 4.10: Projected sensitivity of ABS after one year of observations on Field A. As in Figure 4.9, a detector time efficiency of 80% is assumed as well as even coverage over 2000 deg^2. The array sensitivity is still 34.2 μK$\sqrt{s}$, and with the roughly 40-fold increase in observation time the weight would increase to (0.27 μK)$^{-2}$deg^{-2}. At this sensitivity the EE spectrum is clearly visible. The top and bottom figures are the same except that the top displays the binned errors for $r = 0.1$ (blue boxes) and the bottom for $r = 0.03$ (green boxes). If ABS can achieve a 80% detector time efficiency, after one year of observation it will be able to detect approximately an r of 0.03.

4.3 Maps

To make maps from the ABS data, we run the mapmaking code Ninkasi on the SciNET General Purpose Cluster (GPC). Ninkasi was originally written (lead, Jonathan Sievers) to map data from the Atacama Comology Telescope (ACT) [14, 18], and was extended for use with ABS data by Jon Sievers and Mike Nolta. It makes unbiased, maximum likelihood maps by finding the map of the sky that minimizes χ^2 of the bolometer data using a preconditioned conjugate-gradient method (PCG), with a special focus on handling complicated correlated noises. The maps presented of Field A are in a cylindrical equal-area (CEA) projection with a standard latitude of $\delta = -43.7$, the central declination of the patch, and with a pixel size of $5'$, one seventh of the beam FWHM. Figure 4.11 shows the preliminary maps after 1400 iterations of mode removal with the current set of data cuts.

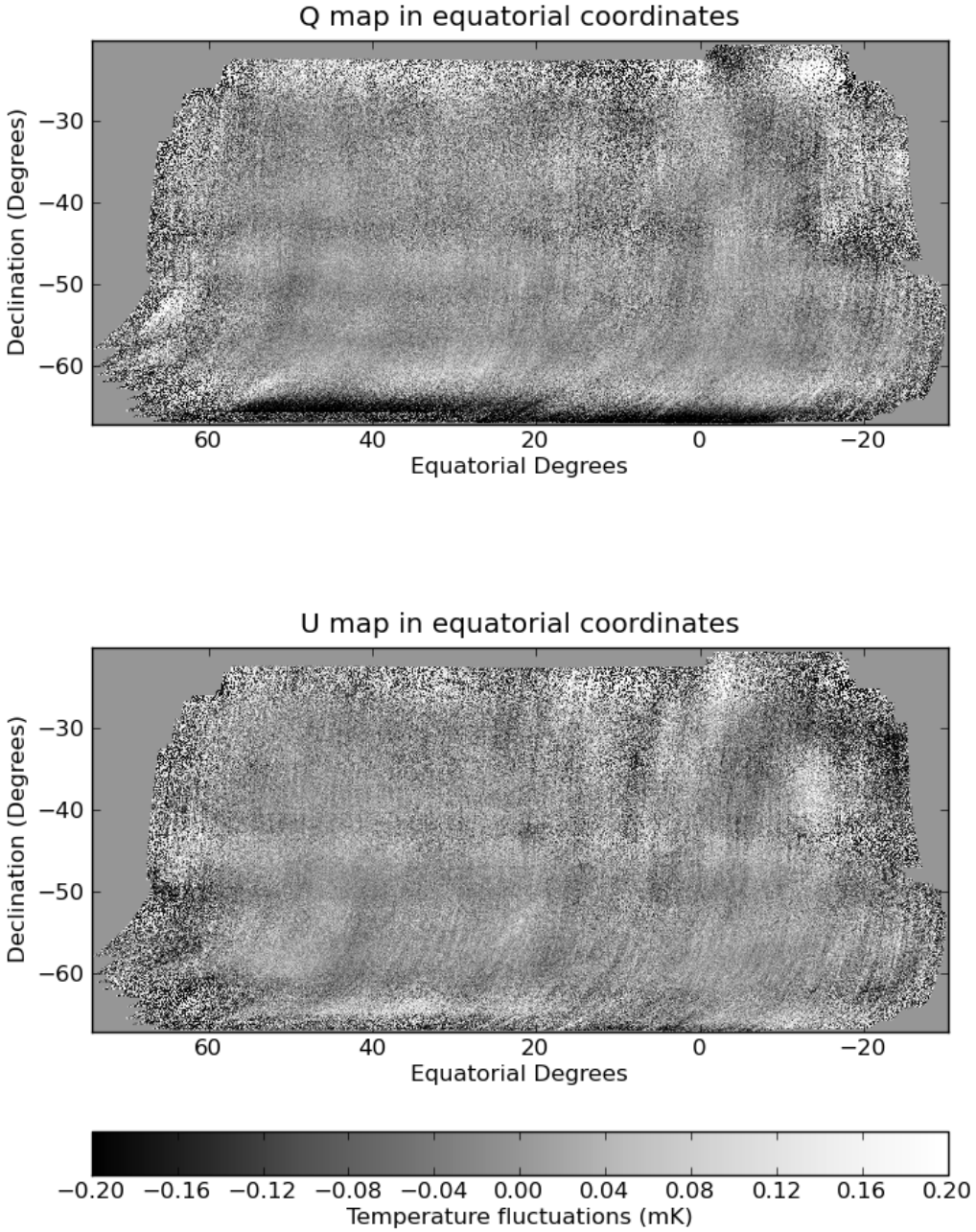

Figure 4.11: Preliminary Q and U maps for Field A. The sky moves across the field of view in the horizontal direction, and so the horizontal striping is likely due to a ground pick-up profile.

4.4 Current Status

ABS is currently in its second season of observation, which started on March 29. Since that time, ABS has been observing for a total of 622 hours, approximately 30% calendar time. Of those, 343 hours were spent on Field A. The main causes of down time this season so far have been severe weather conditions, and complications due to the deployment of ACTpol currently underway, such as increased loading on the generators. These complications are anticipated to be resolved very soon, since ACTpol is on the brink of starting regular operation. Several changes were implemented since the last season to make ABS operation more robust and reduce down time due to maintenance, most notably the addition of a wooden wheel inserted in the cable wrap to ease the strain on the pulse tube lines. The wheel was added during the December 2012 down time, and as of July 11, 2013 when this was written the pulse tube lines are still in good condition.

For this season, now that we have a better understanding the data from the instrument, our primary goal is to observe Field A for as many hours as possible in order to reach our projected sensitivity.

Chapter 5

Addendum

The methods described in Chapter 4 represent a first pass at the data selection, and the findings led to a number of improvements that were implemented by the team. We now recover 218 hours during the reference period (92% of the observing time). This leads to an improvement in the net sensitivity to 38 $\mu\mathrm{K}\sqrt{s}$. The CES distributions and time efficiencies associated with these cuts are shown in Figures 5.1 and 5.2.

The changes that most increased the percentage of data recovery and the effective focal plane sensitivity were adjustments to the glitch finding algorithm (Sec. 4.1.1) and the DC offset removal (Sec. 4.1.2). More specifically, the former involved a subtraction of the *median* value of each 25 or 50 sample interval, rather than the mean value, preventing a single large glitch from affecting the baseline average of an entire interval. As seen in Figure 5.3, this change removes the artifact appearing as regular peaks in Figure 4.6. The latter change involved moving the DC offset removal step to after the timestream de-Butterworthing step. This had the greatest impact on the kurtosis calculation for each timestream, bringing the average down to below one, compared to ~ 100 for the first iteration.

Selection Criteria	Sensitivity (μK$\sqrt{s}$)
Full array	30.6
HWP shape ratio to reference$\geq$ 0.2	31.3
HWP shape ratio to reference $\leq$ 2.0	31.0
Raw stationarity $\leq$ 0.2	32.5
Raw skewness ≥ -0.3	30.9
Raw skewness $\leq$ 0.3	30.9
Raw kurtosis $\leq$ 5	31.6
No. 2 sample glitches $\leq$ 40	32.1
No. 10 sample glitches $\leq$ 200	31.5
Demodulated white noise amplitude $\geq$ 20	30.8
Demodulated white noise amplitude $\leq$ 100	30.9
χ^2 above 1Hz $\leq$ 3	31.8
χ^2 below 1Hz $\leq$ 4	32.2
Demodulated knee frequency$\leq$ 0.02	34.5
All cuts	37.7

Table 5.1: Effective array sensitivity for the second pass at data cuts. There is a $\sim$ 25% improvement compared to the first pass.

The second pass at data selection has lead to a $\sim$ 25% improvement in the focal plane sensitivity (Tab. 5.1). Related improvements to the algorithms and thresholds will continue to be made over the following months.

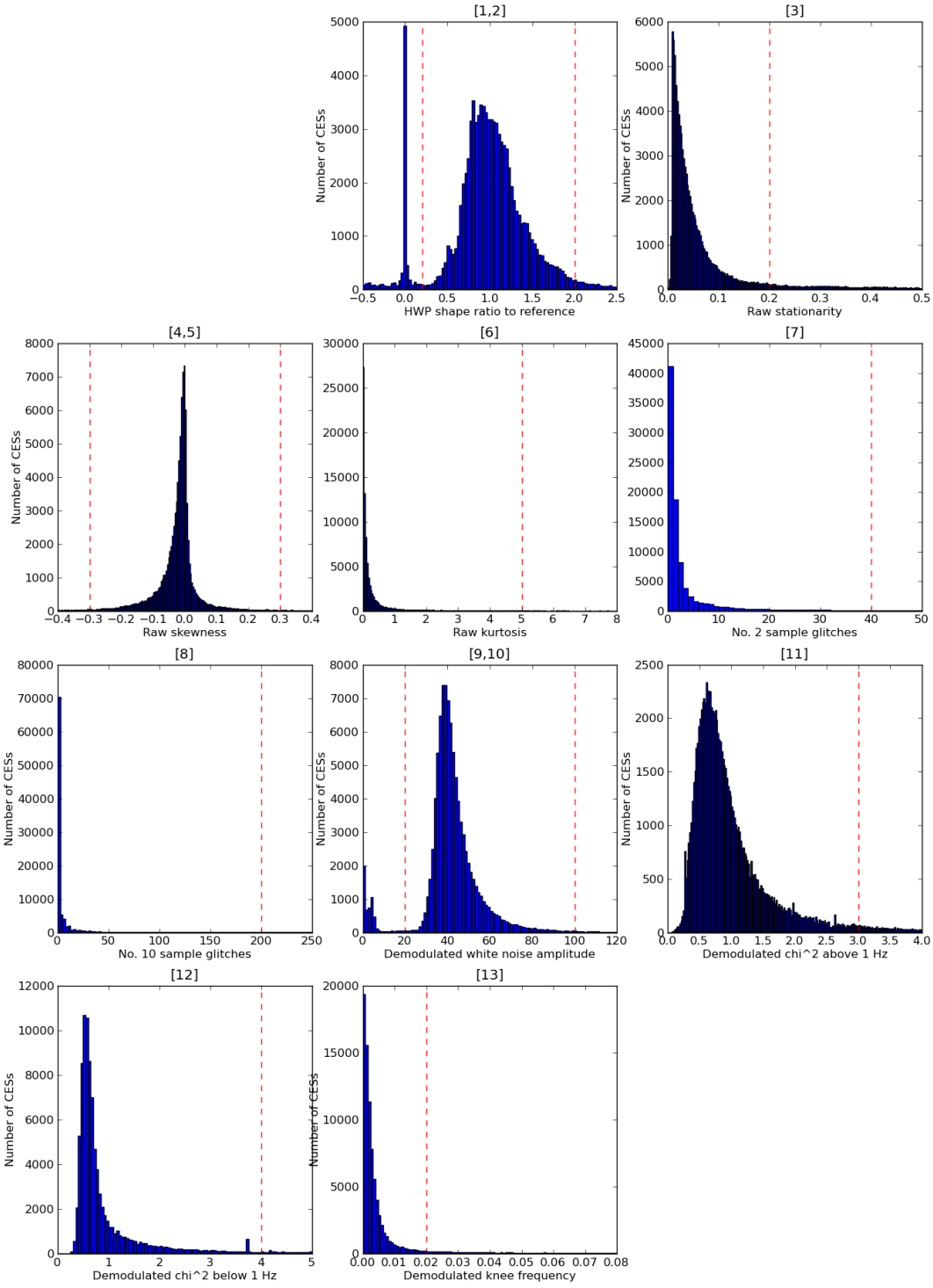

Figure 5.1: Distributions of CESes during Field A observations in the reference period using the second iteration of the data processing algorithm. Compare to Figure 4.3.

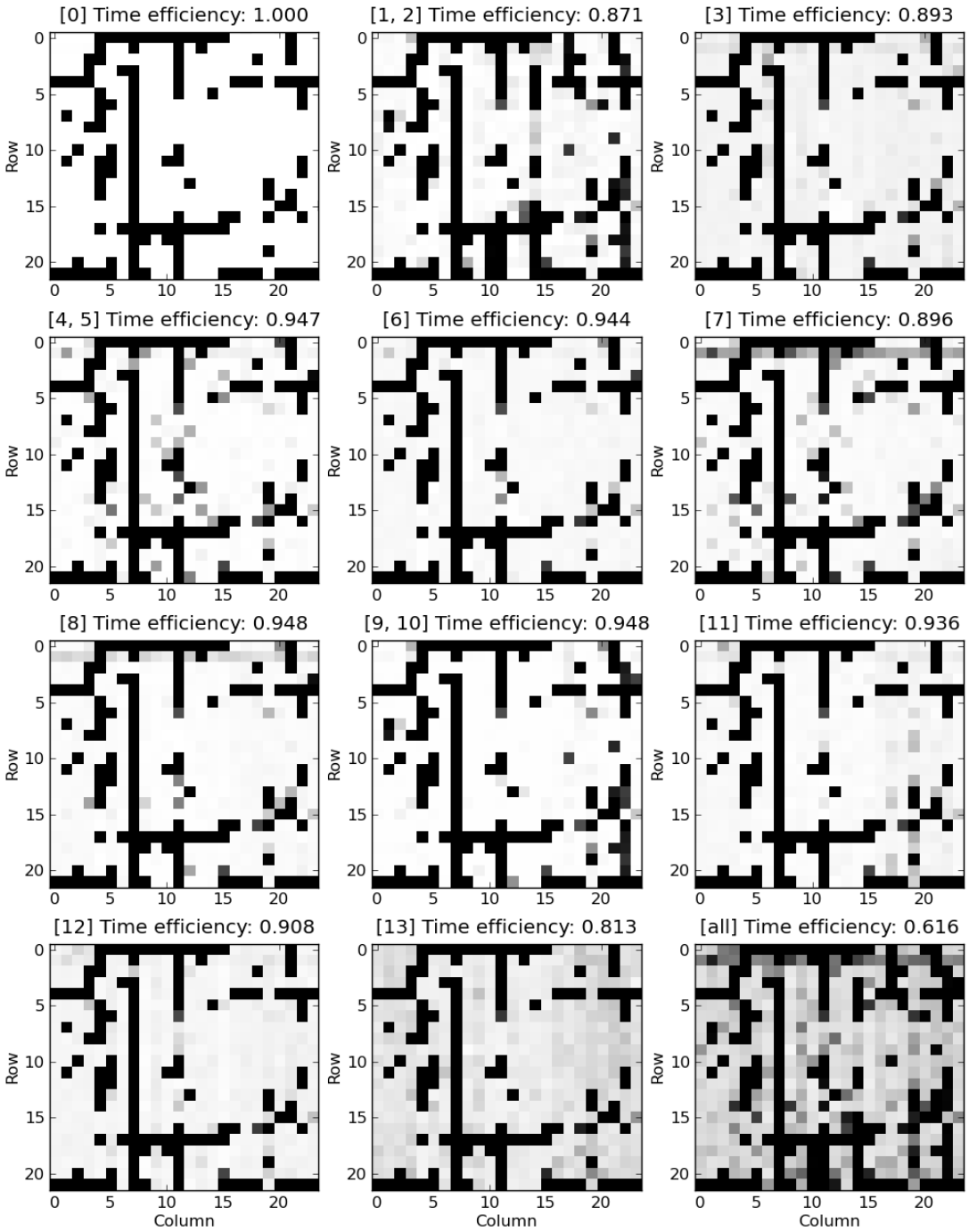

Figure 5.2: Time efficiency of each detector for each cut individually, with the second iteration of data selection criteria. A detector is represented by a square in the grid. The cuts applied in each frame are indicated by the number(s) in square brackets in the titles, and correspond to the cuts in Figure 5.1.

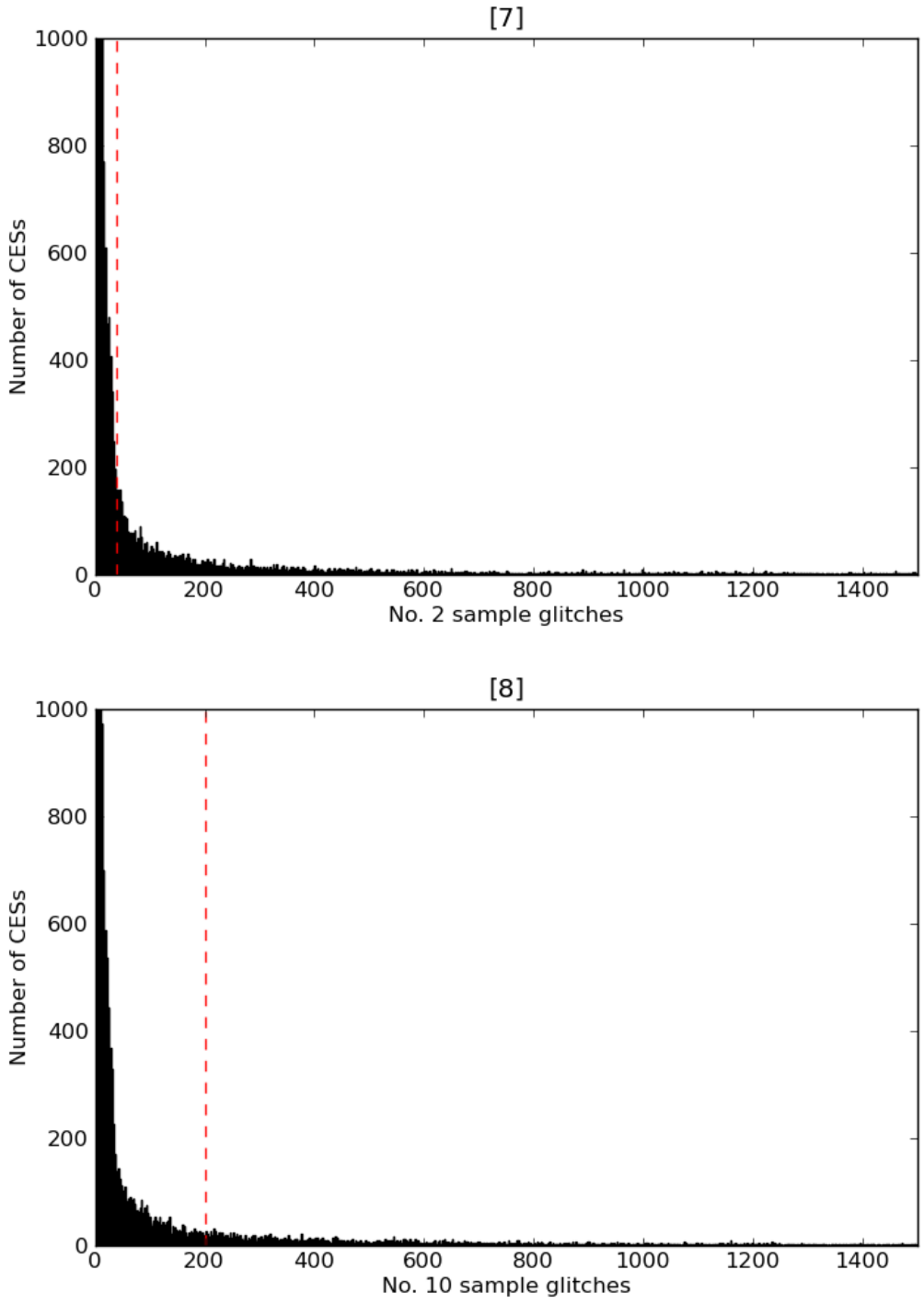

Figure 5.3: Histograms of the number of glitches per constant elevation scan (CES), zoomed in on the y-axis, similarly to Figure 4.6.

Bibliography

[1] Chajnantor Weather Model. http://almascience.eso.org/about-alma/weather/atmosphere-model.

[2] R. A. Alpher and R. Herman. Evolution of the Universe. *Nature*, 162:774–775, 1948.

[3] J. W. Appel. *Detectors for the Atacama B-mode Search Experiment*. PhD thesis, Princeton University, September 2012.

[4] J. E. Austermann, K. A. Aird, J. A. Beall, D. Becker, A. Bender, B. A. Benson, L. E. Bleem, J. Britton, J. E. Carlstrom, C. L. Chang, H. C. Chiang, H. M. Cho, T. M. Crawford, A. T. Crites, A. Datesman, T. de Haan, M. A. Dobbs, E. M. George, N. W. Halverson, N. Harrington, J. W. Henning, G. C. Hilton, G. P. Holder, W. L. Holzapfel, S. Hoover, N. Huang, J. Hubmayr, K. D. Irwin, R. Keisler, J. Kennedy, L. Knox, A. T. Lee, E. Leitch, D. Li, M. Lueker, D. P. Marrone, J. J. McMahon, J. Mehl, S. S. Meyer, T. E. Montroy, T. Natoli, J. P. Nibarger, M. D. Niemack, V. Novosad, S. Padin, C. Pryke, C. L. Reichardt, J. E. Ruhl, B. R. Saliwanchik, J. T. Sayre, K. K. Schaffer, E. Shirokoff, A. A. Stark, K. Story, K. Vanderlinde, J. D. Vieira, G. Wang, R. Williamson, V. Yefremenko, K. W. Yoon, and O. Zahn. SPTpol: an instrument for CMB polarization measurements with the South Pole Telescope. *Proc. SPIE 8452, Millimeter, Submillimeter, and Far-Infrared Detectors and Instrumentation for Astronomy VI, 84520E (September 27, 2012)*, 10 2012, e-print arXiv:1210.4970.

[5] D. Baumann, M. G. Jackson, P. Adshead, A. Amblard, A. Ashoorioon, N. Bartolo, R. Bean, M. Beltran, F. de Bernardis, S. Bird, X. Chen, D. J. H. Chung, L. Colombo, A. Cooray, P. Creminelli, S. Dodelson, J. Dunkley, C. Dvorkin, R. Easther, F. Finelli, R. Flauger, M. Hertzberg, K. Jones-Smith, S. Kachru, K. Kadota, J. Khoury, W. H. Kinney, E. Komatsu, L. M. Krauss, J. Lesgourgues, A. Liddle, M. Liguori, E. Lim, A. Linde, S. Matarrese, H. Mathur, L. McAllister, A. Melchiorri, A. Nicolis, L. Pagano, H. V. Peiris, M. Peloso, L. Pogosian, E. Pierpaoli, A. Riotto, U. Seljak, L. Senatore, S. Shandera, and E. Silverstein. CMBPol Mission Concept Study: Probing Inflation with CMB Polarization. *AIP Conf.Proc.*, 1141:10–120, 2009, e-print arXiv:0811.3919.

[6] D. J. Benford, M. C. Gaidis, and J. W. Kooi. Optical properties of zitex in the infrared to submillimeter. *Applied Optics*, 42(25):5118 – 5122, September 2003.

[7] C. L. Bennett, D. Larson, J. L. Weiland, N. Jarosik, G. Hinshaw, N. Odegard, K. M. Smith, R. S. Hill, B. Gold, M. Halpern, E. Komatsu, M. R. Nolta, L. Page, D. N. Spergel, E. Wollack, J. Dunkley, A. Kogut, M. Limon, S. S. Meyer, G. S. Tucker, and E. L. Wright. Nine-year wilkinson microwave anisotropy probe (wmap) observations: Final maps and results. 12 2012, e-print arXiv:1212.5225.

[8] E. F. Bunn. E/B mode mixing. 11 2008, e-print arXiv:0811.0111.

[9] P. J. B. Clarricoats and A. D. Olver. *Corrugated horns for microwave antennas*. Peter Peregrinus Ltd., 1984.

[10] S. Das, T. Louis, M. R. Nolta, G. E. Addison, E. S. Battistelli, J. R. Bond, E. Calabrese, D. C. M. J. Devlin, S. Dicker, J. Dunkley, R. Dünner, J. W. Fowler, M. Gralla, A. Hajian, M. Halpern, M. Hasselfield, M. Hilton, A. D. Hincks, R. Hlozek, K. M. Huffenberger, J. P. Hughes, K. D. Irwin, A. Kosowsky, R. H. Lupton, T. A. Marriage, D. Marsden, F. Menanteau, K. Moodley, M. D. Niemack, L. A. Page, B. Partridge, E. D. Reese, B. L. Schmitt, N. Sehgal, B. D. Sherwin, J. L. Sievers, D. N. Spergel, S. T. Staggs, D. S. Swetz, E. R. Switzer, R. Thornton, H. Trac, and E. Wollack. The atacama cosmology telescope: Temperature and gravitational lensing power spectrum measurements from three seasons of data. 01 2013, e-print arXiv:1301.1037.

[11] M. J. Devlin, S. R. Dicker, J. Klein, and M. P. Supanich. A high capacity completely closed-cyle 250 mK 3He refrigeration system based on a pulse tube cooler. *Cryogenics*, 44, September 2004.

[12] R. H. Dicke. The measurement of thermal radiation at microwave frequencies. *The Review of Scientific Instruments*, 17(7):268–275, 1946.

[13] R. H. Dicke, P. J. E. Peebles, P. G. Roll, and D. T. Wilkinson. Cosmic black-body radiation. *ApJ*, 142:414–419, 1965.

[14] R. Dünner, M. Hasselfield, T. A. Marriage, J. Sievers, V. Acquaviva, G. E. Addison, P. A. R. Ade, P. Aguirre, M. Amiri, J. W. Appel, L. F. Barrientos, E. S. Battistelli, J. R. Bond, B. Brown, B. Burger, E. Calabrese, J. Chervenak, S. Das, M. J. Devlin, S. R. Dicker, W. B. Doriese, J. Dunkley, T. Essinger-Hileman, R. P. Fisher, M. B. Gralla, J. W. Fowler, A. Hajian, M. Halpern, C. Hernández-Monteagudo, G. C. Hilton, M. Hilton, A. D. Hincks, R. Hlozek, K. M. Huffenberger, D. H. Hughes, J. P. Hughes, L. Infante, K. D. Irwin, J. B. Juin, M. Kaul, J. Klein, A. Kosowsky, J. M. Lau, M. Limon, Y.-T. Lin, T. Louis, and R. H. Lupton. The Atacama Cosmology Telescope: Data characterization and map making. 08 2012, e-print arXiv:1208.0050.

[15] J. R. Eimer, C. L. Bennett, D. T. Chuss, T. A. Marriage, E. J. Wollack, and L. Zeng. The Cosmology Large Angular Scale Surveyor (CLASS): 40 GHz optical design. *Proc. SPIE 8452, Millimeter, Submillimeter, and Far-Infrared Detectors and Instrumentation for Astronomy VI, 845220 (September 24, 2012)*, 11 2012, e-print arXiv:1211.0041.

[16] T. Essinger-Hileman. *Probing Inflationary Cosmology: The Atacama B-Mode Search (ABS)*. PhD thesis, Princeton University, September 2011.

[17] D. Fixsen. The temperature of the cosmic microwave background. *ApJ 709 (2009)*, 11 2009, e-print arXiv:0911.1955.

[18] J. W. Fowler, V. Acquaviva, P. A. R. Ade, P. Aguirre, M. Amiri, J. W. Appel, L. F. Barrientos, E. S. Battistelli, J. R. Bond, B. Brown, B. Burger, J. Chervenak, S. Das, M. J. Devlin, S. R. Dicker, W. B. Doriese, J. Dunkley, R. Dünner, T. Essinger-Hileman, R. P. Fisher, A. Hajian, M. Halpern, M. Hasselfield, C. Hernández-Monteagudo, G. C. Hilton, M. Hilton, A. D. Hincks, R. Hlozek, K. M. Huffenberger, D. H. Hughes, J. P. Hughes, L. Infante, K. D. Irwin, R. Jimenez, J. B. Juin, M. Kaul, J. Klein, A. Kosowsky, J. M. Lau, M. Limon, Y.-T. Lin, R. H. Lupton, T. A. Marriage, D. Marsden, K. Martocci, P. Mauskopf, F. Menanteau, K. Moodley, H. Moseley, C. B. Netterfield, M. D. Niemack, M. R. Nolta, L. A. Page, L. Parker, B. Partridge, H. Quintana, B. Reid, N. Sehgal, J. Sievers, and D. N. Spergel. The Atacama Cosmology Telescope: A measurement of the $600< \ell <8000$ cosmic microwave background power spectrum at 148 GHz. *Astrophysical Journal*, 722:1148–1161, 2010, e-print arXiv:1001.2934.

[19] A. A. Fraisse, P. A. R. Ade, M. Amiri, S. J. Benton, J. J. Bock, J. R. Bond, J. A. Bonetti, S. Bryan, B. Burger, H. C. Chiang, C. N. Clark, C. R. Contaldi, B. P. Crill, G. Davis, O. Doré, M. Farhang, J. P. Filippini, L. M. Fissel, N. N. Gandilo, S. Golwala, J. E. Gudmundsson, M. Hasselfield, G. Hilton, W. Holmes, V. V. Hristov, K. Irwin, W. C. Jones, C. L. Kuo, C. J. MacTavish, P. V. Mason, T. E. Montroy, T. A. Morford, C. B. Netterfield, D. T. O'Dea, A. S. Rahlin, C. Reintsema, J. E. Ruhl, M. C. Runyan, M. A. Schenker, J. A. Shariff, J. D. Soler, A. Trangsrud, C. Tucker, R. S. Tucker, A. D. Turner, and D. Wiebe. SPIDER: Probing the Early Universe with a Suborbital Polarimeter. *JCAP04(2013)047*, 06 2011, e-print arXiv:1106.3087.

[20] H. P. Gush, M. Halpern, and E. H. Wishnow. Rocket measurement of the cosmic-background-radiation mm-wave spectrum. *Physical Review Letters*, 65:537–540, 07 1990.

[21] G. Hinshaw, D. Larson, E. Komatsu, D. N. Spergel, C. L. Bennett, J. Dunkley, M. R. Nolta, M. Halpern, R. S. Hill, N. Odegard, L. Page, K. M. Smith, J. L. Weiland, B. Gold, N. Jarosik, A. Kogut, M. Limon, S. S. Meyer, G. S. Tucker, E. Wollack, and E. L. Wright. Nine-Year Wilkinson Microwave Anisotropy Probe (WMAP) Observations: Cosmological Parameter Results. 12 2012, e-print arXiv:1212.5226.

[22] J. Kaplan and QUBIC Collaboration. QUBIC, a bolometric interferometer to measure the B-modes of the CMB. 10 2009, e-print arXiv:0910.0391.

[23] L. Knox. Determination of inflationary observables by cosmic microwave background anisotropy experiments. *Phys.Rev.*, D52:4307–4318, 1995, e-print arXiv:astro-ph/9504054.

[24] J. M. Lau. *CCAM: A Novel Millimeter-Wave Instrument Using a Close-Packed TES Bolometer Array*. PhD thesis, Princeton University, October 2007.

[25] A. R. Liddle. Inflation and the cosmic microwave background. *AIPConf.Proc.*, 476:11–17, 1999, e-print arXiv:astro-ph/9901041.

[26] J. Mather, E. Cheng, R. E. Jr., R. Isaacman, S. Meyer, R. Schafer, R. Weiss, E. Wright, C. Bennett, N. Boggess, E. Dwek, S. Gulkis, M. Hauser, M. Janssen, T. Kelsall, P. Lubin, S. M. Jr., T. Murdock, R. Silverberg, G. Smoot, and D. Wilkinson. A preliminary measurement of the cosmic microwave background spectrum by the Cosmic Background Explorer (COBE) satellite. *ApJ*, 354:L37–L40, 1990.

[27] M. D. Niemack, P. A. R. Ade, J. Aguirre, F. Barrientos, J. A. Beall, J. R. Bond, J. Britton, H. M. Cho, S. Das, M. J. Devlin, S. Dicker, J. Dunkley, R. Dunner, J. W. Fowler, A. Hajian, M. Halpern, M. Hasselfield, G. C. Hilton, M. Hilton, J. Hubmayr, J. P. Hughes, L. Infante, K. D. Irwin, N. Jarosik, J. Klein, A. Kosowsky, T. A. Marriage, J. McMahon, F. Menanteau, K. Moodley, J. P. Nibarger, M. R. Nolta, L. A. Page, B. Partridge, E. D. Reese, J. Sievers, D. N. Spergel, S. T. Staggs, R. Thornton, C. Tucker, E. Wollack, and K. W. Yoon. ACTPol: A polarization-sensitive receiver for the Atacama Cosmology Telescope. *Proc. SPIE, Vol.*, 7741:77411S, 2010, e-print arXiv:1006.5049.

[28] A. D. Olver. Corrugated horns. *Electronics and Communication Engineering Journal*, pages 4–10, February 1992.

[29] L. Page, C. Jackson, C. Barnes, C. Bennett, M. Halpern, G. Hinshaw, N. Jarosik, A. Kogut, M. Limon, S. S. Meyer, D. N. Spergel, G. S. Tucker, D. T. Wilkinson, E. Wollack, and E. L. Wright. The optical design and characterization of the Microwave Anisotropy Probe. *Astrophys.J.*, 585:566–586, 2003, e-print arXiv:astro-ph/0301160.

[30] A. A. Penzias and R. W. Wilson. A measurement of excess antenna temperature at 4080 Mc/s. *ApJ*, 142:419–421, 1965.

[31] Planck Collaboration, P. A. R. Ade, N. Aghanim, C. Armitage-Caplan, M. Arnaud, M. Ashdown, F. Atrio-Barandela, J. Aumont, C. Baccigalupi, A. J. Banday, R. B. Barreiro, J. G. Bartlett, N. Bartolo, E. Battaner, K. Benabed, A. Benoit, A. Benoit-Levy, J.-P. Bernard, M. Bersanelli, P. Bielewicz, J. Bobin, J. J. Bock, A. Bonaldi, J. R. Bond, J. Borrill, F. R. Bouchet, M. Bridges, M. Bucher, C. Burigana, R. C. Butler, E. Calabrese, J.-F. Cardoso, A. Catalano, A. Challinor, A. Chamballu, L.-Y. Chiang, H. C. Chiang, P. R. Christensen, S. Church, D. L. Clements, S. Colombi, L. P. L. Colombo, F. Couchot,

A. Coulais, B. P. Crill, A. Curto, F. Cuttaia, L. Danese, R. D. Davies, R. J. Davis, P. de Bernardis, A. de Rosa, G. de Zotti, J. Delabrouille, J.-M. Delouis, F.-X. Desert, C. Dickinson, and J. M. Diego. Planck 2013 results. XXII. Constraints on inflation. 03 2013, e-print arXiv:1303.5082.

[32] Planck Collaboration, P. A. R. Ade, N. Aghanim, C. Armitage-Caplan, M. Arnaud, M. Ashdown, F. Atrio-Barandela, J. Aumont, C. Baccigalupi, A. J. Banday, R. B. Barreiro, J. G. Bartlett, E. Battaner, K. Benabed, A. Benoit, A. Benoit-Levy, J.-P. Bernard, M. Bersanelli, P. Bielewicz, J. Bobin, J. J. Bock, A. Bonaldi, L. Bonavera, J. R. Bond, J. Borrill, F. R. Bouchet, F. Boulanger, M. Bridges, M. Bucher, C. Burigana, R. C. Butler, E. Calabrese, J.-F. Cardoso, A. Catalano, A. Challinor, A. Chamballu, L.-Y. Chiang, H. C. Chiang, P. R. Christensen, S. Church, D. L. Clements, S. Colombi, L. P. L. Colombo, C. Combet, F. Couchot, A. Coulais, B. P. Crill, A. Curto, F. Cuttaia, L. Danese, R. D. Davies, R. J. Davis, P. de Bernardis, A. de Rosa, G. de Zotti, J. Delabrouille, J.-M. Delouis, and F.-X. Desert. Planck 2013 results. XV. CMB Power spectra and likelihood. 03 2013, e-print arXiv:1303.5075.

[33] Planck Collaboration, P. A. R. Ade, N. Aghanim, C. Armitage-Caplan, M. Arnaud, M. Ashdown, F. Atrio-Barandela, J. Aumont, C. Baccigalupi, A. J. Banday, R. B. Barreiro, J. G. Bartlett, E. Battaner, K. Benabed, A. Benoît, A. Benoit-Lévy, J.-P. Bernard, M. Bersanelli, P. Bielewicz, J. Bobin, J. J. Bock, A. Bonaldi, J. R. Bond, J. Borrill, F. R. Bouchet, M. Bridges, M. Bucher, C. Burigana, R. C. Butler, E. Calabrese, B. Cappellini, J.-F. Cardoso, A. Catalano, A. Challinor, A. Chamballu, R.-R. Chary, X. Chen, L.-Y. Chiang, H. C. Chiang, P. R. Christensen, S. Church, D. L. Clements, S. Colombi, L. P. L. Colombo, F. Couchot, A. Coulais, B. P. Crill, A. Curto, F. Cuttaia, L. Danese, R. D. Davies, R. J. Davis, P. de Bernardis, A. de Rosa, G. de Zotti, J. Delabrouille, J.-M. Delouis, and F.-X. Désert. Planck 2013 results. XVI. Cosmological parameters. 03 2013, e-print arXiv:1303.5076.

[34] Polarbear Collaboration, J. Errard, P. Ade, A. Anthony, K. Arnold, F. Aubin, D. Boettger, J. Borrill, C. Cantalupo, M. Dobbs, D. Flanigan, A. Ghribi, N. Halverson, M. Hazumi, W. Holzapfel, J. Howard, P. Hyland, A. Jaffe, B. Keating, T. Kisner, Z. Kermish, A. Lee, E. Linder, M. Lungu, T. Matsumura, N. Miller, X. Meng, M. Myers, H. Nishino, R. O'Brient, D. O'Dea, C. Reichardt, I. Schanning, A. Shimizu, C. Shimmin, M. Shimon, H. Spieler, B. Steinbach, R. Stompor, A. Suzuki, T. Tomaru, H. Tran, C. Tucker, E. Quealy, P. Richards, and O. Zahn. The new generation CMB B-mode polarization experiment: POLARBeaR. *2010 Rencontres de Moriond proceedings*, 11 2010, e-print arXiv:1011.0763.

[35] QUIET Collaboration, D. Araujo, C. Bischoff, A. Brizius, I. Buder, Y. Chinone, K. Cleary, R. N. Dumoulin, A. Kusaka, R. Monsalve, S. K. Næss, L. B. Newburgh, R. Reeves, I. K. Wehus, J. T. L. Zwart, L. Bronfman, R. Bustos, S. E. Church, C. Dickinson, H. K. Eriksen, T. Gaier, J. O. Gundersen, M. Hasegawa,

M. Hazumi, K. M. Huffenberger, K. Ishidoshiro, M. E. Jones, P. Kangaslahti, D. J. Kapner, D. Kubik, C. R. Lawrence, M. Limon, J. J. McMahon, A. D. Miller, M. Nagai, H. Nguyen, G. Nixon, T. J. Pearson, L. Piccirillo, S. J. E. Radford, A. C. S. Readhead, J. L. Richards, D. Samtleben, M. Seiffert, M. C. Shepherd, K. M. Smith, S. T. Staggs, O. Tajima, K. L. Thompson, K. Vanderlinde, and R. Williamson. Second season QUIET observations: Measurements of the CMB polarization power spectrum at 95 ghz. *ApJ*, 760:145, 2012, e-print arXiv:1207.5034.

[36] R. W. Ogburn IV, P. A. R. Ade, R. W. Aikin, M. Amiri, S. J. Benton, C. A. Bischoff, J. J. Bock, J. A. Bonetti, J. A. Brevik, E. Bullock, B. Burger, G. Davis, C. D. Dowell, L. Duband, J. P. Filippini, S. Fliescher, S. R. Golwala, M. Gordon, M. Halpern, M. Hasselfield, G. Hilton, V. V. Hristov, H. Hui, K. Irwin, J. P. Kaufman, B. G. Keating, S. A. Kernasovskiy, J. M. Kovac, C. L. Kuo, E. M. Leitch, M. Lueker, T. Montroy, C. B. Netterfield, H. T. Nguyen, R. O'Brient, A. Orlando, C. L. Pryke, C. Reintsema, S. Richter, J. E. Ruhl, M. C. Runyan, R. Schwarz, C. D. Sheehy, Z. K. Staniszewski, R. V. Sudiwala, G. P. Teply, K. Thompson, J. E. Tolan, A. D. Turner, A. G. Vieregg, D. V. Wiebe, P. Wilson, and C. L. Wong. BICEP2 and Keck Array operational overview and status of observationsl overview and status of observations. 08 2012, e-print arXiv:1208.0638.

[37] Y. Rahmat-Samii, W. Imbriale, and V. Galindo. Conical Corrugated Horn Analysis (CCORHRN). YRS Associates, 1996.

[38] B. Reichborn-Kjennerud, A. M. Aboobaker, P. Ade, F. Aubin, C. Baccigalupi, C. Bao, J. Borrill, C. Cantalupo, D. Chapman, J. Didier, M. Dobbs, J. Grain, W. Grainger, S. Hanany, S. Hillbrand, J. Hubmayr, A. Jaffe, B. Johnson, T. Jones, T. Kisner, J. Klein, A. Korotkov, S. Leach, A. Lee, L. Levinson, M. Limon, K. MacDermid, T. Matsumura, X. Meng, A. Miller, M. Milligan, E. Pascale, D. Polsgrove, N. Ponthieu, K. Raach, I. Sagiv, G. Smecher, F. Stivoli, R. Stompor, and H. Tran. EBEX: A balloon-borne CMB polarization experiment. 07 2010, e-print arXiv:1007.3672.

[39] P. L. Richards. Bolometers fo infrared and millimeter waves. *Journal of Applied Physics*, 76(1):1–24, July 1994.

[40] U. Seljak and M. Zaldarriaga. Signature of gravity waves in polarization of the microwave background. *Phys.Rev.Lett.*, 78:2054–2057, 1997, e-print arXiv:astro-ph/9609169.

[41] G. F. Smoot and C. L. Bennett. Structure in the COBE DMR First Year Maps. *Astrophysical Journal Letters*, page 14, Apr 1992.

[42] K. T. Story, C. L. Reichardt, Z. Hou, R. Keisler, K. A. Aird, B. A. Benson, L. E. Bleem, J. E. Carlstrom, C. L. Chang, H.-M. Cho, T. M. Crawford, A. T. Crites, T. de Haan, M. A. Dobbs, J. Dudley, B. Follin, E. M. George, N. W. Halverson, G. P. Holder, W. L. Holzapfel, S. Hoover, J. D. Hrubes, M. Joy,

L. Knox, A. T. Lee, E. M. Leitch, M. Lueker, D. Luong-Van, J. J. McMahon, J. Mehl, S. S. Meyer, M. Millea, J. J. Mohr, T. E. Montroy, S. Padin, T. Plagge, C. Pryke, J. E. Ruhl, J. T. Sayre, K. K. Schaffer, L. Shaw, E. Shirokoff, H. G. Spieler, Z. Staniszewski, A. A. Stark, A. van Engelen, K. Vanderlinde, J. D. Vieira, R. Williamson, and O. Zahn. A Measurement of the Cosmic Microwave Background Damping Tail from the 2500-square-degree SPT-SZ survey. 10 2012, e-print arXiv:1210.7231.

[43] N. Suzuki, D. Rubin, C. Lidman, G. Aldering, R. Amanullah, K. Barbary, L. Barrientos, J. Botyanszki, M. Brodwin, N. Connolly, K. Dawson, A. Dey, M. Doi, M. Donahue, S. Deustua, P. Eisenhardt, E. Ellingson, L. Faccioli, V. Fadeyev, H. Fakhouri, A. Fruchter, D. Gilbank, M. Gladders, G. Goldhaber, A. Gonzalez, A. Goobar, A. Gude, T. Hattori, H. Hoekstra, E. Hsiao, X. Huang, Y. Ihara, M. Jee, D. Johnston, N. Kashikawa, B. Koester, K. Konishi, M. Kowalski, E. Linder, L. Lubin, J. Melbourne, J. Meyers, T. Morokuma, F. Munshi, C. Mullis, T. Oda, N. Panagia, S. Perlmutter, M. Postman, T. Pritchard, J. Rhodes, P. Ripoche, P. Rosati, D. Schlegel, A. Spadafora, S. A. Stanford, V. Stanishev, D. Stern, M. Strovink, N. Takanashi, K. Tokita, M. Wagner, L. Wang, N. Yasuda, and H. Yee. The Hubble Space Telescope Cluster Supernova Survey: V. Improving the Dark Energy Constraints Above z> 1 and Building an Early-Type-Hosted Supernova Sample. *ApJ*, 746:85, 2012, e-print arXiv:1105.3470.

[44] M. White and M. Srednicki. Window functions of cosmic microwave background experiments. *Astrophysical Journal*, 443(1):6–10, 04 1995.

[45] K. W. Yoon, P. A. R. Ade, D. Barkats, J. O. Battle, E. M. Bierman, J. J. Bock, J. A. Brevik, H. C. Chiang, A. Crites, C. D. Dowell, L. Duband, G. S. Griffin, E. F. Hivon, W. L. Holzapfel, V. V. Hristov, B. G. Keating, J. M. Kovac, C. L. Kuo, A. E. Lange, E. M. Leitch, P. V. Mason, H. T. Nguyen, N. Ponthieu, Y. D. Takahashi, T. Renbarger, L. C. Weintraub, and D. Woolsey. The Robinson Gravitational Wave Background Telescope (BICEP): a bolometric large angular scale CMB polarimeter. e-print arXiv:astro-ph/0606278.

[46] M. Zaldarriaga. The polarization of the cosmic microwave background. In W. L. Freedman, editor, *Measuring and Modeling the Universe*, volume 2, page 309. Cambridge University Press, 2004.